Final Research Performance Progress Report

Federal Agency and Organization: DOE EERE – Geothermal Technologies Program

Recipient Organization: Louisiana State University and A&M College
DUNS Number: 075050765
Recipient Address: Patricia M. Territo, Director
Sponsored Program Accounting Office
Louisiana State University and A & M College
336 Thomas Boyd Hall
Baton Rouge, Louisiana 70803-2901

Award Number: DE-EE0005125
Project Title: Geothermal Resource Development with Zero Mass Withdrawal, Engineered Convection, and Wellbore Energy Conversion
Project Period: 9/1/2011-9/30/2016

Principal Investigator: Dr. Richard Hughes
Professional in Residence and holder of Campanile Charities Professorship
rghughes@LSU.edu
225/578-6038 (off.), 225/284-4742 (mob.)

Report Submitted by: Dr. Richard Hughes
Professional in Residence and holder of Campanile Charities Professorship
rghughes@LSU.edu
225/578-6038 (off.), 225/284-4742 (mob.)

Date of Report Submission: September 30, 2016
Reporting Period: September 1, 2011 to September 30, 2016
Report Frequency: Final

DOE Project Team: DOE Contracting Officer – Laura Merrick
DOE Project Officer – Lauren Boyd
Project Monitor – Alexandra Prisjatschew

Contributing Authors: Dr. Esmail Ansari, Dr. Stephen Sears and Dr. Masoud Safari-Zanjani
Dr. Mayank Tyagi and Dr. Ildar Akmaudlin
Dr. Mileva Radonjic and Kalowale Belo
Dr. Arash Dahi Telighani and Dr. Milad Ahmadi
Dr. Fahui Wang and Keuntai Kim
Dr. Chako John and Brian Harder
Dr. Mark Kaiser and Dr. Brian Snyder

Project Summary

This project is intended to demonstrate the technical and economic feasibility, and environmental and social attractiveness of a novel method of heat extraction from geothermal reservoirs. The emphasis is on assessing the potential for a heat extraction method that couples forced and free convection to maximize extraction efficiency. The heat extraction concept is enhanced by considering wellbore energy conversion, which may include only a boiler for a working fluid, or perhaps a complete boiler, turbine, and condenser cycle within the wellbore. The feasibility of this system depends on maintaining mechanical and hydraulic integrity of the wellbore, so the material properties of the casing-cement system are examined both experimentally and with well design calculations. The attractiveness depends on mitigation of seismic and subsidence risks, economic performance, environmental impact, and social impact – all of which are assessed as components of this study.

Executive Summary

The focus of this project was on the design and economics of the application of a Zero Mass Withdrawal system whereby the entire heat extraction and power generation process is done within a single wellbore. The primary target area for this work was the low enthalpy geothermal systems of the Louisiana Gulf coast but the evaluation was extended somewhat to include other parts of the country. The Louisiana geothermal systems were characterized (Task 1) and response models for both traditional heat extraction and extraction using the ZMW concept were developed for evaluating energy conversion and economics (Task 2). Geochemical changes in the reservoir due to pressure and temperature changes were also evaluated. Since pressure and temperature changes are small, only moderate concerns occur if/when brine salinities are extremely high. The full ZMW wellbore energy conversion system was designed and evaluated for efficiency using mostly "off-the-shelf" products. The in-wellbore turbines are the only piece of the system that may need special handling and it was felt that the heat rejection loop could best be accomplished with air coolers as surface equipment. Thus the entire system fits on a standard well pad. The generated power is much lower than typical surface power generation facilities and the single wellbore system makes the well cost (the largest capital cost) prohibitive at this time. Ideas for increasing the efficiency of the heat extraction and power generation loops are immanently achievable but would require specially designed equipment. As part of the well design, wellbore integrity was evaluated (Task 4) using a liquid pressure-pulse decay permeameter purchased for use on this project and cement additives have been evaluated for use in geothermal environments. A 3D finite element geomechanical code was been developed and used to provide an assessment of the risk of seismic events (Task 5). These risks are again minimal since the overall changes in the pressure and temperature of the system are small. Areas around the proposed geothermal development sites were evaluated to assess the need for power stability or expansion using economic indicators, demographics and emergency and medical facility needs (Task 7). Finally, an economic evaluation (Task 6) was done to provide an estimate of the LCOE for the proposed system. Using historical capital and operating costs and an early design for the system, the LCOE was between 24 and 78 ¢/kWh. Doubling system capacity (which is easily achievable given the initial design) cuts the LCOE by not quite half. Dropping capital expenditures in addition to increasing system capacity provides and LCOE of around 18 ¢/kWh. One design evaluated provided as much as a 7× increase in system capacity with only a slightly larger capital cost and that very optimistic design put the LCOE right at the target power cost of 10 ¢/kWh.

There were five PhD dissertations and two MS theses that were developed from this work. There were also two other MS students and one other PhD student that were funded but did not complete their projects.

Task 1 -- Resource Scope and Characterization

Data from approximately 900 wells with depths greater than 12500 ft deep in South Louisiana were assembled and prepared for the creation of regional thermal maps using the Geographix software system. Three regional heat maps were created using this data. From these maps a promising area was selected based on additional understanding developed through extensive prior work by the Louisiana Geological Survey in various geothermal projects. The Sweet Lake area in Cameron Parish was chosen for further study. Brine, rock property and log data were assembled for the Myogyp sands of the Sweet Lake area (Cameron Parish) and detailed thermal information was extracted from the regional thermal maps. Sweet Lake was chosen for three major reasons. First this is the area that the Louisiana Geological Survey has the most comprehensive geothermal data sets from due to their prior geothermal projects and includes prior geothermal test wells. Second, this is the area that all older thermal maps suggest is the area with the highest concentration of the hottest water resources. This was confirmed in generating these new maps. Third, from the prior geothermal tests in the area it is known that the volumes of water are sufficient for an economically viable model to be created. An example regional thermal map and a detailed structural and thermal map of the Sweet Lake area are shown in Figure 1.

In addition to the Sweet Lake area, extensive work has been done on the Gueydan Dome area (frequently called the Camerina A in this and other work) and the Hackberry field areas. The reservoir characteristics, thermal properties and structural and stratigraphic settings have been used in previous work and the reservoir modeling effort (below) will leverage this previous work.

An additional study was developed whereby data from previous work on Gulf Coast geothermal systems were evaluated. Permeability, porosity, average reservoir temperature, thickness, areal extent, temperature gradient of the earth, reservoir dip angle, injection temperature and well flow rate were the parameters evaluated. These data were transformed using appropriate methods and distributions were fit to the transformed data. An approach for calculating the reservoir dip angle was developed which requires bootstrapping the temperature gradient in the area. The data was used to create the range and distribution of the parameters for experimental design and scaling analysis studies in Task 2.

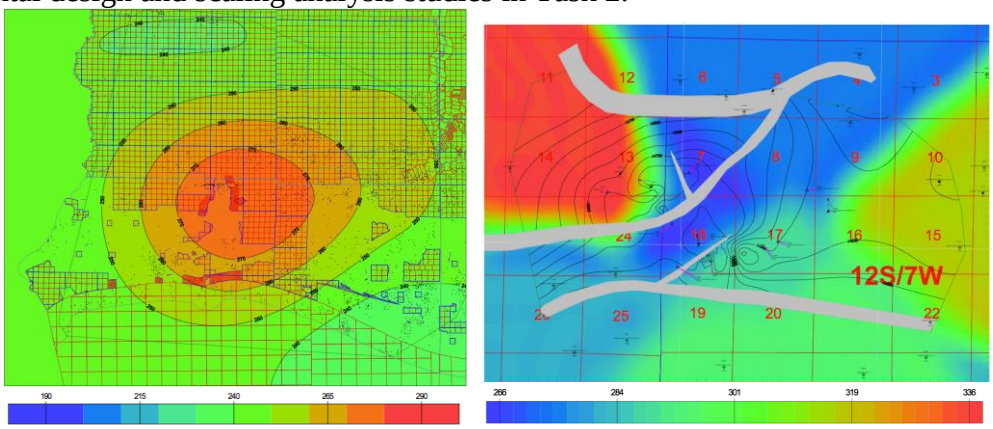

Figure 1: Example Regional Thermal Map and Thermal and Structural Map of the Sweet Lake Area

Results from the statistical analyses were provided in the 2014 annual report for this project, have been published in a PhD dissertation (Ansari, 2016) and is being prepared for a publication.

The geothermal data used was based on the reports published by Bassiouni (1980) and John et al. (1998). The sources contain the data collected in the US Department of Energy "Wells-of-Opportunity" and "Design Wells" programs respectively.

References

Ansari, E.: *Mathematical Scaling and Statistical Modeling of Geopressured-Geothermal Reservoirs*, PhD dissertation, Louisiana State University, 2016.

Bassiouni, Z., 1980. "Evaluation of potential geopressure geothermal test sites in southern Louisiana". Tech. rep., Louisiana State Univ., Baton Rouge (USA). Dept. of Petroleum Engineering.

John, C., Maciasz, G., Harder, B., 1998. "Gulf coast geopressured-geothermal program summary report compilation. volume 2-a: Resource description, program history, wells tested, university and company based research, site restoration". Tech. rep., Louisiana State Univ., Basin Research Inst., Baton Rouge, LA (United States).

Task 2 – Reservoir Engineering

There are two primary thrusts in the work in the reservoir engineering task. The first is modeling heat harvesting techniques using the zero mass withdrawal, engineered convection process and the other is modeling the geochemical responses that will occur during the process.

Heat Harvesting and Engineered Convection Modeling

Our previous dimensional works show that regular design performs better than reverse design for heat harvesting (Ansari, et. al., 2014). In this section, a set of dimensionless groups have been obtained from dimensional and inspectional analysis and these groups are explained. An experimental design and response surface model has been applied to these groups. The obtained screening model is then presented and discussed.
A regular line-drive design is scaled for obtaining dimensionless groups using inspectional analysis. The obtained dimensionless groups are (for details, see Ansari, 2016):

$$\pi_1 = \frac{\phi c_t}{c_f} \qquad \pi_2 = \frac{\phi \beta_t}{\beta_f}$$

$$\pi_3 = M \qquad \pi_4 = c_f p_1^* = \frac{c_f \mu q L}{k_x W H}$$

$$\pi_5 = \beta_f T_1^* = \beta_f T_{avg} \qquad \pi_6 = R_L = \frac{L}{H}\sqrt{\frac{k_z}{k_x}}$$

$$\pi_7 = \frac{L}{H}\tan\alpha \qquad \pi_8 = \frac{L}{H}$$

$$\pi_9 = N_\alpha = \frac{k_x \rho_0 g \sin\alpha\, W H}{q\mu} \qquad \pi_{10} = Pe = \frac{u_T H}{\kappa} = \frac{q}{\kappa W}$$

$$\pi_{11} = \frac{\kappa'_{ob}}{\kappa} \qquad \pi_{12} = \frac{\kappa'_{ub}}{\kappa}$$

$$\pi_{13} = c_f(p_i - p_0) \qquad \pi_{14} = \frac{T_{inj}}{T_{avg}}$$

$$\pi_{15} = \frac{\tau \sin\alpha\, L}{T_{avg}} \qquad \pi_{16} = \frac{T_0}{T_{avg}}$$

Because the focus of the study is to model thermal recovery factor and production temperature, the energy equation is used for scaling the time (see Ansari, 2016). The dimensionless time for this system is then:

$$t_D = \frac{1}{M}\frac{qt}{LWH}$$

in which $M = (\rho_m C_{pm})/(\rho_f C_{pf})$. Note that if the dimensionless time was defined based on the momentum equation, it would be

$$t_{D_{hyd}} = \frac{\phi C_f}{C_t}\frac{qt}{LWH}$$

All of these dimensionless groups are needed for transforming the dimensional model into the dimensionless representation; however, their form can be heuristically manipulated (multiplied or divided) to get other desirable dimensionless groups.

Five dimensionless groups are identical to those published by previous researchers. They are: π_3 representing matrix to fluid heat capacity ratio (Phillips, 2009), π_6 representing effective aspect ratio (Shook et al., 1992; Wood et al., 2008), π_7 representing the dip angle group (Shook et al., 1992; Wood et al., 2008), ($\pi_4 \times \pi_9 \times \pi_{15} / \pi_7$) representing the buoyancy number (Shook et al., 1992; Wood et al., 2008), and π_{10} representing the Peclet number (Phillips, 2009).

The meaning of other dimensionless groups can be discerned from their derivation or their format: π_1 is the ratio of total compressibility to fluid compressibility; π_2 is the ratio of total expansivity to fluid expansivity; π_5 is fluid expansion due to average reservoir temperature; π_{11} and π_{12} show the ratio of heat conduction across the boundary to heat conduction within the reservoir; π_{13} describes fluid compression as a result of reservoir pressure; π_{14} scales the injection temperature to the average reservoir temperature; π_{15} scales the temperature difference across the reservoir to the average reservoir temperature and represents temperature distribution in the reservoir; and π_{16} scales the reference temperature to the average reservoir temperature. The effective aspect ratio is defined as

$$R_L = \frac{\mathrm{L}}{\mathrm{H}}\sqrt{\frac{k_z}{k_x}}$$

The effective aspect ratio controls the cross flow within the reservoir and indicates the ratio of the rate of communication between the fluids in the horizontal direction to the rate of communication between the fluids in the vertical direction. This number is purely a reservoir characteristic and has been reported for oil and gas waterflooding, CO_2 injection, surfactant-polymer as well as surfactant enhanced CO_2 flooding. (Shook et al., 1992; Novakovic, 2002; Rai, 2008; Wood et al., 2008; Afonja, 2013). A smaller aspect ratio means that the fluid communication in the horizontal direction is more than the fluid communication along the vertical direction. Novakovic (2002) gives several other interpretations for effective aspect ratio. For homogeneous isotropic reservoirs, effective aspect ratio reduces to the aspect ratio; thus this ratio can be seen as heterogeneity scaled aspect ratio. This number can also be interpreted as relative flow capacity of the reservoir in the vertical and horizontal direction (Novakovic, 2002). The dip angle group is:

$$N_\alpha = \frac{\mathrm{L}}{\mathrm{H}}\tan\alpha$$

This dimensionless number has no affiliated fluid or rock properties and is entirely geometrical. This number has been published for water and CO_2 injection scenarios (Shook et al., 1992; Wood et al., 2008). This number is also known as the tilt number and interpreted as a measure of the rotation of the system. If this number is multiplied by another dimensionless group, it transforms it from a horizontal-vertical system to a longitudinal-transverse system accounting for the tilt (Novakovic, 2002).

The buoyancy number has also been published by previous authors (Shook et al., 1992; Novakovic, 2002; Wood et al., 2008; Rai, 2008; Afonja, 2013). The buoyancy number is the ratio of the gravity forces to the viscous forces and is sometimes called the gravity number and in this work it is given by:

$$N_g = \frac{\pi_4 \pi_9 \pi_{15}}{\pi_7} = \frac{k_x \Delta\rho g \cos\alpha \, W H^2}{\mathrm{q\mu L}}$$

In petroleum engineering, the density difference between injection and production fluid creates this number. In geothermal reservoirs, the difference in the temperature and mineralogy of the geofluid across the reservoir creates the density difference.

The Peclet number is the ratio of the rate of heat advection to the rate of heat diffusion in the porous media (Phillips, 2009). In this work it is given by

$$\mathrm{Pe} = \frac{u_T \mathrm{H}}{\kappa} = \frac{Q}{\kappa \mathrm{W}}$$

In aquifers with higher thickness and higher flow velocity (e.g. higher permeability), heat convection overwhelms heat diffusion and the Peclet number is high. When the aquifer thickness is small compared with its width, Peclet number is also small and heat only transfers by conduction (Phillips, 2009). A decrease in thermal diffusion also increases Peclet number.

The set of thermal diffusivity ratio π values (π_{11} and π_{12}) show the ratio of the conductive heat transfer across the boundary to the conductive heat transfer in the matrix. These numbers are purely geological characteristics. The higher the thermal diffusivity ratio, the greater the heat transfer across the reservoir and the higher thermal recovery. These values are:

$$\pi_{11} = (N_{th})_{ob} = \frac{\kappa'_{ob}}{\kappa}$$

$$\pi_{12} = (N_{th})_{ub} = \frac{\kappa'_{ub}}{\kappa}$$

The π_{14} temperature ratio group provides the ratio of injected energy to the total energy in place. This is an operational number and is set by the heat exchanger design. Temperature ratio inversely affects thermal recovery. If the injection temperature is high, this temperature ratio will also be high. Higher values mean less energy recovery from the reservoir. The π_{16} group can typically be ignored because reference temperature does not affect the thermal recovery from the reservoir.

The natural geothermal gradient creates a temperature distribution in the reservoir. Because reservoir length (i.e. the distance between wells for this system) is typically larger than the

reservoir layer thickness, the temperature distribution number (π_{15}) considers temperature differences across the reservoir. The tilt number (i.e. dip angle number) can be used to rotate this number to account for the temperature distribution along the thickness of the reservoir (π_{15}/N_{α}).

There are five rock and fluid numbers (π_1, π_2, π_3, π_5, and π_{13}). The *M* term in π_3, is the matrix/fluid thermal capacity ratio

$$\mathrm{M} = \frac{\rho_m c_{pm}}{\rho_f c_f}$$

and $\rho_m c_{pm} = \phi c_{pf} + (1 - \phi) c_{pr}$. All of these numbers consist of rock and fluid characteristics. We assume that fluid properties are functions of temperature and pressure and use available tables for calculating them (Lemmon et al., 2007). Rock properties are assumed constant across the system in this development.

Figure 2 shows a typical two-dimensional line drive model. The model has 25×1×10 grid blocks with each grid block being 120 m × 100 m × 10.5 m in the X and Y and Z directions, respectively. The reservoir has a dip angle of 5° with an average reservoir temperature of 115° C assigned to the middle of the reservoir. Thermal gradient is 24 °C/km. The injection temperature is 30° C and the injection and production rates are 1250 m^3/day. The reservoir rock cools down as the front slowly propagates in the reservoir and moves towards the production well. Figure 2b shows the thermal front at $t_D = 0.2$ (~8.5 years for this system) when no breakthrough has occurred. Thermal breakthrough happens around $t_D = 0.6$ (ca. 25 years, Figure 2c). Figure 2d and Figure 2e show reservoir temperature at $t_D = 1$ (41.5 years) and $t_D = 3$ (124 years) respectively.

At the start of the simulation, the temperature drop in the production well is due to the geothermal gradient in the model. When breakthrough happens, there is a sharp decrease in the

production temperature and finally at the late times, the model temperature asymptotically approaches the injection temperature. This behavior is used in the next section to develop a predictive model for dimensionless production temperature and thermal recovery factor.

To calculate the energy production rate, a model to predict the temperature of the production fluid versus time is needed and to assess the net energy that a system can produce, a model for

predicting thermal recovery factor is needed. In this work, the derived dimensionless numbers were confirmed and used to create predictive models for dimensionless production temperature and heat recovery factor. For doing this, important dimensionless numbers for different models are matched to validate that the models with the same dimensionless numbers would give identical dimensionless results. A Box-Bhenken design is then used to sample the parameter space and create the dimensionless numbers. A violin plot is created from the data for assessing uncertainty in the production temperature and energy recovery factor. A procedure known as all subset regression is used to compare all possible models and select the optimum one. These simplified final models were then presented and assessed. This section first discusses the model

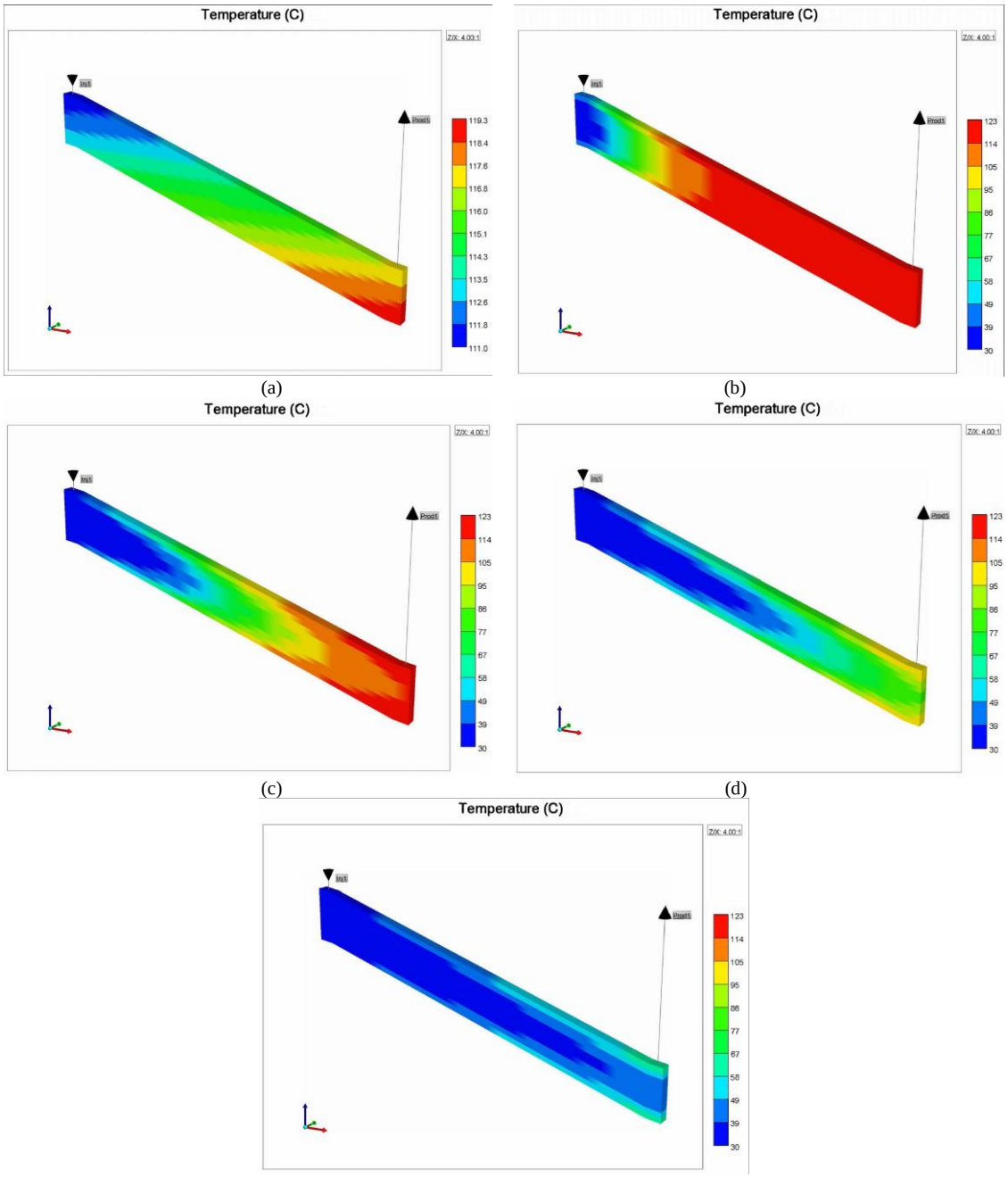

Figure 2: (a) Reservoir temperature at initial condition (t_D = 0) with an average temperature of 115 C assigned to the middle of the reservoir. Temperature gradient is 24 C/m and dip angle is 5°. (b) Thermal front at t_D = 0.2 (ca. 8.3 years). (c) Thermal front at breakthrough t_D = 0.6 (ca. 25 years). (d) Thermal front at t_D = 1 (ca. 41.5 years). € Thermal front at t_D = 3 (ca. 124 years). Vertical axis is exaggerated four times in all figures.

developed for the dimensionless production temperature for the line-drive system and then presents a model for thermal recovery factor.

A major shortcoming of all previous published works is that they are only useful for a specific dimensionless time. Some of these works model their response at specific times such as oil

breakthrough (Wood et al., 2008). However, dimensionless time can be inserted inside the model according to the following: assume predictor variables ($x_1, x_2, \ldots, x_m$) and regression coefficients ($\beta_0, \beta_1, \ldots, \beta_m$) can model response Y.

$$Y = \beta_0 + \beta_1 x_1 + \cdots + \beta_m x_m + E.$$

Now, assume that the regression coefficients $\beta_0, \beta_1, \ldots, \beta_m$ are functions of dimensionless time and can be regressed independently.

$$\begin{aligned} \beta_0 &= \alpha_{00} + \alpha_{01}\, t_D \\ \beta_1 &= \alpha_{10} + \alpha_{11}\, t_D \\ &\cdots \\ \beta_m &= \alpha_{m0} + \alpha_{m1}\, t_D \end{aligned}$$

Substituting the regressed coefficients into the multiple regression formulation yields:

$$\begin{aligned} Y = {} & \alpha_{00}\beta_0 + \alpha_{01}\beta_0 t_D + \alpha_{10}\beta_1 x_1 + \alpha_{20}\beta_2 x_2 + \cdot + \alpha_{m0}\beta_m x_m \\ & + \alpha_{11}\beta_1 x_1\, t_D + \cdot\ + \alpha_{21}\beta_2 x_2\, t_D + \cdot + \alpha_{m1}\beta_m x_m\, t_D \end{aligned}$$

This equation implies that dimensionless time can be added as a predictor for Y if we retain the dimensionless time's interaction with other dimensionless numbers.

A model for dimensionless production temperature can be used to calculate the rate of energy production versus time. The dimensionless production temperature is the ratio of the producing fluid temperature to the initial average reservoir temperature.

$$T_D = \frac{\text{production temperature}}{\text{initial average temperature}}$$

The energy recovery factor is defined as the ratio of the produced energy to the total energy in place before exploiting the reservoir (Muffler and Cataldi, 1978; Nathen- son, 1975; Williams et al., 2008). Cumulative produced energy can be directly calculated using energy recovery factor.

After testing and validating the dimensionless numbers, a model for dimensionless production temperature was selected, presented and assessed and then the same systematic procedure was used to develop a model for the thermal recovery factor.

For any given similar flow problem (i.e. same configuration and boundary conditions), matching the dimensionless numbers will yield similar dimensionless results (e.g. thermal recovery factor or dimensionless temperature) between scales. For validating the dimensionless numbers, the parameters in the groups are varied but the groups are held constant. Fifteen different reservoir models were considered such that their geometrical and dimensional properties were different but their dimensionless groups were identical (for details see Ansari, 2016). The energy recovery factor was then plotted versus dimensionless time. Matching the cases where the parameters were changed but their group values remain the same would suggest that the dimensionless numbers adequately scale the system. The dimensional result vs. time for these fifteen models

did not show any pattern but the models with identical dimensionless numbers showed the same dimensionless temperature and thermal energy recovery factor (Ansari, 2016).

Once the thermal recovery factor curves corresponding to similar dimensionless numbers were matched, violin plots were created directly from the data. Violin plots are useful for answering generic uncertain questions with minimum data (White, 2013). A violin plot (see Figure 3)shows a combination of the box plot and a rotated kernel density plot (i.e. an estimation for probability

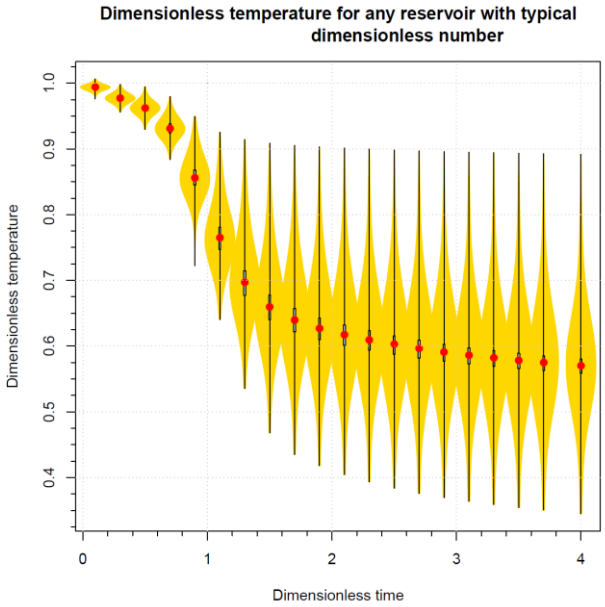

Figure 3 Violin plot for dimensionless temperature

density function). In the violin plot, the middle dot shows the median (which is identical to the mode and maximum likelihood estimator of the mean in a normal distribution), the white boxes indicate the lower to upper quartile and the thin black lines are whiskers. Edges of the vertical lines shows the minimum and maximum values. The tail of the violins where no whiskers (thin black line) exist has few data and can be disregarded for uncertainty assessments. These plots can also be updated when additional certain data are available. Violin plots are used to determine how many piecewise regression models are needed and to specify their dimensionless time ranges. Three regression models were chosen based on the median points: $0 < t_D \leq 0.5$, $0.5 < t_D \leq 1.5$ and $1.5 < t_D \leq 4$.

Inspectional analysis quickly becomes overwhelming and performing a relative im- portance analysis is a good way to make it manageable. ANOVA is traditionally used to identify the factor significance of uncorrelated variables (White and Royer, 2003). The dimensionless numbers are algebraically independent but statistically dependent because they are functions of random parameters (Rice, 2006; Soong, 2004). Experimental design is difficult when factors are correlated with each other (White and Royer, 2003). Another complication is that the relative importance of dimensionless numbers varies with dimensionless time. These changes in relative importance are smooth and modeling every dimensionless time is redundant. Segmented (piecewise) regression is used for creating models with time-varying coefficients. The segmentation range can be chosen heuristically using violin plots and then be tested using trial

and error to obtain the best segmented model. In order to determine the relative importance of the predictors a robust tree-based algorithm, known as Boosting is used. The Boosting method creates an ensemble of independent regression trees and updates them sequentially. Each tree is fit to the current step residual and the final model is the average of all the trees weighted by a shrinkage parameter which controls the rate at which boosting learns (James et al., 2013; Hastie et al., 2009; Kuhn and Johnson, 2013). There were 10,000 trees with an interaction depth of 4 and shrinkage parameter of 0.01 in the Boosting algorithm for this work.

Dimensionless numbers were rank-ordered based on their relative importance in predicting the dimensionless temperature. Dimensionless time was the most important factor in determining dimensionless temperature for $0 < t_D \leq 1.5$ while temperature ratio (π_{14}) was more important for $1.5 < t_D \leq 4$. Peclet number (π_{10}) and aspect ratio (π_8) are other important dimensionless numbers in predicting the response. The dimensionless numbers which do not affect the response can be safely disregarded for prediction. Dimensionless numbers with less than 1% relative importance were ignored.

The model was fit at eighty values for dimensionless time with step size of $t_D = 0.05$ (i.e. 0 t_D , 0.05 t_D , 0.1 t_D , ..., 4 t_D). Segmented (piecewise) regression was used to model dimensionless production temperature using 761 runs. The violin plot was used for segmenting the model. The segments were then be tested using trial and error to find the best ranges for segmenting. A procedure known as "all subset regression" was used to assess all possible sub-models The purpose of the model selection for this work is to obtain a simple model with a minimum number of predictors and interactions. Choosing a simpler model trades off a small increase in the model bias. Introducing more predictors improves the R^2. The optimum model is both simple (i.e. has fewer terms) and representative (i.e. close to the best model). The choice of the final model is based on the modeler's selection and how the person trades off increasing terms with increasing R^2 value. The model with the maximum R^2 value found by the "all subset regression" algorithm was selected as the best model. The selected models for dimensionless production temperature are presented in Box 1.

Box 1: Proposed model for dimensionless production temperature

For $0 \leq t_D \leq 0.5$, we have:

$$T_D = 0.9936 - 0.0267t_D - 0.0516\pi_{15} + 0.0002\pi_7 - 0.8434t_D\pi_{15} + 0.0029t_D\pi_7 + 0.0045\pi_{15}\pi_7$$

for $0.5 < t_D \leq 1.5$, we have:

$$T_D = 1.3429 - 0.6041t_D - 0.4467\pi_{14} - 0.001\pi_8 + 0.6101t_D\pi_{14} + 0.0022t_D\pi_8 - 0.0003t_D\pi_{10} + 0.0003\pi_{10}\pi_{14} - 0.0001\pi_8\pi_{10}$$

and for $1.5 < t_D \leq 4$, we have:

$$T_D = 0.4528 - 0.0587t_D + 0.4880\pi_{14} - 0.0004\pi_{10} + 0.0037\pi_8 + 0.0729t_D\pi_{14} - 0.003\pi_{14}\pi_8 - 0.0003t_D\pi_8 + 0.0004\pi_{14}\pi_{10}$$

Figure 4 shows the assessment of the reduced final model (Box 1). In each sub-figure 711 runs were used for training and 50 runs for testing. This means that 7,821 (i.e. 711×11) training

samples (blue points) and 550 (i.e. 50×11) testing samples (red points) were used for the first segment, 14,220 training samples and 1,000 testing samples were used for the second segment and 35,550 training samples and 2,500 testing samples were used for the third segment.

The same procedure that was used to model dimensionless production temperature was used to develop a thermal recovery factor model. First, the violin plots are presented and the segmentation ranges for the dimensionless time are heuristically found. The important dimensionless numbers in each ranges of the dimensionless time are found and then the optimum models consisting of these important dimensionless numbers are selected. Finally, the simplified models are presented and assessed.

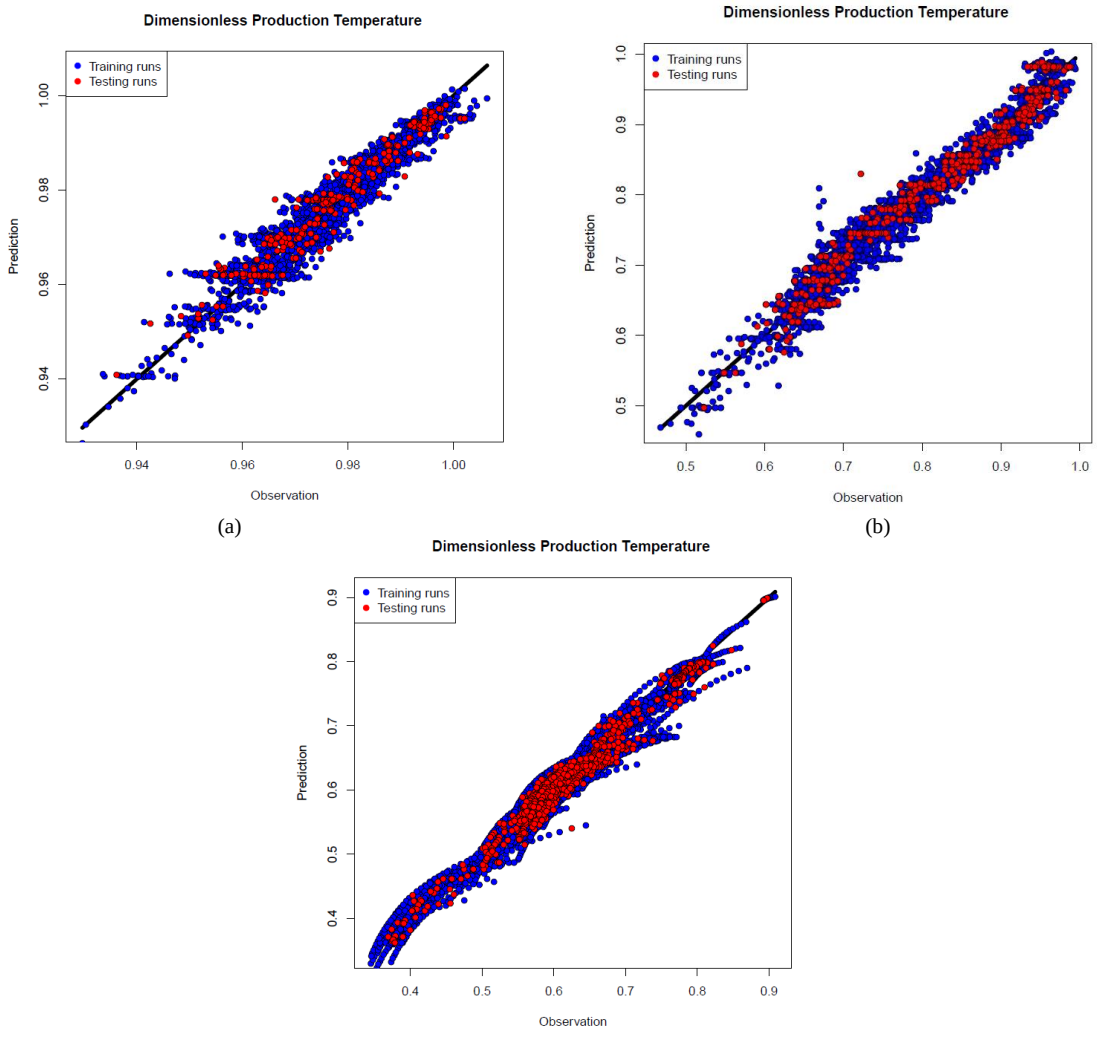

Figure 4 Simplified model prediction vs simulated observation for dimensionless production temperature. Figure (a) is for $t_D \leq 0.5, 5$ (b) $0.5 < t_D \leq 1$ and (c) $1.5 < t_D \leq 4$.

Again, violin plots were used to determine the number of segments and their ranges A sensitivity analysis was performed to find the important dimensionless numbers in predicting the response

and important dimensionless numbers were found to develop a model for the thermal recovery factor. The simplified models for energy recovery factor are shown in Box 2.

Box 2: Proposed model for thermal recovery factor

For $0 \leq t_D \leq 1$, we have:

$$RF = 1.083 t_D$$

and for $1 < t_D \leq 4$, we have:

$$RF = 1.01 + 0.0405 t_D - 0.829 \pi_{14} - 0.002 \pi_8 + 1.01 t_D \pi_{14} + 0.0022 t_D \pi_8 - 0.0071 \pi_{14} \pi_8$$

By a similar process, scaling and inspectional analysis was performed on the Zero Mass Withdrawl system (details in Ansari, 2016) using the system configuration shown in Figure 5.

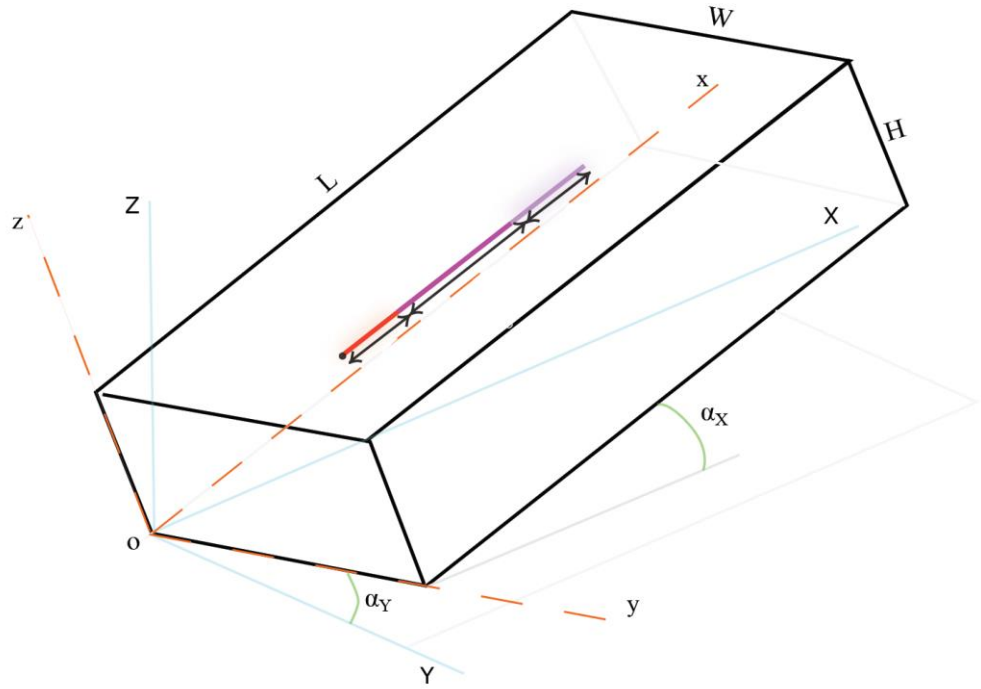

Figure 5 Zero Mass Withdrawal (ZMW) design. This design is based on Feng et al. (2014) and Novakovic (2002) work for studying the effect of downhole heat exchangers on geopressured geothermal reservoirs using a single horizontal wellbore. For Gulf coast geothermal reservoirs W/H is more than ca. 120, assuming L = W = Area$^{0.5}$

From the analysis, the following dimensionless numbers were obtained for the ZMW system:

$$\pi_1 = \frac{\phi c_t}{c_f} \qquad \pi_2 = \frac{\phi \beta_t}{\beta_f}$$

$$\pi_3 = M \qquad \pi_4 = c_f p_1^* = \frac{c_f \mu q (L_{prod} + L_{ins} + L_{inj})}{H L_{ins}}$$

$$\pi_5 = \beta_f T_1^* = \beta_f T_{avg} \qquad \pi_6 = \frac{(L_{prod} + L_{ins} + L_{inj})}{H} \sqrt{\frac{k_z}{k_x}}$$

$$\pi_7 = \frac{L_{ins}}{H} \sqrt{\frac{k_z}{k_y}} \qquad \pi_8 = \frac{(L_{prod} + L_{ins} + L_{inj})}{H} \tan(\alpha_X)$$

$$\pi_9 = \frac{L_{ins}}{H} \tan(\alpha_Y) \qquad \pi_{10} = \frac{L_{prod}}{H}$$

$$\pi_{11} = \frac{L_{inj}}{H} \qquad \pi_{12} = \frac{L_{ins}}{H}$$

$$\pi_{13} = \frac{k_x}{\mu} \frac{\rho_f g \sin\alpha_X \cos\alpha_Y L_{ins} H}{q} \qquad \pi_{14} = \frac{u_{x1}^* z_1^*}{\kappa} = \frac{q}{\kappa L_{ins}}$$

$$\pi_{15} = \frac{\kappa'_{ob}}{\kappa} \qquad \pi_{16} = \frac{\kappa'_{ub}}{\kappa}$$

$$\pi_{17} = c_f \, p_i \qquad \pi_{18} = \frac{T_{inj}}{T_{avg}}$$

$$\pi_{19} = \frac{\tau \sin\alpha_X \cos\alpha_Y (L_{prod} + L_{ins} + L_{inj})}{T_{avg}}$$

The thermal dimensionless time based on the energy equation for this system is:

$$t_D = \frac{\rho_f C_f}{(\phi \rho_f C_f + (1-\phi)\rho_r C_r)} \frac{q\,t}{(L_{prod} + L_{ins} + L_{inj}) L_{ins} H}$$

Similar to the line drive system, matching the dimensionless numbers gives similar dimensionless results. A violin uncertainty plot for the dimensionless production temperature was developed and the model was segmented using the violin plot. For the ZMW design, dimensionless time was the most important factor in determining dimensionless production temperature at early times. However, at later times, temperature ratio (π_{18}) and Peclet number (π_{14}) become more important. Dip angle group (π_8), dimensionless production (π_{10}) and injection length (π_{11}) are other important dimensionless numbers. The model was fit using eighty values for dimensionless time with step size of t_D = 0.25 and again using the "all subset regression" procedure, all possible models were investigated. The selected models for dimensionless production temperature are presented in Box 3 and Figure 6.7 shows the assessment of the reduced final model. In each sub-figure 786 runs were used for training and 55 runs for testing.

This same procedure was used to model thermal recovery factor. First a violin plot is created to determine how many piecewise regression models are needed and to specify their dimensionless time ranges. Then a sensitivity analysis is performed to find the important dimensionless numbers in predicting the response for each dimensionless time segment. The models are reduced by comparing their R^2 values and the final simple model is presented (see Box 4). Finally, these reduced models are assessed to observe their performance (Figure 7).

Box 3: Proposed model for dimensionless production temperature

For $0 \leq t_D \leq 0.5$, we have:

$$T_D = 1$$

For $0.5 \leq t_D \leq 2.5$, we have:

$$T_D = 0.9782 - 0.1051 t_D + 0.0001\pi_{14} + 0.0059\pi_6 + 0.0963 t_D\pi_{18} + 0.0018 t_D\pi_{10} + 0.0001\pi_{14}\pi_{10} - 0.0001\pi_{14}\pi_6 - 0.0002\pi_6\pi_{10}$$

For $2.5 < t_D \leq 5$, we have:

$$T_D = 0.7284 + 0.2924\pi_{18} - 0.0234 t_D + 0.0059\pi_{10} + 0.0101\pi_6 + 0.0001\pi_{10}\pi_{14} + 0.0001\pi_{14}\pi_{11} - 0.0002\pi_6\pi_{14} - 0.001\pi_{10}\pi_{11}$$

For $5 < t_D \leq 10$, we have:

$$T_D = 0.6057 - 0.0106 t_D + 0.3952\pi_{18} + 0.0112\pi_6 + 0.0073\pi_{10} + 0.0001\pi_{10}\pi_{14} + 0.0002\pi_{14}\pi_{11} - 0.0002\pi_6\pi_{14} - 0.0011\pi_{10}\pi_{11}$$

and for $10 < t_D \leq 20$, we have:

$$T_D = 0.5004 - 0.0047 t_D + 0.0081\pi_{10} + 0.4878\pi_{18} + 0.0113\pi_6 + 0.0001\pi_{10}\pi_{14} + 0.0002\pi_{14}\pi_{11} - 0.0002\pi_6\pi_{14} - 0.0011\pi_{11}\pi_{10}$$

Box 4: Proposed model for thermal recovery factor

For $0 \leq t_D \leq 5$, we have:

$$RF = 1.7742 t_D$$

and for $5 < t_D \leq 20$, we have:

$$RF = 3.6441 + 0.8895 t_D - 3.5367\pi_{18} + 1.081 t_D\pi_{18}$$

Ansari (2016) provides several example calculations and compares the results to detailed reservoir modeling of geothermal systems that have more realistic geologic features and properties. These include two low enthalpy geothermal systems in Louisiana (Gueydan Dome and Sweet Lake) as well as areas outside the Gulf coast region where the parameter values are outside the statistics of those in Louisiana where the models were developed. As expected, the simplified models captured the thermal decline and the energy recovery very well for the Gulf coast systems. They also did reasonably well with the cases outside the region with a bit higher error in the predicted amount of energy produced with the results being conservative (predicting lower values than what was stated in the papers).

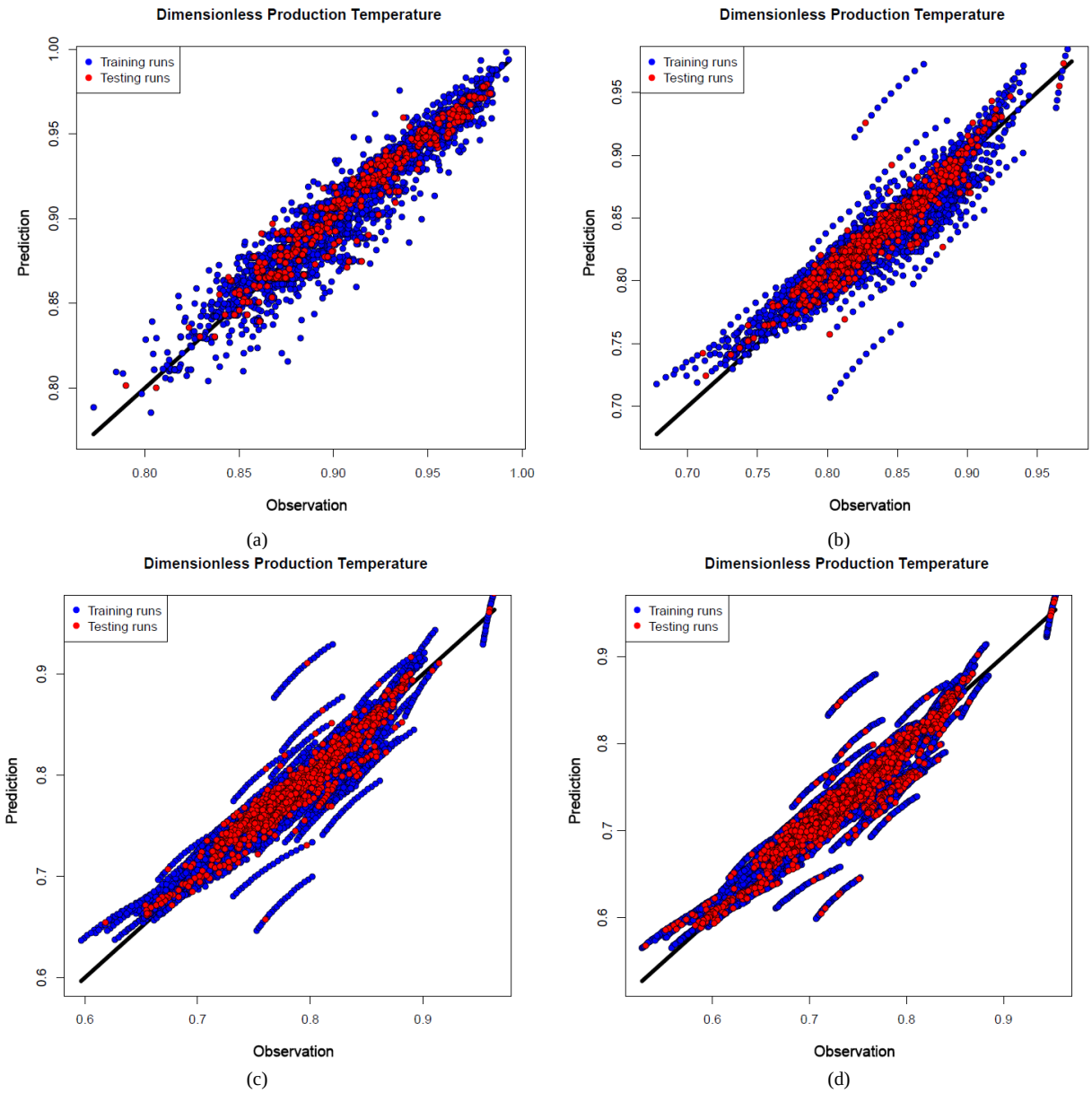

Figure 6 Simplified model prediction vs simulated observation for Dimensionless production temperature. Figure (a) is for $0.5 < t_D \leq 2.5$, (b) $2.5 < t_D \leq 5$ (c) $5 < t_D \leq 10$ and (d) $10 < t_D \leq 20$.

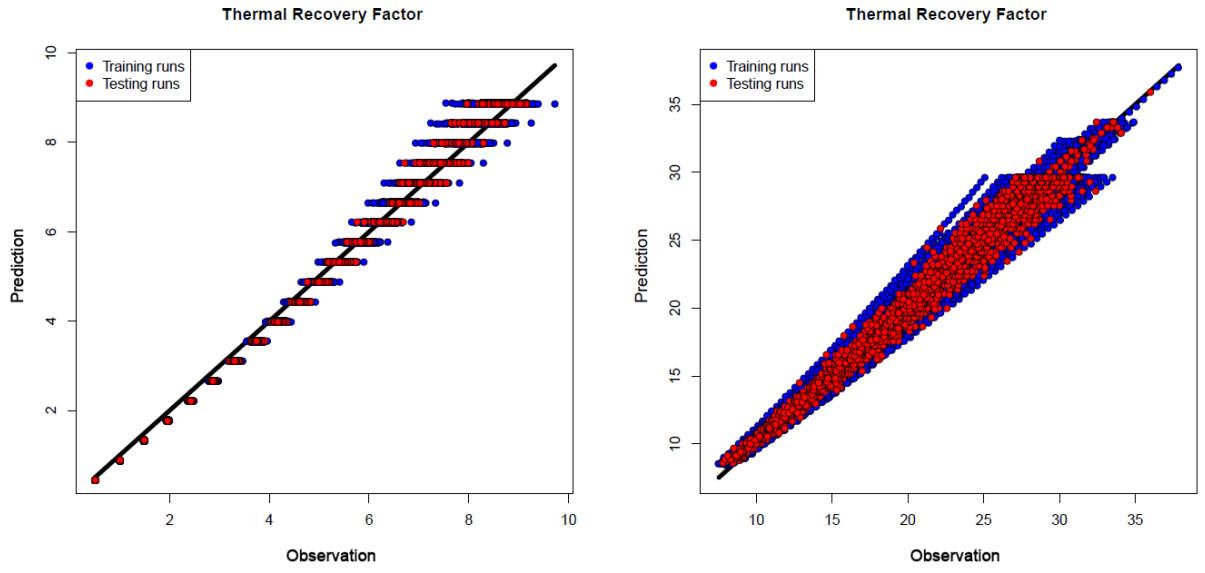

(a) (b)

Figure 7 Simplified model prediction vs simulated observation for thermal recovery factor. Figure (a) is for $t_D \leq 5$ and (b) $5 < t_D \leq 20$.

References

Afonja, G. I. (2013). *Development of a Framework for Scaling Surfactant Enhanced CO_2 Flooding from Laboratory Scale to Field Implementation*. Ph. D. thesis, Louisiana State University.

Ansari, E.: *Mathematical Scaling and Statistical Modeling of Geopressured-Geothermal Reservoirs*, PhD dissertation, Louisiana State University, 2016.

Ansari, E., R. Hughes, and C. D. White (2014). "Well placement optimization for maximum energy recovery from hot saline aquifers". In 39th Workshop on Geothermal Reservoir Engineering, Stanford University. SGP-TR-202.

Feng, Y. (2012). *Numerical study of downhole heat exchanger concept in geothermal energy extraction from saturated and fractured reservoirs*. Ph. D. thesis, Louisiana State University.

Feng, Y., M. Tyagi, and C. D. White (2014). "A downhole heat exchanger for horizontal wells in low-enthalpy geopressured geothermal brine reservoirs". *Geothermics* 53, 368– 378.

Hastie, T., R. Tibshirani, J. Friedman (2009). *The elements of statistical learning, Volume 2*. Springer.

James, G., D. Witten, T. Hastie, and R. Tibshirani (2013). *An introduction to statistical learning*. Springer.

Kuhn, M. and K. Johnson (2013). *Applied predictive modeling*. Springer.

Muffler, P. and R. Cataldi (1978). "Methods for regional assessment of geothermal resources". *Geothermics* 7 (2), 53–89.

Nathenson, M. (1975). Physical factors determining the fraction of stored energy recoverable from hydrothermal convection systems and conduction-dominated areas. Technical report, Geological Survey, Menlo Park, Calif.(USA).

Novakovic, D. (2002). *Numerical reservoir characterization using dimensionless scale numbers with application in upscaling*. Ph. D. thesis, Louisiana State University.

Phillips, O. M. (2009). *Geological fluid dynamics: sub-surface flow and reactions*. Cambridge University Press.

R Core Team (2014). R: *A Language and Environment for Statistical Computing*. Vienna, Austria: R Foundation for Statistical Computing.

Rai, K. (2008). *Screening model for surfactant-polymer flooding using dimensionless groups*. Master's thesis, University of Texas at Austin.

Rice, J. (2006). *Mathematical statistics and data analysis*. Cengage Learning.

Shook, M., D. Li, and L. W. Lake (1992). "Scaling immiscible flow through permeable media by inspectional analysis". *In Situ*;(United States) 16 (4).

STARS manual (2011). Advanced process and thermal reservoir simulator. Computational Modeling Group, Ltd. , Calgary, AB, Canada.

White, C. and S. Royer (2003). Experimental design as a framework for reservoir studies. In SPE Reservoir Simulation Symposium, Houston, Texas, SPE-79676-MS.

White, C. D. (2013). Statistical Reservoir Modeling, PETE 7285 course notes.

Williams, C. F., M. J. Reed, and R. H. Mariner (2008). A review of methods applied by the us geological survey in the assessment of identified geothermal resources. US Geological Survey Open-File Report 1296 (2008), 27.

Wood, D. J., L. W. Lake, R. T. Johns, V. Nunez, et al. (2008). "A screening model for CO2 flooding and storage in Gulf Coast reservoirs based on dimensionless groups". *SPE Reservoir Evaluation & Engineering* 11 (03), 513–520.

Geochemical Modeling

Permeability damage due to mineral transformations and scale formation in the heat exchanger can be a potential problem for operating downhole heat exchangers. Although considerable efforts have been done to solve the scaling problem in production and surface facilities (Gallup and Featherstone, 1995, Manceau et al., 1995, Gallup, 1996), the impact of scaling in downhole exchangers and rock-brine interactions on reservoir permeability and porosity has not been addressed as fully. In this paper, interactions between a geothermal brine and reservoir sediments in Vermilion Parish, Louisiana are examined using geochemical modeling. A downhole heat exchanger configuration proposed by Feng et al (2015) has been considered for this study. The objective of this work is to investigate the potential of scaling inside the heat exchanger due to the temperature drop and reservoir permeability damage due to brine-rock geochemical interactions.

In the late 1970s, a program was started by DOE to investigate the geothermal-geopressured formations in southeast Louisiana. This program included "identification, qualification, acquisition, planning and conducting of geothermal-geopressured formation tests in oil or gas prospective wells about to be drilled, being drilled, or being abandoned" (Dobson et al., 1980). For the current study, data collected from the Beulah Simon No. 2 test well have been used. The tests on this well were conducted by Gruy Federal, Inc., under a contract with the DOE (Dobson et al., 1980). The Beulah Simon well is located in Vermilion Parish, Louisiana, about 5 miles northeast of the town Kaplan and 30 Miles southeast of Lafayette (Figure 8).

The target formation, which is geopressured-geothermal, consists of a thick bed of Camerina A sand, a member of the Frio formation. The net sand thickness for the Camerina A section at the Beulah Simon No.2 is 266 feet (Dobson et al., 1980). Some of the geological and petrophysical information of this area has been summarized in Table 1 (Dobson et al., 1980).

The brine composition reported by Southern Petroleum Laboratories collected from the Beulah Simon No.2, Vermilion Parish, Louisiana, (Table 2) (Dobson et al., 1980), has been used for geochemical modeling purposes.

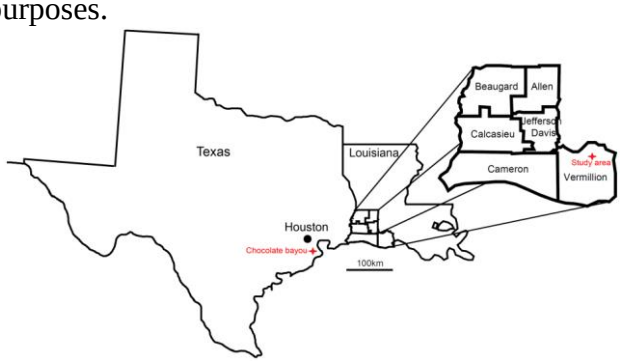

Figure 8: Approximate location of the study area. The data collected from Beulah Simon No. 2 well have been used for this study (adapted from Szalkowski, 2003 and Dobson et al., 1980).

The rock composition of the Camerina A sand in Vermilion Parish was not reported in the Beulah Simon No.2 well investigations. The Camerina A sandstone, however, belongs to the Frio formation which is one of the major oil and gas producing formations in the Texas and Louisiana Gulf Coast. For this study, a rock composition was assumed based on studies of the Frio formation in the Texas Gulf Coast with similar reservoir temperatures and depths (Figure 8).

A study in the Frio formation conducted by Land and Milliken (1981) in the Chocolate Bayou Field, Brazoria County, Texas, shows that 65 volumetric percent of the rock consists of mineral grains and the remainder is pore space and diagenetic products. The grains portion includes quartz (40 percent), albite (10 percent) and rock fragments (15 percent). The subsurface temperature is approximately 150 ºC.

Lynch (1996) studied the Frio sandstone diagenesis near Corpus Christi, Texas. This study showed that illite/smectite matrix (4.4 percent), chlorite (3.2 percent), quartz overgrowths (1.5 percent), calcite (11 percent) and kaolinite (1.3 percent) are the diagenetic products in the Frio sandstone. Percentages are bulk volume. At the target depth, around 14,000 ft., no kaolinite was found. The absence of kaolinite in the most deeply buried sandstones is probably the result of diagenetic loss of kaolinite in favor of highly illitic I/S, chlorite, and albite (Lynch, 1996) at higher temperatures. In another study on the smectite to illite reaction in Frio shale, Lynch (1997) showed that the illite and smectite percentage in illite/smectite matrix is 80 and 20 percent, respectively. Based on these studies and assuming that the composition of the rock fragment is the same of the remainder of the reservoir sandstone, the rock composition that has been used in the models is presented in Table 3.

Table 1: Geological and petrophysical information of study area (Dobson et al., 1980).

Total depth	15,265 ft
Formation	Camerina (Upper Oligocene)
Perforated interval	14,674-14,770 ft
Original reservoir pressure	13,015 psi at 14,722 ft
Original reservoir temperature	130 °C (266 °F)
Total dissolved solid	103,925 ppm
Net sand thickness	266 ft
Porosity	17.4 percent
Permeability	12 md

Table 2: The brine composition that has been used in the models. All concentrations are in mg/l (Dobson et al., 1980).

Density (gr/ml)	1.066
pH	6.61
Total Dissolved Solids	103,925
Calcium	7,869
Magnesium	910
Bicarbonate (HCO_3)	606
Chloride (Cl)	50,300
Total Iron (Fe)	33
Dissolved Silicate (SiO_2)	92
Boron (B)	89.6
Lead (Pb)	7.73
Sodium (Na)	32,190
Potassium (K)	454
Barium (Ba)	30.4
Sulfate (SO_4)	444

Table 3: The rock composition by volume percentage that has been used in the models.

Pore volume	17.4
Quartz	47.9
Calcite	12.7
Albite	11.5
Illite	5.6
Chlorite	3.8
Smectite	1.1

Possible water-rock reactions in South Louisiana were studied by Ausburn and Hanor (2013). They used water sample data from six oil and gas fields located in Vermilion, Iberia, and St. Mary parishes, Louisiana. In their study, water compositions were found to be partially buffered by calcite/dolomite and chalcedony. It also was found that there is potential for barite precipitation due to mixing of barium and sulfate rich waters (Ausburn and Hanor, 2013).

The impact of brine-rock interactions on geothermal reservoir properties has been investigated in a study by Safari-Zanjani et al., (2013). In that study, interactions between geothermal fluid and reservoir rocks in the West Hackberry field, Cameron Parish, Louisiana were examined using geochemical modeling. A porosity change about 5 percent was anticipated by geochemical reaction models (Safari-Zanjani et al., 2013).

3.2. Simulation of fluid-rock interaction

The modeling software package, Geochemist's Workbench, developed by Bethke (2008) has been used in this research. This software can model chemical reactions, trace reaction processes, model reactive transport and plot the results of these calculations.
Geochemist's Workbench (GWB) is able to use different thermodynamic databases. Each database contains the properties of minerals, aqueous species, and gases, equilibrium constants for reactions to form these species, and data required to calculate activity coefficients (Bethke and Yeakel, 2012). The default dataset employed by GWB is the LLNL thermodynamic database. This dataset was compiled by the geochemical modeling group at Lawrence Livermore National Laboratories (LLNL). The temperature range in LLNL thermodynamic dataset spans from 0 to 300 °C and it contains data related to high temperature minerals like saponite and nontronite. The bulk of the modeling was performed using this dataset.

GWB is also able to employ the database designed by the U.S. Geological Survey for the PHREEQC software package. The PHREEQC database does not include saponite and nontronite minerals and only goes up to 100 °C. This dataset was utilized for comparison purposes.

The rock-brine reactions have been modeled with both titration and kinetic paths. In the titration reaction path, the program repeatedly adds a small aliquot of reactants and then recalculates the equilibrium state the system. There is no time component in this reaction path. In the kinetic reaction path, kinetic rate laws control the rates at which reactions proceed (Bethke and Yeakel, 2012).

In accordance with the planned heat exchanger specifications (Feng et al., 2015), the initial and final temperatures of the brine as it travels through the exchanger have been assumed to be 130 and 100 °C, respectively. To investigate the precipitation risk inside the heat exchanger brine was assumed to be cooled down from 130 to 100 °C.

To combine geochemical reaction with brine flow in reservoir, rock-brine geochemical reactions have been modeled in consecutive steps. After the earliest rock-brine interaction, the resulting minerals are separated and the next reaction step happens between the minerals resulting from last reaction step and the initial brine composition (the brine composition does not change). Reactions have been modeled for five steps, since the results for total minerals in the system show only minor changes after five consecutive steps. Chemical equilibrium between the brine and the minerals is achieved at each step.

The first rock-brine interaction happens in the vicinity of the heat exchanger where brine at 100 °C encounters reservoir rock with 130 °C. Assuming a constant temperature of 130°C for the reservoir, the subsequent rock-brine interactions happen with constant temperature of 130 °C.

To investigate the precipitation risk between the heat exchanger and the wellbore, a temperature drop from reservoir temperature, 130 °C, to heat exchanger output temperature, 100 °C, has been modeled. Results show that the total precipitated mineral mass is about 0.47 gram for every 1122 grams of solution. Therefore, the mass of precipitation inside the heat exchanger is close to 0.42 gr per kg brine.

Most of this precipitation is dolomite (Table 4). Quartz, barite and nontronite are other formed precipitates. Assuming 5 kg per second (adopted from Feng et al, 2015) as the brine flow rate to the heat exchanger and 70 years as the anticipated life time of a geothermal power plant, 4.64×10^{6} kg of precipitate is expected to be formed, which is 68 times the heat exchanger volume. Although due to high flow rates much of this precipitation may be carried outside the exchanger to the reservoir rather than form scale in the heat exchanger, the potential of scaling inside the heat exchangers should be considered carefully in heat exchanger design.

Table 4: Expected precipitates in heatexchanger due to the temperature drop (gr per kg brine).

Dolomite	0.31
Quartz	0.062
Barite	0.048
Nontronite-Mg	2.65×10^{-5}

Geochemical reactions between rock and brine have been modeled in five consecutive steps (Run A). The changes in the mass of major minerals with reaction steps are shown in Figure 9. Considering the 17.4 percent initial reservoir porosity, the rock to brine volume ratio is 4.75. Minerals shown in step 0 of this graph indicate the initial rock composition.

The main change in rock composition can be seen in the first reaction step. In this step, the brine temperature rises from 100 °C to reservoir temperature, 130 °C. Quartz (not shown here), which is the dominant mineral in the initial rock composition, shows a slight increase after five reactions increasing from initial value of 8046 g to 8227 g after the fifth reaction. Calcite also shows no noticeable change, decreasing from an initial value of 2183 gr to 2177 gr after the fifth reaction. Albite, however, shows a sharp drop in the first reaction step and this reduction is

continued until the last reaction step. In the first rock-brine interaction, illite, smectite, and chlorite are transformed to muscovite, saponite-Ca, nontronit-Ca and paragonite.

Illite is a non-expanding, clay-sized, micaceous mineral which structurally is similar to muscovite. Transformation of illite to muscovite has been shown by many studies (Gharrabi et al. 1998, Hunziker et al., 1986, Verdel et al., 2012). Muscovite, $KAl_3Si_3O_{10}(OH)_2$, and paragonite, $NaAl_3Si_3O_{10}(OH)_2$, both are micaceous minerals. The crystal structures of paragonite and muscovite are nearly identical (Zen and Albee, 1964). Saponite is the most abundant of the trioctahedral smectites and is found in a number of Mg-rich geologic environments (Whitney, 1983). Nontronite-Ca is the iron-rich member of the smectite group. In the first reaction step, original smectite has been converted to saponite-Ca and nontronite-Ca.

As discussed above, the models show the formation of pure end member layer silicates, such as saponite and paragonite. Different assumptions result in similar predictions, although the specific pure end members may vary.

We believe that alteration of the initial clay mineral assemblage of chlorite and illite smectite, as well as albite, to clay minerals that more closely resemble the pure end members is likely due to the lower free energy state which would result. However, we do not believe that at these temperatures, rather than the metamorphic temperatures at which the pure end members are found in nature, the transformation will be complete. Rather, new clay minerals that are closer to but not completely represented by the pure end members will be formed. In this work, we refer to the formation of muscovite, paragonite, talc, etc. but these are simply proxies for the actual clay minerals formed.

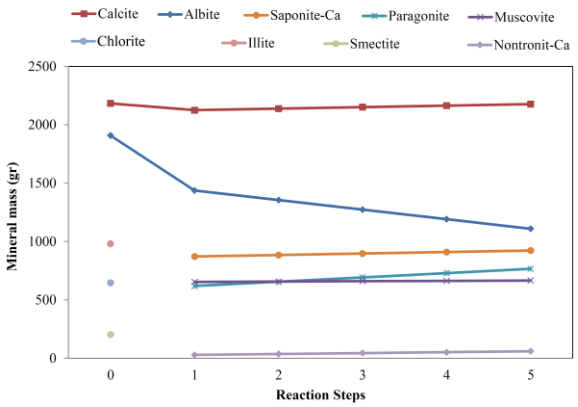

Figure 9: The changes in major minerals mass with reaction steps in run A. Reaction step 0 shows the initial rock composition. The main change happens in the first reaction where the temperature changes from 100 to 130 °C. In steps from 2 to 5, temperature is constant and equal to 130 °C.

A question that has to be answered is whether the system was initially in equilibrium with the brine and minerals shown in Table 2 and Table 3. To address this question, the brine-rock reactions were modeled with a similar approach but this time without changing temperature. Temperature in all reaction steps was constant and equal to reservoir temperature (130 °C). The results of this case (Run B) are similar to those obtained from Run A. It can be concluded that in addition to temperature change, pursuing a lower free energy state is a reason for the predicted mineral transformations.

For further investigation, the final rock composition in run B was assumed to be close to equilibrium and reactions from that point have been modeled and called run C. The results for this case show small changes. A decrease of albite and an increase of paragonite can still be seen in these results.

The clay portion forms 10.5 percent of total initial rock volume. This volume percentage is increased to 13.4 percent after five reaction steps for run A. Most of the initial clay minerals are chlorite and illite which are non-expandable minerals and the share of expandable mineral, smectite, is low. After reactions, however, a considerable amount of expandable clay minerals, saponite-Ca and nontronite-Ca, are formed. Transformation of chlorite to smectite has been observed in previous studies (e.g. Senkayi et al., 1981).

Albite transformation to clay minerals is the reason for the increase in the clay content. Albite is a member of the feldspar family. The transformation of the plagioclase feldspar to clay minerals has also been reported in previous studies (e.g. Frank-Kamenetskii, 1980). The amount of albite decreases continuously in all runs in different steps. In run A the amount of albite decreases from an initial mass of 1908 grams to 1109 grams. Assuming that aluminum is conserved in all reactions, tracking the location of aluminum in the reaction steps is a useful way to illustrate the change in aluminum silicate minerals. As it can be seen in Figure 10, in reaction steps 1 to 5 the total amount of albite decreases while paragonite increases. Other Al-contained minerals have small changes after the first step.

Our interpretation of these results is that the combination of repeatedly exposing the rock to fresh brine, and a change in the brine temperature from 100 to 130 °C results in two changes. The first is alteration of smectite, illite and chlorite to purer layer silicates, represented by saponite, nontronite, paragonite and muscovite. The second change is dissolution of albite and the formation of additional paragonite, a sodium-bearing sheet silicate, as well as additional quartz. The combination of these two changes results in an increase in clay volume from approximately 10 percent to 13 percent bulk volume.

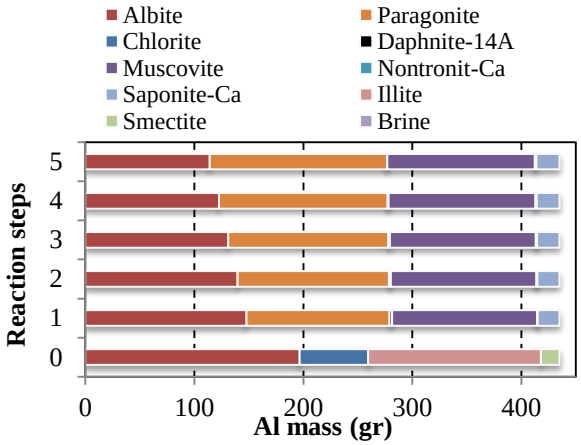

Figure 10: The change in total Al mass in run A. In all reaction steps the total amount of albite decreases while paragonite increases. Other Al-contained minerals have small changes after the first step.

To validate these results, modeling was performed varying the change in temperature (ΔT between 30 and 70 °C), the pH (4.61 to 6.61), HCO_3 concentration (60.0 to 6060 mg/l), and sodium concentration in the brine (16,095 to 64,380 mg/l), the amount of albite initially present (0 to 23% by volume) and the amount of initial clay present (0 to 21% by volume). Modeling was also performed using the PHREEQC thermodynamic data base in place of the LLNL database. In addition, runs were made in which the formation of saponite, nontronite and paragonite was prevented.

With two exceptions, all the runs showed a similar increase in clay content from approximately 10 to 13 percent, although the specific clay minerals formed varied.

The two exceptions were: (a) a run made with twice the Na concentration present compared to the initial case (64,380 mg/l). In this case, the alteration of albite to paragonite did not occur, as the higher Na concentration stabilized the albite. The total clay concentration decreased from 10 to 9 percent and the amount of albite increased, reflecting a reversal of the reaction albite → paragonite: (b) a run made which prevented the formation of paragonite. In this case, no sodium containing layer silicate formed, and the amount of albite stayed constant. The volume of total clay only increased from 10 to11 percent.

The situation in case (a) could be expected to occur in the vicinity of salt domes in the area studied, and indicates that the concentration of sodium in the brine could be a variable affecting the suitability of different locations for projects of this type. The exception is (b) which is not believed to be a realistic scenario – the exclusion of any sodium-bearing sheet silicates is not believed to be a likely occurrence.

To this point reactants were added to (or removed from) the system at arbitrary rates by the software. The reaction progress is also measured parametrically in terms of the reaction progress variable, ξ, which is dimensionless and varies from zero to one from the beginning to end of the path (Bethke, 2008).

The obtained results so far are based on thermodynamic calculations which deal with free energies of reactions. On the other hand, kinetics deals with the rate of a chemical reaction and the reaction mechanism. Thermodynamic principles give us an idea of whether a reaction is able to occur in a given system, while kinetics tells us how fast. To investigate how fast the anticipated reactions could happen and whether these changes will be effective in a geothermal power plant life span, brine-rock interactions were modeled with kinetic data.

The first step to model reactions with kinetics is to select the applicable rate law. A rate law reflects the idea of how a reaction proceeds on a molecular scale and requires that a mineral's specific surface area (cm^2/g) and rate constant (mole cm^{-2} s^{-1}) should be assigned. A rate constant depends on temperature and pH and is not the same for dissolution and precipitation. Therefore, it is not uncommon to find different rate constants for a specific mineral.

The rate constants used here for modeling the anticipated reactions have been adopted from other research work (Table 5). For all minerals, except paragonite and muscovite the dissolution rate constant was used for precipitation. For nontronite the constant for saponite was used.

Table 5: The rate constants used for kinetics modeling. For patagonite and muscovite numbers are for precipitation.

Quartz	$1.93\times10^{-14*}$	Rimstidt and Barnes, 1980
Albite	6.3×10^{-13}	Knauss and Wolery, 1986
Illite	2×10^{-18}	Alekseyev, 2007
Smectite	4×10^{-17}	Alekseyev, 2007
Calcite	2×10^{-8}	Pokrovsky et al., 2009
Chlorite	4×10^{-16}	Smith and Carroll, 2014
Saponite-Ca	1×10^{-14}	Savage et al., 2002
Paragonite	1.02×10^{-13}	Soler and Lasaga, 1998
Muscovite	1.02×10^{-13}	Soler and Lasaga, 1998

**The rate constant unit for all minerals is mole cm^{-2} s^{-1}*

Kinetic models have been run with three different approaches; in the first approach, dissolution has been assumed to be the rate-limiting step. In other words, it is assumed that the reactant dissolution happens slowly whereas product precipitation occurs instantaneously. Therefore, there is no need to set the precipitation rate constants for products.

In the second approach, precipitation rate constants were also considered in the kinetics. Setting a rate constant for products before formation is a challenge. A supersaturated mineral that has not yet formed will have no surface area, and as a result its precipitation rate would be zero. This problem was solved by assuming a very small mass of products in the initial rock composition. From the titration path results it is already known that the products which are not present in the initial rock composition are saponite-Ca, nontronite-Ca, paragonite and muscovite. By including 0.01 gram of these minerals among reactants, their precipitation rate constant can be set in the model.

In the third approach, the precipitation rate constants were considered in models by setting a nucleus density for products. Nucleation is the formation of a new phase, here the formation of a solid phase from a supersaturated solution.

All three approaches show very similar results. In the second and third approaches, in which precipitation rate constants are considered, products are formed slightly slower than the first approach. The results for the second approach are shown in Figure 11.

The first rock-brine reaction was modeled with a time span from 0.5 year to 5000 years. Titration results have also been shown on the graph (Figure 11). As it can be seen after almost 50 years most of the reactions have been completed, but for illite and muscovite almost 100 years are needed to complete the reaction. After 100 years there is almost no change in the products and results are similar to the titration results. Quartz shows small changes and has not been shown on the graph. Based on these results, the anticipated changes which lead to a 3 percent increase in the clay volume will be achieved in almost 70 years. This is in the life span of a geothermal power plant.

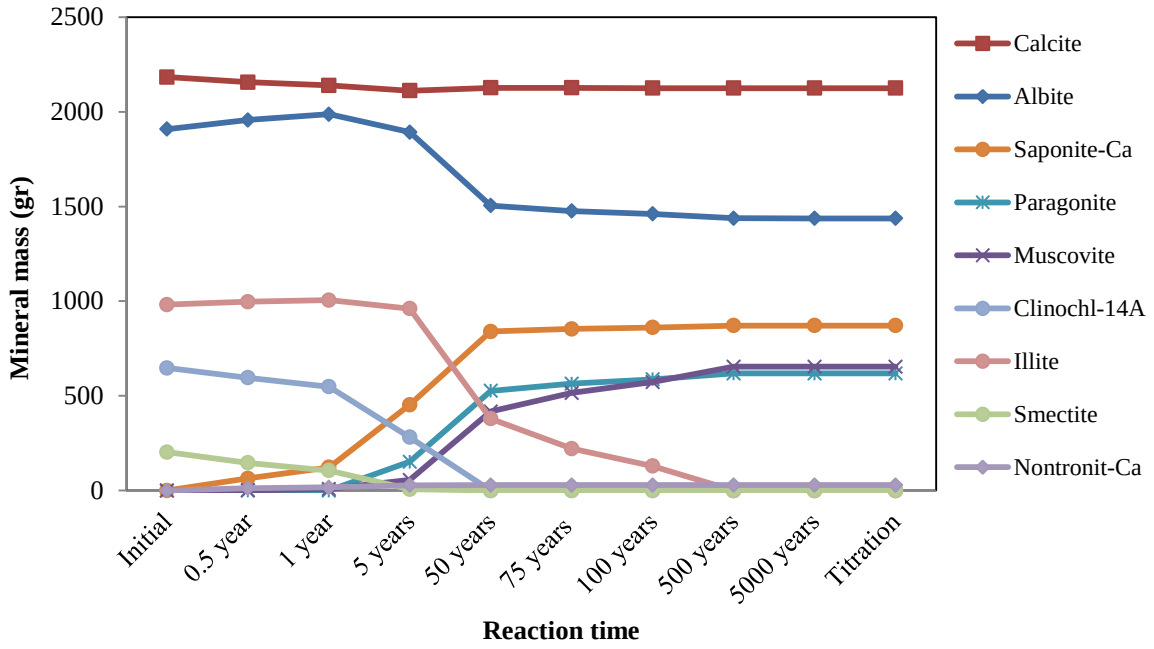

Figure 11: The changes in major minerals mass with time in the second approach of kinetics modeling. The reactants precipitation rate constants were also included in the models. Consideration of very small initial amount of products in the rock composition makes it possible to include precipitation rate constants in the models. Almost 50 years are needed for most reactions to become completed.

5 Discussion

The modeling results discussed above show that equilibrating the initial rock composition with the brine from the Beulah Simon No. 2 well causes a transformation of the initial illite/smectite and chlorite clay compositions to a mixture of purer clay end members with lower free energies. This is accompanied by dissolution of albite to further increase the amount of clay present. Varying the starting fluid composition over a wide range of pH, HCO_3 and Na does not affect the overall results. The reactions do not require a change in temperature, but occur when exposing the fluid to the rock. While the exact clays formed vary, an overall increase in clay content occurs using two different thermodynamic databases and regardless of whether specific clay minerals are prevented from forming during the modeling. Kinetic modeling shows that this transformation and increase in the clay minerals present should occur in a time span of approximately 70 years.

An apparent contradiction in these results is the expected time span of the reaction from the modeling (approximately 70 years) compared to the fact that the brine has had millions of years to equilibrate with the rock mineralogy. Previous studies (Land and Milliken, 1981, Hanor, 2001, Ausburn and Hanor, 2013) show that fluid composition in similar formations are partially buffered by the rock mineralogy. There are several possible explanations:

1) The fluid composition is erroneous, especially the pH, which is very difficult to determine at subsurface conditions. However, varying the initial fluid composition substantially still leads to the same results.
2) The thermodynamic data are not appropriate, predicting the formation of unlikely pure phases. However, two different databases, and suppressing different minerals in the modeling, show similar results. A possibility is that mixed layer illite/smectite is a

distinct phase with a specific free energy which was not included. However, the data utilized are the best available from the aqueous geochemical community.

3) Pore waters in isolated layers in the rock are at equilibrium, but the sample obtained from the well mixed fluids from several of these layers together, resulting in a water sample that is not in equilibrium with the rock. However, the results of varying the initial fluid composition still makes this an unlikely reason.
4) The rock composition assumed here is not the exact rock composition in the studied field. However, varying the initial rock composition shows similar results. In addition, the comparison of applied rock composition with similar fields assures that the assumed rock composition here should be close enough to reality.
5) The kinetic modeling predicts a much shorter time span than should be expected. This should be resolved by experimental work with the actual fluid composition and rock compositions.
6) Pore water is in equilibrium with meta stable phases when stagnant. This includes concentration differences between micropores in clay and larger intergranular pores due to double layer effects. Flow through the larger pores at the high rates required by the project may disturb this equilibrium and initiate dissolution of the original clay minerals and albite and precipitation of new clay phases to achieve a lower free energy state.

From an engineering viewpoint, the most important alteration of the rock is a change from the original morphology of clay largely contained in partially altered rock fragments and authigenic grain coating clay to new precipitates, which would be expected to have pore lining or pore bridging morphologies. This change in morphology, accompanied by an increase in total clay content from approximately 10.5 to 13.5 percent pore volume, would be expected to have a substantial negative effect on permeability (Neasham, 1977).

The next phase of this study will be focused on determining the change in petrophysical rock properties, specifically permeability, due to the expected transformations in the rock mineralogy. Since the creation of additional pore lining and pore bridging clay will reduce permeability and materially impair the project, this is a necessary engineering evaluation. Experimental work to validate the modeling, especially the kinetics, is recommended as a future study.

6 Conclusions

1. Reacting the brine from the Beulah Simon No. 2 well with a rock composition inferred from the Frio Formation at similar depths and temperatures from other wells results in an increase in clay minerals from about 10 percent by volume to 13-14 percent by volume. This increase occurs over a wide variation in pH, and bicarbonate concentrations. A similar increase is observed when using two different thermodynamic data bases.
2. The modeling shows that the initial assemblage of albite, illite, chlorite and smectite would be expected to alter to a mixture of smectite-like minerals (nontronite and saponite) and illite-like minerals (muscovite and paragonite). Continued alteration of albite to paragonite and quartz occurs with each additional reaction step. The presence of pure nontronite, saponite, muscovite and paragonite is not expected in a natural setting, but are proxies for actual expandable and non-expandable clay minerals for which free energy data is not available.
3. Kinetic modeling shows that this increase can be expected to occur within a time span of approximately 70 years, close to the expected lifespan of the project.

4. The exact clay minerals formed vary depending on the data base, which minerals are allowed to form in the reactions, and the temperature.
5. The increase in total clay is primarily the result of albite altering to clay. The exact clay mineral formed depends on the variables described in (4). High sodium content in the brine reduces the amount of clay formed by reversing the albite to clay transformation.
6. A temperature drop may cause precipitation inside the heat exchanger. The impact of this on the heat exchanger will vary with flow rates and the concentration of dissolved sodium and other ions in the fluid. An increase in brine salinity will increase the risk of precipitation in heat exchangers dramatically.
7. In the models, the geochemical system is in equilibrium with regard to quartz and calcite but feldspar equilibrium depends on the concentration of Na in the brine. With a lower amount of Na, feldspar (albite) transformation to clay minerals is expected by the models while with the increase of Na amount, this reaction will progress in reverse direction and a clay mineral to albite conversion is expected.

References

Alekseyev, V. A., (2007), "Equations for the Dissolution Reaction Rates of Montmorillonite, Illite, and Chlorite", Geochemistry International, Vol. 45, No. 8, pp. 770–780.

Ausburn, M.E., (2013), "Controls on the Composition of Saline Formation Waters from Coastal and Offshore Louisiana", Master's Thesis, 95p.

Ausburn, M.E., Hanor, J.S., (2013), "Geochemical Characterization of Formation Waters and Sediments from an Area of South-Central Louisiana with Implications for Geothermal Energy Production", Gulf Coast Association of Geological Societies Transactions, Vol. 63, pp. 67–77.

Berner, R.A., (1971), "Principles of Chemical Sedimentology", McGraw-Hill, 240p.

Bethke, C.M., (2008), "Geochemical and Biogeochemical Reaction Modeling (Second Edition)", Cambridge University press, 543p.

Bethke, C.M. and Yeakel, S., (2012), "Reaction Modeling Guide", Aqueous Solutions, LLC, 162p.

Burton, J.H., Krinsley, D.H., and Pye, K., (1987), "Authigenesis of Kaolinite and Chlorite in Texas Gulf Coast Sediments", Clays and Clay Minerals, 35, 291-296.

Dobson, R. J., Hartsock, J. H., McCoy, R. L., and Rodgers, J. A., (1980), "Investigation and Evaluation of Geopressured-Geothermal Wells - Final Report, Beulah Simon No. 2 Well, Vermilion Parish, Louisiana, Volume I: Completion and Testing", Gruy Federal, Inc., Houston, Texas.

Dullien, F.A.L., (1979), "Porous Media, Fluid Transport and Pore Structure", Academic Press, 396p.

Feng., Y., Tyagi, M., White, C.D., (2015), "A Downhole Heat Exchanger For Horizontal Wells In Low-Enthalpy Geopressured Geothermal Brine Reservoirs", Geothermics, Vol. 53, pp. 368-378.

Frank-Kamenetskii, V.A., Kotov, N.V., and Rjumin, A.A., (1980), "The Transformation of Feldspar and Muscovite to Clay Minerals in (Ca, Mg)-Carbonated Bearing Hydrothermal Media", Clay Minerals, 15, 263-274.

Gallup, D.L., (1996), "Brine pH modification scale control technology", Geothermal Resources Council Transactions, 20, 749–755.

Gallup, D.L., (2009), "Production engineering in geothermal technology: A review", Geothermics, 38, 326–334.

Geothermal Energy Association, (2014), "2014 Annual U.S. & Global Geothermal Power Production Report", 25p.

Gallup, D.L., Featherstone, J.L., (1995), "Control of NORM deposition from Salton Sea geothermal brines", Geothermal Science & Technology, 4, 215–226.

Gharrabi, M., Velde, B., and Sagon, J.P., (1998), "The Transformation of Illite to Muscovite in Pelitic Rocks: Constraints from X-Ray Diffraction", Clays and Clay Minerals, 46, 79–88.

Goyal, K.P., and Conant, T.T., (2010), "Performance history of The Geysers steam field, California, USA", Geothermics, 39, 321–328.

Gray, T.A., (2010), "Geothermal Resource Assessment of the Gueydan Salt Dome and the Adjacent Southeast Gueydan Field, Vermilion Parish, Louisiana", a Master's thesis submitted to the graduate faculty of Louisiana State University.

Hanor, J.S., (2001), "Reactive Transport Involving Rock-buffered Fluids of Varying Salinity", Geochimica et Cosmochimica Acta, 65, 3721–3732,

Hunziker, J.C., Frey, M., Clauer, N., Dallmeyer, R.D., Friedrichsen, H., Flehmig, W., Hochstrasser, K., Roggwiler, P., and Schwander, H., (1986), "The Evolution of Illite to Muscovite: mineralogical and Isotopic Data from the Glarus Alps, Switzerland", Contributions to Mineralogy and Petrology, 92,157–180.

Knauss, K.G. and Wolery, T.J., (1986), "Dependence of albite dissolution kinetics on pH and time at 25 °C and 70 °C", Geochimica et Cosmochimica Acta, 50, 2481–2497.

Land, L.S., and Milliken, K.L., (1981), "Feldspar diagenesis in the Frio Formation, Brazoria County, Texas Gulf Coast", Geology, Vol. 9, 314–318.

Lynch, F.L., (1996), "Mineral/Water Interaction, Fluid Flow, and Frio Sandstone Diagenesis: Evidence from the Rocks", AAPG Bulletin, Vol. 80, No. 4, 486–504.

Lynch, F.L., (1997), "Frio Shale Mineralogy and the Stoichiometry of the Smectite-to-Illite Reaction: the Most Important Reaction in Clastic Sedimentary Diagenesis", Clays and Clay Minerals, Vol. 45, No. 5, 618-613.

Manceau, A., Ildefonse, Ph., Hazemann, J.L., Flank, A.M., Gallup, D.L., (1995), "Crystal chemistry of hydrous iron silicate scale deposits at the Salton Sea geothermal field", Clays and Clay Minerals, 43, 304–317.

Mitchell, J.K., and Soga, K., (2005), "Fundamentals of Soil Behavior", John Wiley & Sons, 577p.

Morris K.A., and Shepperd C.M., (1982), "The Role of Clay Minerals in Influencing Porosity and Permeability characteristics in the Bridport Sands of Wytch Farm, Dorset", Clay Minerals, 17, 41-54.

Neasham, J.W., (1977), "The Morphology of Dispersed Clay in Sandstone Reservoirs and its Effect on Sandstone Shaliness, Pore Space and Fluid Flow Properties", 52nd Annual Fall Technology Conference and Exhibition of the Society of Petroleum Engineers of AIME, Denver, Colorado.

Pokrovsky, O.S., Golubev, S.V., Schott, J., and Castillo, A., (2009), "Calcite, Dolomite and Magnesite Dissolution Kinetics in Aqueous Solutions at Acid to Circumneutral pH, 25 to 150 °C and 1 to 55 atm pCO_2: New Constraints on CO_2 Sequestration in Sedimentary Basins", Chemical Geology, 265, 20-32.

Rimstidt J. D., and Barnes H. L., (1980), "The Kinetics of Silica–Water Reactions", Geochimica et Cosmochimica Acta, 44, 1683–1699.

Safari-Zanjani, M., White, C.D., and Hanor, J.S., (2013), "Impacts of Rock-brine Interactions on Sandstone Properties in Lower Miocene Sediments, Southwest Louisiana", Thirty-Eighth Workshop on Geothermal Reservoir Engineering Stanford University, Stanford, California.

Savagea, D., Noyb, D., and Mihara, M., (2002), "Modelling the Interaction of Bentonite with Hyperalkaline Fluid", Applied Geochemistry, 17, 207–223.

Senkayi, A.L., Dixon, J.B., and Hossner, L.R., (1981), "Transformation of Chlorite to Smectite through Regularly Interstratified Intermediates", Soil Science Society of America Journal, Vol. 45, No. 3, 650-656.

Smith, M.M., and Carroll, S.A., (2014), "Experimental Determination of Chlorite Kinetics at Geothermal Conditions", PROCEEDINGS, Thirty-Ninth Workshop on Geothermal Reservoir Engineering Stanford University, Stanford, California, February 24-26.

Szalkowski, D.S, (2003), "Low Salinity Waters in Deep Sedimentary Basins", a Master's thesis submitted to the graduate faculty of Louisiana State University.

"Thermodynamic Datasets." Geochemist's Workbench Thermodynamic Datasets. Web. 26Feb.2015. <http://www.gwb.com/thermo.php>.

Ungemach, P., (2003), "Reinjection of Cooled Geothermal Brines into Sandstone Reservoirs", Geothermics, 32, 743–761.

Verdel, C., van der Pluijm, B.A., and Niemi, N., (2012), "Variation of Illite/Muscovite $^{40}Ar/^{39}Ar$ Age Spectra during Progressive Low-Grade Metamorphism: An Example from the US Cordillera", Contributions to Mineralogy and Petrology, 164, 521-536.

Whitney, G., (1983), "Hydrothermal Reactivity of Saponite", Clays and Clay Minerals, Vol. 31, No. 1, 1-8.

Zen, E-an., Albee, A.L., (1964), "Coexistent Muscovite and paragonite in Pelitic Schists", The American Mineralogist, 49, 904-925.

Task 3 – Downhole Energy Conversion

Design Details of Zero Mass Withdrawal Concept with Energy Extraction in Geopressured Geothermal Brine Reservoirs

A downhole heat exchanger inside a deviated wellbore with a dual completion design for electricity production from low enthalpy geothermal reservoirs was numerically studied (Figure 12). Fluid flow from the porous media (reservoir) into and out of the deviated well was simulated using a nodal analysis approach. Friction, acceleration and gravitational pressure losses inside of the pipe were also modeled. Two different completion designs viz. perforated and frac pack completions were studied. Inflow and tubing performance relationship curves for both production and injection completions were then used to calculate the pump capacity requirements.

Additionally, reservoir response to cooling was studied. A representative case of a geopressured reservoir located in Vermilion Parish, Louisiana was used for the design parameter reservoir conditions. It was determined that reservoir temperature after thirty years continuous ZMW operation would reduce from 126 °C to 115 °C.

The Zero Mass Withdrawal principle (Feng et al., 2015) requires only a single well to complete the proposed system. This method applies geofluid circulation inside of the wellbore, rather than extraction to the surface. This eliminates several traditional problems associated with geothermal power plants, such as heat leakage off the well to the underground conjugated layers, and to the ambient air at the surface; pipe clogging due to mineral precipitation; and necessary cleaning used geo-fluid before pumping back to the reservoir. The well scheme is chosen as a vertical well with a deviated offset.

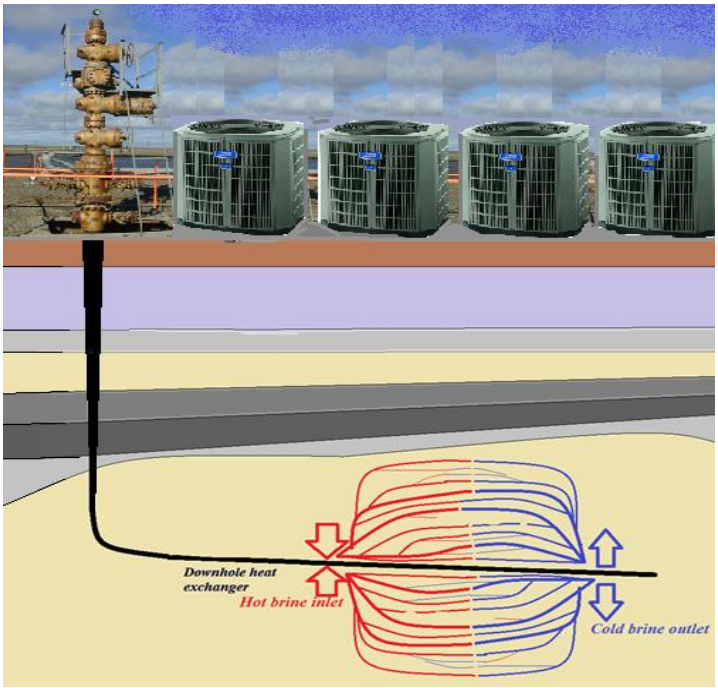

Figure 12: Zero mass extraction power unit schematic

Three main energy transformation loops are recognized in the scheme (Figure 13). The Heat Extraction Loop (HEL) is defined by reservoir brine circulation through the downhole heat exchanger (DHE); the Power Generation Loop (PGL) is located in the vertical section of the well and it is here where the thermal energy of the binary fluid is transformed into electric energy. The only part of the system installed at the surface is a Heat Rejection Loop (HRL). Here excessive thermal energy from the binary fluid is removed to the ambient air.

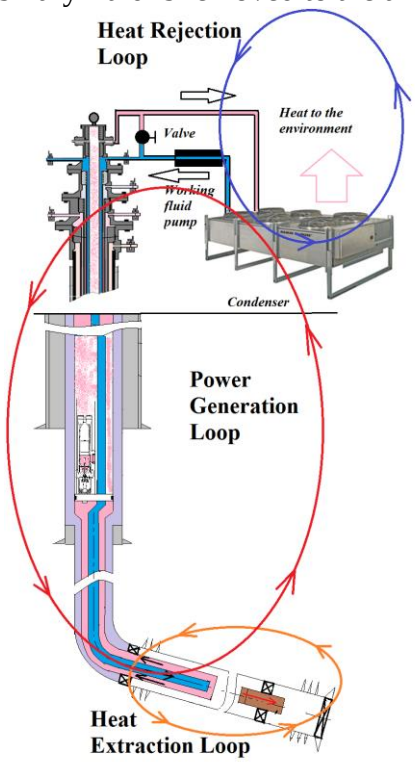

Figure 13: System schematic

Heat Extraction Loop

The horizontal offset has a production and an injection side at the heel and toe regions, respectively. The distance between was analyzed with a desire to avoid influx of cooled brine from the injection into the production area. An electric submersible pump (ESP) pulls brine from the reservoir through the production side to the injection side of the well and discharges the geofluid back into the reservoir. There is a risk of sand production if the reservoir rock is unconsolidated. To avoid complications a gravel pack is considered for the production completion as a protection system. The well may have some inclination angle according to the reservoir dip direction.

The DHE is installed into the cased horizontal offset at the reservoir depth and has a coaxial pipe scheme. The approximately horizontal orientation of the well gives the maximum heat transfer area exposed directly at the heat source to increase thermal efficiency. The length of the DHE depends on working fluid choice and geometry of the pipes. The working fluid and geofluid do not mix with each other, and only have thermal interaction through the DHE.

Power Generation Loop

The working fluid loop is driven by a conventional electric pump, installed in the vertical portion of the well. This location has high density working fluid and, thus, requires less power to apply for the pump. It directs cooled working fluid through the insulated tubing of 5-inch OD. The working fluid remains in a dense phase all the way down to the well depth. The working fluid then increases in temperature in the DHE and low density working fluid then leaves the horizontal offset and travels vertically up toward the turbine inside the production casing. The turbine-generator assembly is installed in a large capacity casing near the surface.

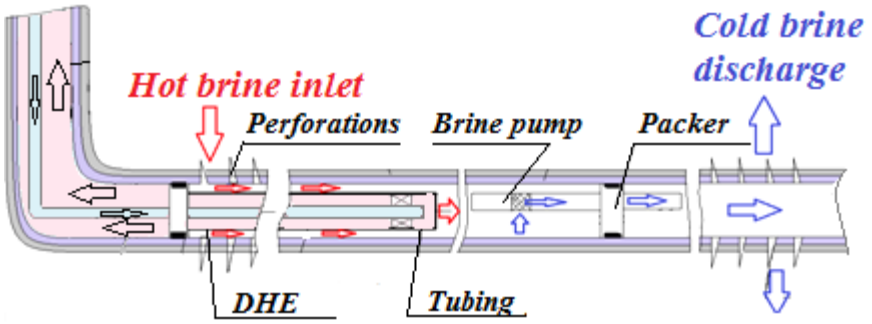

Figure 14: Completion design scheme for horizontal well with downhole heat exchanger installed into the production side.

Heat Rejection Loop

A condenser is used to convert vapor to fluid. This stage can be completed by commercially available air o liquid coolers. The number of coolers would depends on ambient air conditions, and binary fluid flow rates.

Reservoir Application Case Study

A geopressured reservoir located near the Gueydan salt dome in Vermillion Parish, Louisiana was used as a reservoir prototype. The true vertical depth (TVD) is between 4253 and 4479 meters (13,953 – 14,695 ft) and the dip angle varies from 1.2 to 28 degrees. The 100 m (300 ft.) thickness A-sand is characterized by 12 mD permeability and porosity which varies between 9 and 31 percent (Gray, 2010). The temperature gradient consists of two parts: 23.04 °C/km from the surface to the top of the geopressured zone at 12,556ft (3827m); and 28.9 °C/km through the geopressured zone.

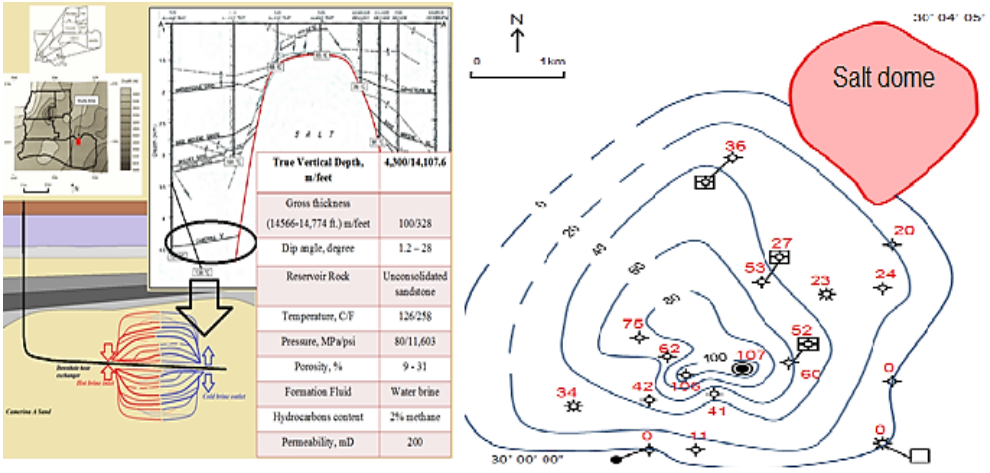

Figure 15: Camerina A-sand is a potential low-enthalpy geopressured reservoir located in Vermilion Parish, Louisiana. (Modified from Gray, 2010).

Heat Extraction Loop

Well Plan

In this project three types of pipes are used. First, casings protect the entire well from the subsurface formations. Then, the production strings with changing diameter along the well length hold the PGL. The last is the cold stream tubing going from the surface to the end of DHE.

The Overall Design Scheme

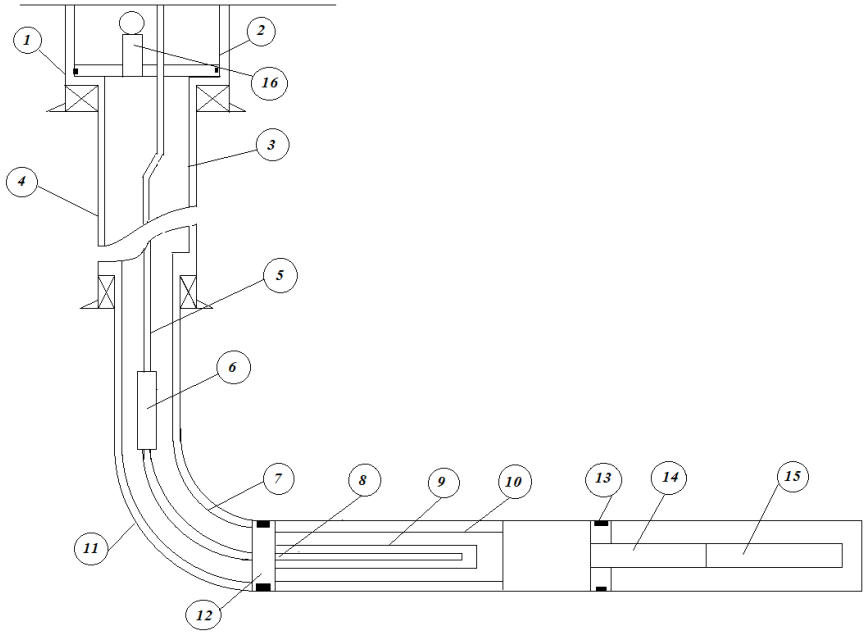

Figure 16: Overall specification

Table 6 Overall specification

#	Name
1	Surface casing
2	Production casing 16” OD
3	Production casing 9 5/8” OD
4	Intermediate casing 13 5/8” OD
5	Production tubing 5” OD
6	ESP
7	Production casing 6.625” OD
8	Production tubing 2” OD
9	Tubing 4” OD
10	Screen pipe
11	Casing 9 5/8”
12	Packer
13	Packer
14	ESP
15	Casing 6 5/8”

Casing Design

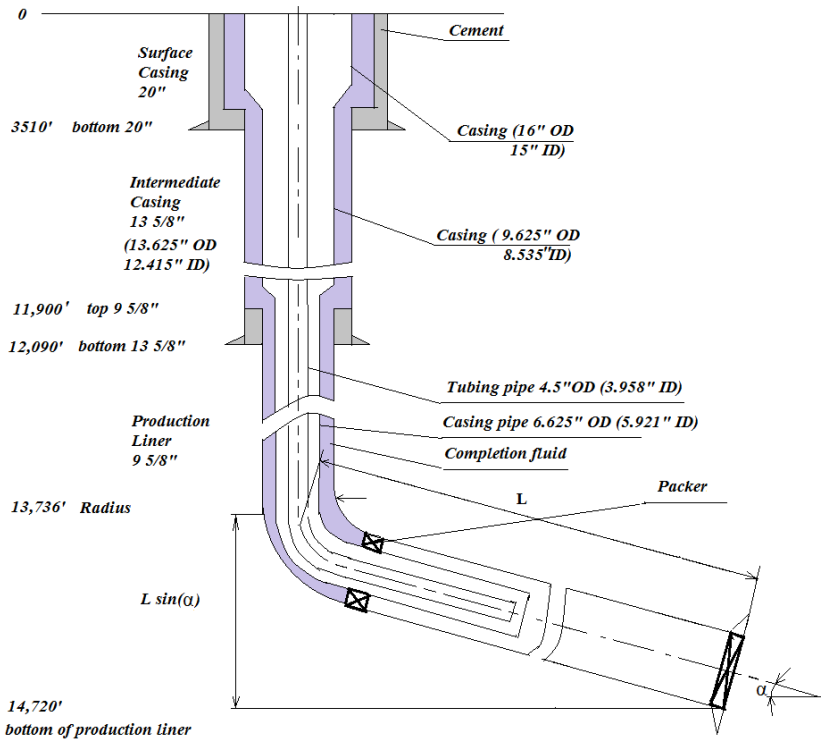

Figure 17: Casing program. The scheme was developed from the design of already drilled geothermal well in 1980 (Dobson) for the geothermal reservoir in Vermilion Parish, Louisiana.

A standard casing design was done to choose the casing plan and setting depths using the previously drilled Beulah Simon #2 (Dobson, 1978) well as a base. The calculations contain burst/collapse calculations for all segments of the casing program and matching the selection of the casings by maximum allowable stresses and safety margins, assuming design scenarios from Rahman and Chillingarian (1995). Details of the design are provided in Akmaudlin (2016).

The last casing is subject to bend to a maximum 90 degrees from vertical. Assuming uniform contact with the borehole the calculation results in Table 7 were performed according to Rahman and Chillingarian (1995). The total length of the last segment casing T-95 consists of 1225.2 ft of vertical section, 478.56 ft of bending section, and 914.4 ft of horizontal offset.

Table 7: Bending stress calculation results

Cross sectional area, inch^2	Axial stress w/o bending, psi	Additional stress to bending, psi	Total stress in a pipe, psi	Minimum acceptable yield stress, psi
22.0928	7,515.28	39,031.644	45,546.924	95,000

Table 8: Hook Load calculations

	Surface casing	Intermediate casing	Production casing
Hook Load, lbs	338,450.9	422,108.1	149,873

Completion Design

As was mentioned before there are three main sections in the horizontal section of the well: production, injection, and the section in between. To analyze the pressure development in the completion scheme, the wellbore was divided into nodes. As soon as the brine pump starts pulling geofluid from the production to the injection side, there are pressure drops that develop at each node. The maximum flow rate is in the closest nodes to the pump due to the lowest well flowing pressures, which confirms the maximum influx/outflow rates. Again, details for the calculations can be found in Akmaudlin (2016). Table 9 lists the specifications for the well design segments in the inclined/horizontal segment of the well.

Table 9: Horizontal well data 9 5/8 inch OD

Name	***Production side 100m (304.8 ft)***
Perforations	1 inch perforations with 20 shots per foot. Perforation length – 100m (304.8ft)
Gravel Pack	20/40 size sand with 135D permeability
Screen pipe	4.88 inch ID screen pipe
	Circular pipe interval 100m (304.8ft)
	8.031 inch ID
	Injection side 100m (304.8 ft)
	1 inch perforations with 12 shots per foot
	Extension pipe 5 inch OD (see Figure 20)

Production side

The brine flow rate value is bounded by two constraints. The desire to avoid possible sand production from the reservoir tends to decrease the flow rate value. From the other side, increasing flow rate means higher energy production from the hot aquafer. The chosen brine flow rate is 20.2 kg/s (11,020 bbl/day). The calculations assume no sand production which is based on previous drilling and production operations in the region (Durham, 1978).

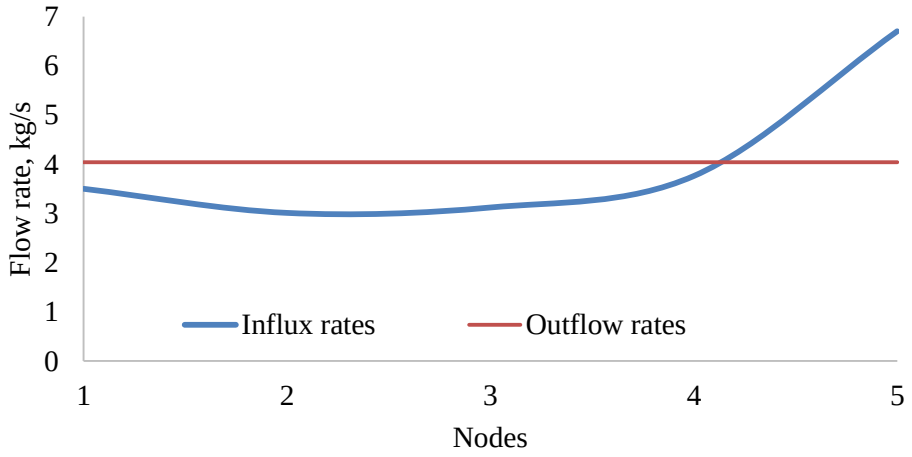

Figure 18: Influx distribution along the production and injection sides for total 20.2 kg/s brine flow rate. The nodes represent calculation intervals.

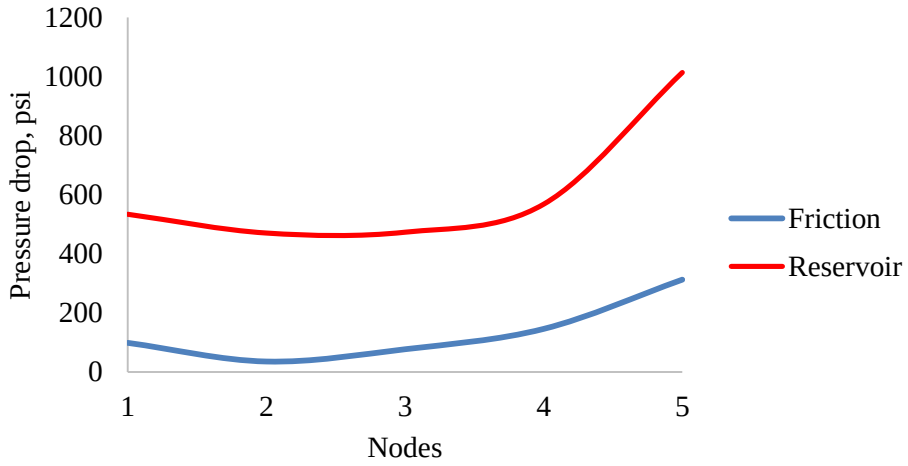

Figure 19: Pressure losses at 20.2 kg/s (11020 Bbl/day) brine flow rate. The maximum pressure drop in the fifth node is closest to the pump. 15 degree inclination

The maximum pressure drop is affected by frictional pressure losses and in the reservoir. Forchheimer, Acceleration and Gravel pack pressure drops are insignificant due to high area open to flow through the perforated interval. The maximum pressure drop occurs close to the pump location.

Injection side

The pressure development for the injection section develops in the opposite order than in production section. Pressure is maximum at the pump location and drops to the reservoir value while travelling through the completion. Since there is no heat exchanger, the frictional pressure drop is lower compared to the production side. The well flowing pressure values at each node are very close to each other and the out-flux flow rates are about the same (Figure 18). To simplify the design, no gravel pack is installed for this side of the well. Perforation size is 1 inch and 12 shots per foot.

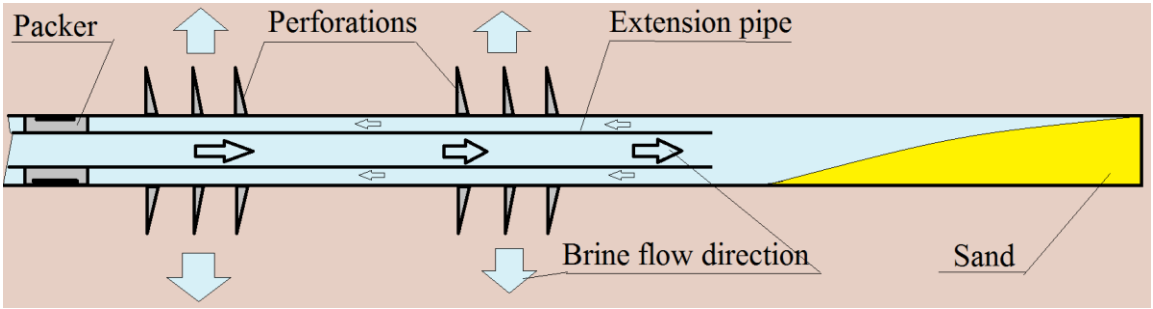

Figure 20: Injection side sand intrusion protection design scheme.

To protect the injection side from sand plugging the following scheme is proposed (Figure 20). Brine is pumped through the tubing all way to the end of the horizontal offset. Flow changes direction by 180 degrees and any sand particles missed by the production side gravel pack will be moving under inertial forces and can collect at the end of the well.

Coupling production and injection sides. Pump performance

The pressure drop in the circular pipe separating both sides and at the diameter change section is negligible compared with the completion pressure drop. The pump should overcome all pressure losses in the well and the reservoir in the production and injection sides at a certain flow rate. The sum of these pressure losses would define the pump head necessary at that flow rate. An inclination angle can reduce the pump power requirement due to gravity (see Figure 21).

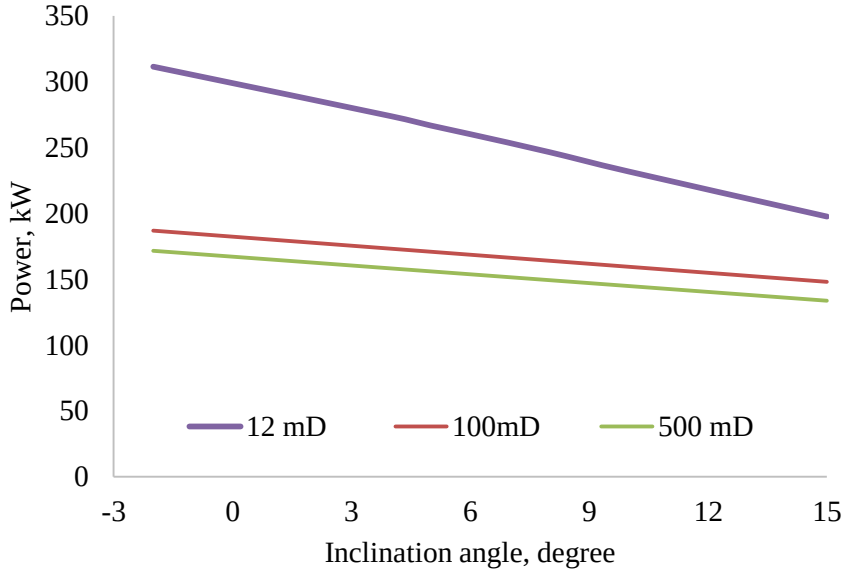

Figure 21: Pump power development with inclination of the horizontal well at different permeabilities of the reservoir. Higher values of permeability reduce the effect from inclination angle.

Choosing the correct ESP for the system is determined by pressure drop in the deviatd offset. Total pressure drop is a function of reservoir permeability and friction inside the well. Friction is a function of flow rate and for a fixed rate is assumed constant. Reservoir pressure drop is a function of permeability, which varies from 10 to 500 mD depending on location (Ansari, 2015). Figure 21 shows the pump power requirement from the permeability change found by the following formula:

$$P = \frac{\Delta P \, \dot{m}_{brine}}{\rho_{brine}}$$

This is how much power would be needed for brine circulation. The pump power requirement should be corrected by pump efficiency. Obviously, less power is required for high permeability cases. With 100 mD the value is 148 kW at 15 degree inclination. Figure 16 shows one of the suitable cases for the brine pump from the Schlumberger REDA® pump catalog. With 11,000 Bbl/day flow rate and converting pressure difference to feet of head, the pump would require 47 stages and 152.75 kW power consumption.

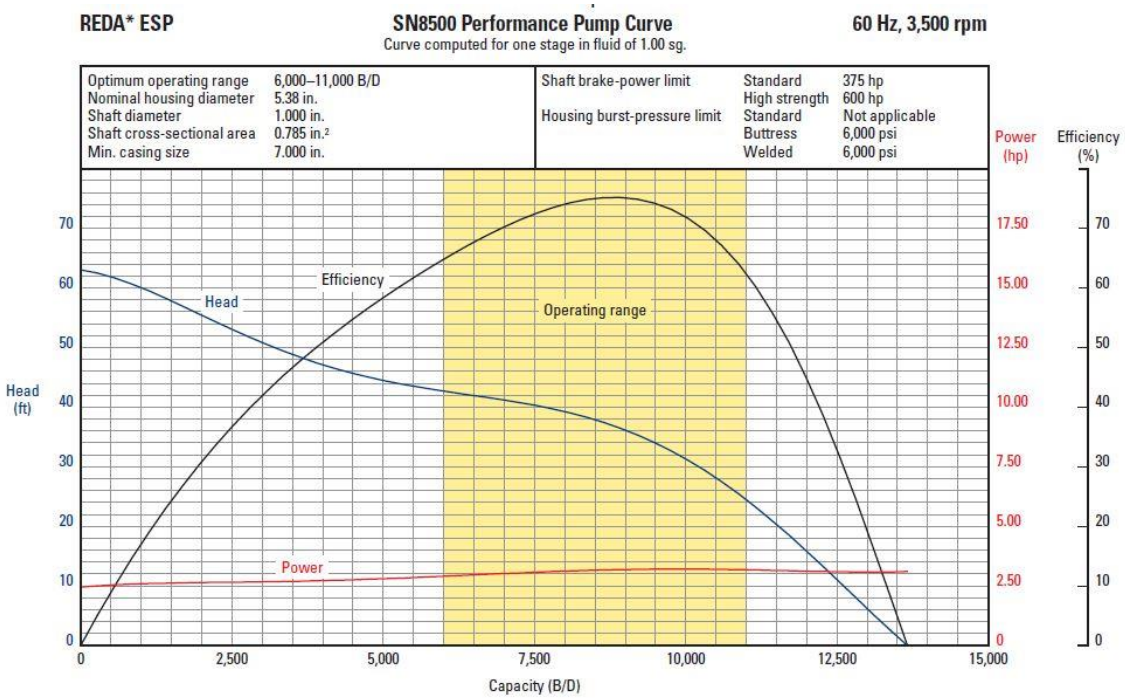

Figure 22: Example of pump performance curve for one stage. The calculated required number of stages is 47.

Arrangement

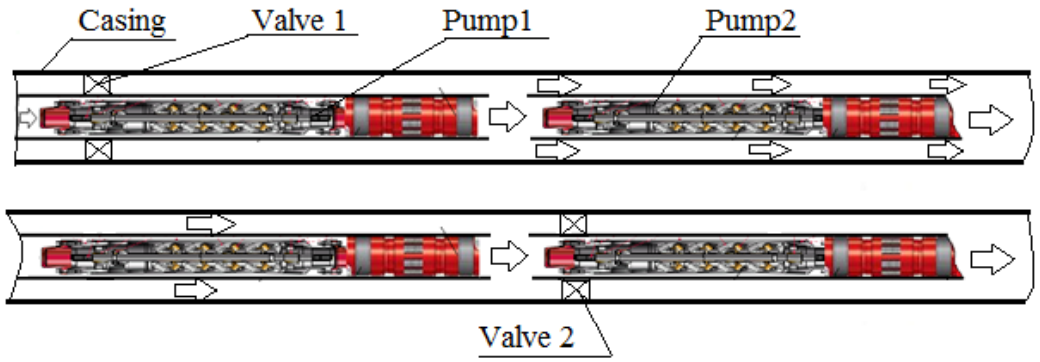

Figure 23: Pump assembly arrangement. When the pump 2 is disabled, the bypass valve 1 is closed in the upper picture. Flow is pressurized by pump 1. When the pump 2 is operated the valve 2 is closed and pump 1 is not working (bottom figure).

To be able to minimize workover issues, a second pump is added inside the 9 5/8" casing (Figure 23). Electrically driven bypass valves 1 and 2 provide opening and closing the paths for the fluid to flow.

Power Generation Loop

Downhole Heat Exchangers.

Brine passes through the perforations into Annulus 2 shown in Figure 24. Annuli 1 and 2 represent the heat interaction boundaries of two independent loops: brine and working fluid. Heat is transferred to the cold secondary working liquid through the annulus 1 pipe thickness.

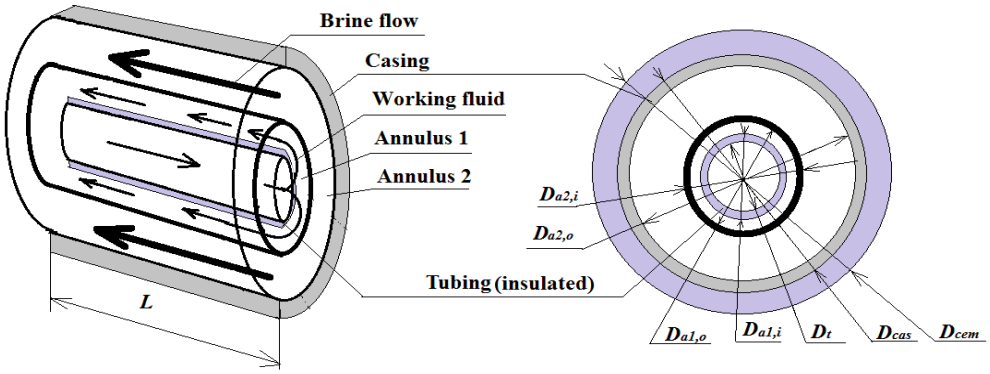

Figure 24: DHE cross sectional cut view. The direction of working fluid and brine flow is shown in parallel scheme as an illustration.

Table 10 Geometric data of chosen casings and tubing in DHE

DHE size, m		
Casing 1	Diameter inner	0.1536
	Diameter outer	0.1936
Casing 2	Diameter inner	0.2190
	Diameter outer	0.2445
Cement sheath	Diameter outer	0.3105
Tubing	Diameter inner Diameter outer	0.1143 0.1000

The heat transfer process was analyzed referring to Feng (2012) under the following assumptions: steady-state, perfectly insulated tubing with constant fluid properties and fully developed flow conditions for both the brine and working fluids. The horizontal offset was divided into several intervals and the fluid properties were calculated from NIST. The equations used can be found in Akhmadullin (2016).

Direction of brine and working fluid flow

The working fluid temperature increases to a higher value with counter flow compared to parallel flow (Feng, 2012). Thus, for the analysis shown here, only counter flow was evaluated.

Thermodynamic Analysis and Working Fluid Choice

Several researchers tested capabilities of carbon dioxide as a working fluid in supercritical cycle. Chen et al. (2011) compared CO_2 with R123 in a supercritical power cycle and found that carbon dioxide has higher system efficiency when accounting for heat transfer ability. There is no or very small pinch point limit in the heat exchanger. Zhang et al. () suggested using CO_2 as a working fluid for supercritical cycle due to higher cycle efficiency and coefficient of performance (COP). Other researchers mentioned satisfying features such as moderate critical point, stability at high pressure/temperature conditions, safety, and low cost. Operating conditions between 6-16MPa have safety issues in traditional power plants. In the ZMW case, it is an advantage to implement in deep wells where high hydrostatic pressure keeps CO_2 in a supercritical condition. Another benefit is that carbon dioxide has higher density compared with hydrocarbons often discussed as potential working fluids, thus, requiring less pump work. A drawback might be a low critical point of 31.1 °C which can be a problem while using it in hot

climate regions. Carbon dioxide has to be cooled below this critical temperature to be able to condense. However, using a non-condensing cycle is a solution.

Thermodynamic analysis was performed by dividing the Heat Generation Loop into the intervals with the nodes, where fluid properties were defined using the NIST fluid properties solver. Table 11 illustrates the fluid property changes while travelling up and down in the Heat Generation Loop. From node 1 to 2 is flow downward vertically inside the 5" casing to the DHE. From node 2 to 3 is pump work and nodes 3 to 4 is flow downward through the deviated section and inside the insulated 2" production tubing toward the end of DHE. Nodes 4 to 5 is the enthalpy increase in the DHE. Nodes 5 to 6; 6 to 7; 7 to 8; and 8 to 9 are flow upward inside the various annuli. From node 9 to 10 is the turbine pressure expansion line; and from node 10 back to node 1 is the cooling process in the condenser.

Table 11: Thermodynamic properties of working fluid travelling in the PGL. The blue and orange colors represent cold and hot sides of the subsystem.

Node	P, MPa	ρ, kg/m^3	T, C	h, kJ/kg	S, kJ/kgK	Cp, kJ/kgK	k, W/K	μ*10^(-5) Pa*s
1	7.50	661.10	30	291.65	1.299	8.13	0.078	5.6
	14.54	840.00	30	260.5	1.170	2.45	0.094	7.8
	22.36	907.05	30	253.5	1.113	2.07	0.1075	9.4
	30.8	952.02	30	250.56	1.074	1.91	0.1100	10.5
	39.69	988.11	30	249.94	1.043	1.81	0.12	11.7
2	48.87	1016.20	30	250.65	1.016	1.76	0.134	12.7
3	53.87	1017.05	35	260.17	1.0402	1.73	0.135	12.735
	55.01	1020.10	35	260.33	1.0266	1.72	0.1354	12.8
	55.00	1019.9	35	260.33	1.027	1.72	0.1354	12.55
4	54.99	895.39	80.27	338.72	1.268	1.715	0.109	9.08
	54.99	840.46	101	373.75	1.36	1.703	0.0999	8
	54.98	813.06	111.2	391.59	1.4051	1.69	0.0965	7.546
	54.98	800.08	116.5	400.04	1.43	1.69	0.094	7.344
5	54.96	792.48	120.3	405	1.4407	1.681	0.0929	7.238
6	53.34	783.04	120.3	405	1.4409	1.697	0.0915	7.09
7	51.12	782.00	120.3	407.77	1.449	1.72	0.087	7.08
	49.25	760.20	120.3	409.55	1.46	1.72	0.087	7
	47.22	747.15	120.3	411	1.49	1.747	0.085	6.5
	45.21	734.09	120.3	415	1.526	1.75	0.083	6.3
	43.18	719.83	120.3	420	1.548	1.78	0.081	6.185
8	39.22	687.23	120.3	427	1.586	1.82	0.083	7.7
	35.59	653.51	120.3	438.3	1.62	1.9	0.0734	6.389
	32.06	613.30	120.3	444.78	1.65	1.94	0.0689	4.9
	28.74	568.26	120.3	449.25	1.671	1.98	0.063	4.54
	25.67	519.12	120.3	453.94	1.6867	2.027	0.0562	3.968
	24.55	498.76	120.3	458.55	1.709	2.038	0.0547	3.7
	22.34	454.03	120.3	461.83	1.72	2.03	0.051	3.5
9	21.27	432.10	120.3	467.64	1.74	2.024	0.051	3.46
10	8.0	301.69	49.5	435.7	1.7585	4.33	0.043	2.38

Graphically the thermodynamic properties change is illustrated in the Figure 25, Figure 26, and Figure 27. The red and blue lines represent liquid and gas sides of the saturation curve.

Node 1 represents the liquid CO_2 stage leaving the condenser. Fluid is directed into the vertical well and travels downward inside the 5 inch OD insulated tubing. Pressure increases gradually from 7.5 to 48.87 MPa with constant temperature 30 °C. Fluid density grows from 661 to 1012 kg/m^3. Entropy and enthalpy are reduced, except interval 2-3. This jump in pressure and temperature represents pump work. The location of the pump is 4770 m right before the deviated section. This position was chosen due to pump safety concerns. Additionally, the highest density location is preferable to reduce pump energy consumption.

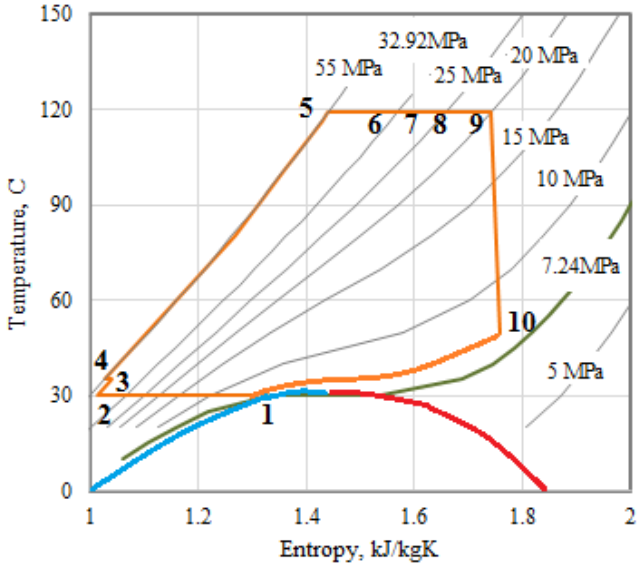

Figure 25: T-S diagram. Intervals 5-9, 1-2, and 3-4 are insulated, therefore, illustrated as a straight lines of constant temperature.

The interval between points 3 and 4 is the insulated pipe flow through the curvature inside of the DHE. Point 4 is at the end of the heat exchanger. After this the flow turns back upward toward the surface. The line from point 4 to 5 represents the temperature rise inside of the DHE. Pressure is slowly reduced by friction, and temperature increases to 120.3 °C. The temperature rise affects density which drops by 100kg/m^3, and entropy and enthalpy get larger. The points 6, 7, 8 and 9 represent flow inside of the vertical insulated annuli according to the casing design up to the turbine. Pressure is reduced to 21.2MPa, but temperature is assumed constant at 120.3 °C. The enthalpy for this sequence is the maximum of the cycle and is equal to 467 kJ/kg. The turbine reduces the pressure to 8 MPa.

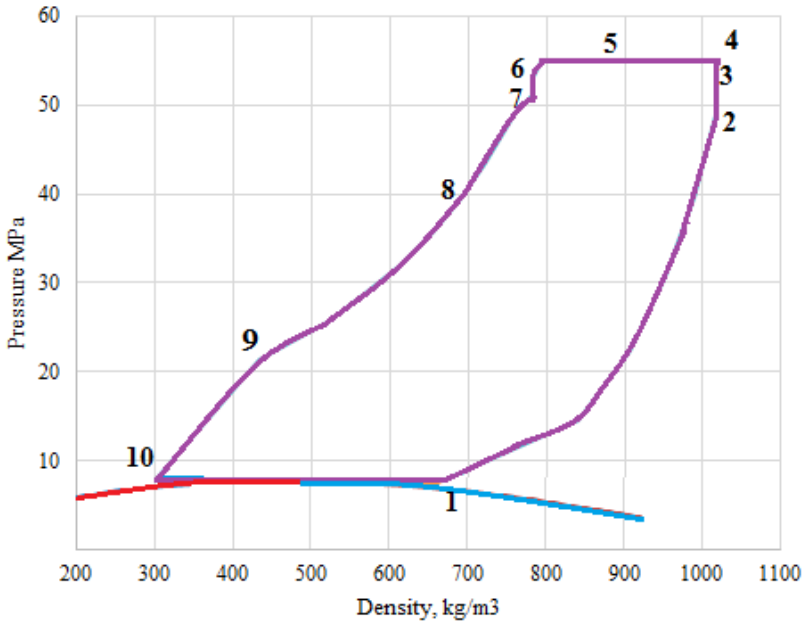

Figure 26: Pressure-density diagram.

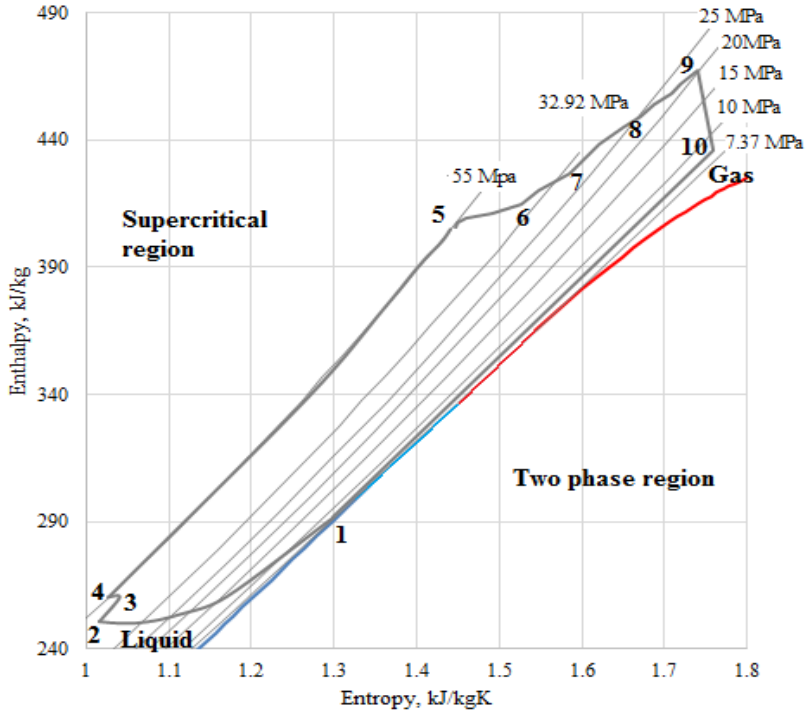

Figure 27: Enthalpy-entropy diagram. The well locations are shown by the numbers.

Insulation

One of the important aspects of the system is insulation. The cold and hot side tubings should be insulated in order to achieve the desired power production. Insulation should be compact in size, very effective, and thermally and chemically resistant to reaction with carbon dioxide. One possibility is Hyperlast Offshore Technology produced by The Dow Chemical Company. The insulation material has low thermal conductivity of 0.15 W/m-K and has been used in the offshore petroleum industry for over 30 years.

Working Fluid Pump

The working fluid is flowing up and down through the well, experiencing phase change. The geometry of the flowing path was defined by casing design and chosen tubings sizes. The working fluid pump is used to overcome all pressure losses in the system. The location of the pump was chosen right before the radius of curvature, where the density of CO_2 is close to the maximum value of 1016.2 kg/m^3. The power requirement for this pump is 49.21 kW.

Additionally, the density affects pressure entering the turbine. To keep the pressure at 21.27 MPa the pump hydraulic head requirement is 5 MPa, which gives 70.3 kW power with 70% pump efficiency. The proposed model is a Schlumberger ESP D5800N with 67 stages.

Design of Small Diameter Multi Stage Turbine

An axial turbine was chosen to extract work from the fluid. An axial configuration is very well suited for the vertical portion of the well, because the direction of the flow matches the turbine-generator axis. To prevent workover operations in case there is a turbine failure, the design includes several turbines. This allows non-stop energy production and the possibility of increasing the working fluid flow rate (thus generating more power) without concerns of vibrational limits in the turbine stage. The flow rate can be evenly distributed among the stages using sliding sleeve mechanism or simple bypass tubes. In addition, the turbines could be worked in parallel in effect doubling or tripling the power generated.

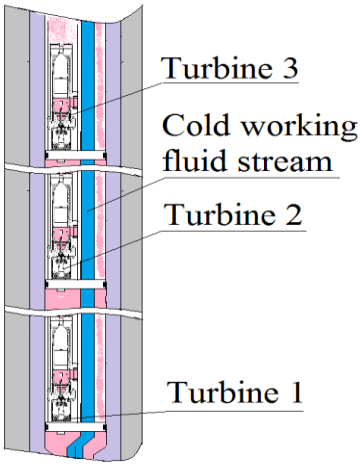

Figure 28: Triple stage axial turbine assembly

The design scheme for the turbine choice is a simple multistage axial turbine. The turbine was analyzed using Church correlations with the following assumptions: the blades of the turbine have frictionless surfaces, and energy conversion on the blade is complete; the fluid flow path matches with blades or nozzle geometry and there is no flow separation from the blades surface; the flow is uniform and steady and has the same properties at every blade of the stage. The equations and procedures is shown in Akhmadullin (2016).

Table 12: Results of single stage turbine calculations

Fluid	Turbine blade radius, inch	Turbine efficiency	Shaft Rev/min	Number of stages	Pressure Start, MPa	Pressure Final, MPa	Mass flow rate kg/sec
CO_2	2.5	0.814	19.018	1	21.27	8	10

Figure 25 illustrates the single stage turbine expansion process with 81.4 % efficiency. With 10 kg/s flow rate the turbine work is 319.4 kW. To convert this work into electric power the generator efficiency of 0.96 and gearbox efficiency of 0.97 were assumed. The resulting electric power produced from the system is 297.4 kW.

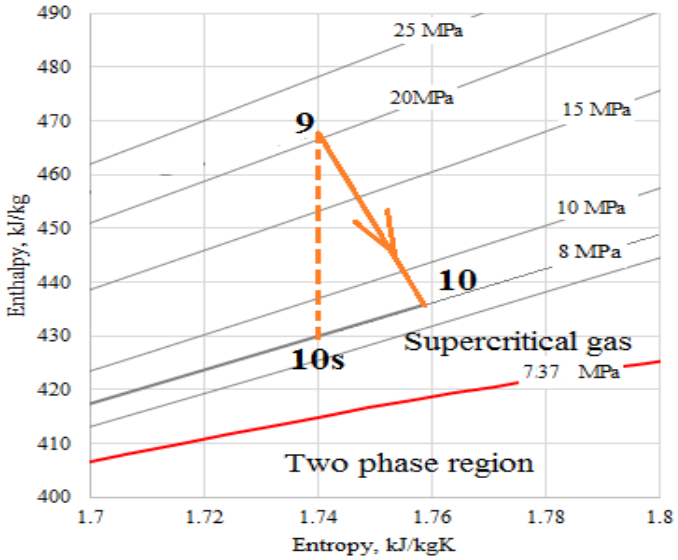

Figure 29: Turbine expansion Enthalpy-Entropy chart. The red line represents the two-phase boundary region. The dashed line is a constant entropy expansion (ideal), and arrow shows real turbine expansion with 0.81 efficiency).

Heat Rejection Loop – Condenser

An air driven condenser was chosen for cooling the system. The total heat to be rejected to the ambient was found as carbon dioxide mass flow rate multiplied by enthalpy difference of the fluid entry and exit conditions:

$$Q = \dot{m}_{CO2}(h_{10} - h_1)$$

Taking values from Table 11 the heat rejection value is 1.44 MW. To successfully emit this amount of heat by traditional air conditioner system is quite challenging task due to limitation of climate conditions (see Figure 30). The critical point of carbon dioxide is about 31 °C. CO_2 vapor to liquid conversion at this point is associated with rapid fluid properties changes, which is not a stable stage. From the observations of the commercially available coolers the Baltimore Aircoil Company's Trillium Series CO_2 condenser is an attractive product.

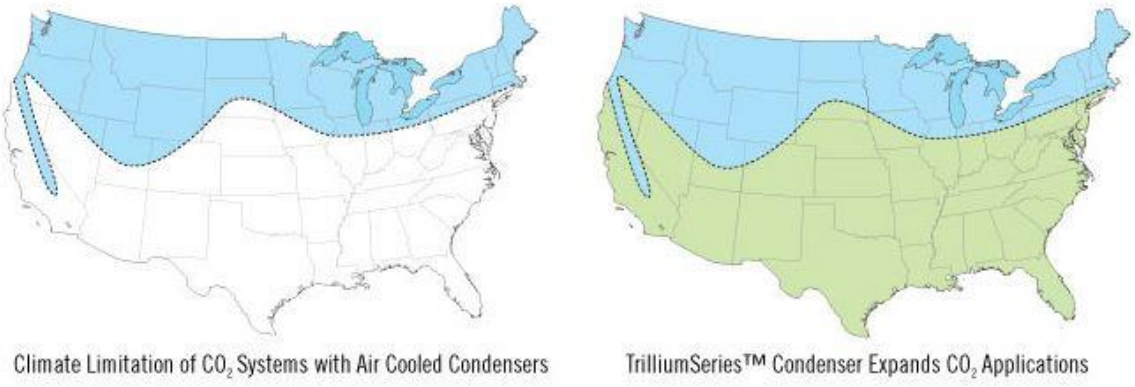

Figure 30: Climate change limitations for the air cooling systems. (Borrowed from http://www.baltimoreaircoil.com)

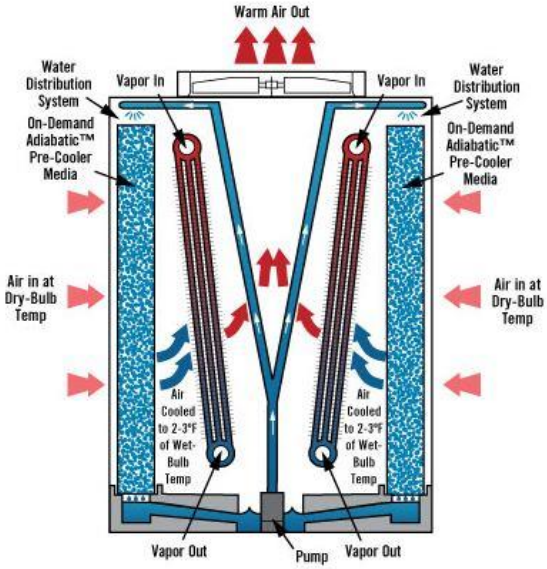

Figure 31: Condenser operating principle.

Conclusions

Table 13 provides the design specifications for a reference system design using "off-the-shelf" products with the possible exception of the downhole turbine.

- A supercritical CO_2 OR cycle with a single stage axial turbine will produce 297.4 kW of electric energy from the single unit with a 10 kg/s working fluid flow rate. Higher power production is possible using a parallel system with minor added cost.

- The condenser was chosen from the commercially available units from the Baltimore Aircoal Company. The company specializes in cooling supercritical CO_2 systems. However, the ambient air fluctuations affect the produced energy. Future work is dedicated to find a technology to avoid climate temperature changes and make the system more stable.
- The length of the DHE and horizontal offset defines the rate of reservoir cooling, and thus, produced power reduction. Future work would be to find an analytical correlation allowing the determination of the distance between production and injection completions that avoids production stream cooling.
- The highest power drain for the system is the brine pump. The amount depends on reservoir permeability and a flow rate. Increasing geofluid flow rate with lower power requirements is possible for high permeability reservoir locations with less power spending on pump. Low permeability systems may also be able to achieve high rates by increasing the completion lengths.

Table 13 Summary table for System Design

Working fluid	CO_2	
DHE	Coaxial type, counter flow	
	Length	100m (304.8 ft)
Brine pump	Flow rate	20 kg/s (11021 Bbl/day)
	Model	REDA ESP SN8500
Turbine	Single stage axial turbine	
	blades radius	2.5 inch
	Shaft revolutions	19,000 rpm
	Electric power produced	297.4 kW
Working fluid pump	Flow rate	10 kg/s (5510 Bbl/day)
	Model	Schlumberger ESP D5800N 67 stages
Condenser	Baltimore Aircoil Company	Trillium series condenser

References

Akhmadullin I., *Design And Analysis Of Geothermal Wellbore Energy Conversion System Working On Zero Mass Withdrawal Principle*, PhD Dissertation, LSU, (2016)

Chen Qun, Wu Jing, Wang Moran, Pan Ning, Guo Zheng Yan, "A Comparison of Optimization Theories for Energy Conservation in Heat Exchanger Groups", *Chinese Science Bulletin*, February 2011, Vol.56, 449-454

DiPippo R., "Second Law assessment of binary plants generating power from low-temperature geothermal fluids", *Geothermics* 33, (2004)

Dobson, R. J., Hartsock, J. H., McCoy, R. L., and Rodgers, J. A., (1980), "Investigation and Evaluation of Geopressured-Geothermal Wells - Final Report, Beulah Simon No. 2 Well, Vermilion Parish, Louisiana, Volume I: Completion and Testing", Gruy Federal, Inc., Houston, Texas.

Durham Jr, C. O. (1978). "Analysis of Cameron Parish geopressured aquifer. Final report (No. NVO-1561-1)". Magma Gulf Co., Baton Rouge, LA (USA).

Feng Y., *Numerical Study of Downhole Heat Exchanger Concept in Geothermal Energy Extraction From saturated and Fractured Reservoirs*, PhD Dissertation, LSU, (2012)

Feng, Y., Tyagi, M., and White, C.D.: "A Novel Downhole Heat Exchanger Concept for Saturated Low-Enthalpy Geothermal Resources" *Geothermics*, v.53, p. 368 – 378, January 2015.

Gray T.A., *Geothermal Resource Assessment of the Gueydan Salt Dome and the Adjacent South-East Gueydan Field, Vermilion Parish, Louisiana*, Master Thesis, LSU, (2010)

Rahman S.S., Chillingarian G.V., *Casing Design. Theory and Practice*, Elsevier Science B.V., 1995, ISBN: 0-444-81743-3

APPENDIX: System Installation Procedure

The system installation procedure is introduced in Table 14. The installation process is described starting from the perforation operation after the casing design is already run and cemented. After the perforation work, the system is run into the well as a whole assembly (starting from brine pumps and finishing with tubing holder) at one trip. The main parts of the system such as w.f. packer and pump, cold stream tubings, turbine assembly with the packer will be running together inside the production casing. As soon as the brine pump assembly reaches TD and tubing is set in the wellhead, an electrical signal initiates the packer latching mechanisms simultaneously. The next step is electric wiring work according to the scheme; checking the circulations of the brine and *w.f.* loops; connection the w.f. condenser with the wellhead through the safety valves; substitution of the completion fluid by the liquid CO_2, and running the system with necessary adjustments to receive the maximum net power production.

Table 14 System installation procedure

Step	Operation	Notes
1	Run perforation gun into the well to the 18,352.23 ft MD.	Injector perforation
2	Perforate 16m (52.5ft) length injector side	
3	Remove perforation gun	
4	Run perforation gun into the well to the 14,907.35 ft MD.	Producer perforation
5	Perforate 200m length producer interval	
6	Remove perforation gun	
7	Pumping test to ensure that both perforation intervals (producer and injector) provide the required flow rate. If required, increase perforation length	
8	Run two brine pump assemblies 5.5 OD with packers 7.0 OD at 15,000 ft MD	Running the system into the well occur at one trip. The system run starts from two brine pump assemblies with packers, DHE with ICD and prepacked screens, tubings, and *w.f.* pump. The final equipment is turbine assembly with packer.
9	Run 100 ft 5.5 inch perforated pipe as a separation interval from the DHE. The brine will enter the pipe through the perforated holes and later the ESP. Clips the cable to the hanging tubing.	
10	Run ICD into the 14,907.35 ft MD with DHE inside of the prepacked sand screens 250m (820.21 ft)	
11	Run the DHE packer and the outer production tubing assembly. Setting depth is 1409.35 ft MD right after the bending section.	
12	Run 5inch OD 515.35 ft length insulated tubing, connected to the DHE packer by additional packer 7 inch OD.	
13	Run *w.f.* pump assembly, connected to the insulated tubing.	
14	Run 5 inch OD tubing above the *w.f.* ESP.	
15	Run Turbine dual string packer with turbine-generator assembly on top. Setting depth is 20 ft below the surface.	
16	Run 5 inch cold stream tubing to the well head.	
17	Connect the cold stream tubing to the well head by tubing holder	
18	Connect power cable to the electric switch board.	
19	Latch all packers at ones using the power cable installed with the system in previous steps.	

20	Circulate the *w.f.* zone by the w.f. pump. Check for the integrity of the system.	
		Starting the system
21	Drive the brine by brine pump and check the temperature change at the DHE and flow rate.	
22	Connect the condenser to the wellhead.	
23	Substitute completion fluid in the *w.f.* zone (vertical well and horizontal DHE section) by carbon dioxide fluid.	
24	Start the system. Maintain the brine and *w.f.* flow rates as prescribed for this particular application, check the temperature of the *w.f.* at the DHE and condenser.	

Total measured depth is 18,404.73 ft (From the top to the end of injector perforations).

Task 4 – Wellbore Integrity

Task 4 – Wellbore Integrity: Impact Of Geofluids On Wellbore Infrastructure In Geothermal Energy Exploration; Focus On Wellbore Cement

Subtask 4.1 – Laboratory setup

1. Porosimeter

The grain volume porosimeter was delivered to the Sustainable Energy and Environmental Research (SEER) laboratory last quarter of 2012 as shown in Figure 32. The porosimeter was used to measure the porosity of wellbore cements during entire project and is continually used in other experiments. These measurements were also used as input data for permeability measurements. The porosimeter is designed for standard 1 inch and 1.5 inch core diameters, which will enable us to compare our measurements with other laboratories.

Figure 32: Porosimeter Ultragrain Grain Volume, UGV-200®

Porosimeter was calibrated using calibration cores provided by the CoreLab. In addition cement cores that were available from a different project were tested as well as sandstone cores and the data was acceptable. Samples cured at elevated T, and at ambient conditions were tested and results were included in the 2013 annual report for the project.

2. Oven and Temperature Cycling/Relative Humidity Chamber

The SEER laboratory also received a vertical temperature chamber (oven) and a temperature cycling/relative humidity chamber (environmental chamber) for testing wellbore cement under geothermal conditions. The vertical temperature chamber has a capacity of 216 liters and can be programed to run between 20 °C – 300 °C. The thermal cyclic/relative humidity chamber on the hand can be programmed to do multiple cycles in same run and have a much lower temperature at -40 °C.

In the first quarter of 2013, an ESPEC engineer visited the LSU to train the students on using both chambers. During the training with ESPEC engineers, it was identified that the environmental chamber would require a pure (deionized) water supply for effective functioning. A contractor was identified and during several weeks the water supply had to be adjusted, and a water treatment system installed, tested and calibrated. The water treatment system requires quarterly inspection and a contract was signed for this for the duration of the project as well. The SEER lab was fitted in March with a reverse osmosis water treatment system

Figure 33: Water treatment system provides de-ionized water for key equipment (chamber, permeameter)

that provides de-ionized water to the temperature cycling/relative humidity chamber (Figure 33). It is essential to have continuous pure water supply in order to have accurate humidity in the chamber.

Also during this time period, the oven and environmental chamber were installed and calibrated (initially and once a year thereafter). The environmental chamber required a specialist calibration, so that accurate measurements of RH, which are critical for cement curing, could be established. This was completed in 6 weeks. In order to be able to do HP/HT experiments we were required to install a hot air vent, which will discharge hot air out of the lab. This activity required additional time and resources.

3. Liquid Pressure Pulse-Decay Permeameter

Designing, assembling and testing of the liquid pressure-pulse decay permeameter, was completed by Core Laboratory (CoreLab) at their laboratories in Tulsa, Oklahoma at the end of March, 2013. Students working on the DOE Geothermal project visited CoreLab in Tulsa in April for a free training and demonstration on using the permeameter. They also had the opportunity to observe the difference between the gas permeability measurements (routinely done by CoreLab) at no extra cost. Furthermore, all the packing of the equipment was done at that time so that it would be easier for LSU to assemble equipment once received.

The permeameter was for measuring permeability and indirectly used to provide data relevant to integrity of cement sheath zonal isolation function under geothermal conditions. Measuring of cement permeability to brine is of critical importance for long term prediction of geopressured geothermal cement behavior. The permeameter also has a core flooding system that will be used for flow through experiment, which is required for quantification of cement deterioration in contact with geofluids.

The core holder of the instrument can be placed in a thermal chamber up to 150 ^{0}C, with maximum overburden pressure of 10,000psi and maximum back pressure of 6,000psi to simulate reservoir condition. The pressure-pulse decay permeameter was delivered to LSU in late April, 2013. It was assembled in the SEER laboratory as it had been shipped over from Tulsa, Oklahoma. As shown in Figure 4, the lab is now fully equipped as proposed. The core holder unit has enough pipe length so it can be fitted inside the oven for high temperature experiments. We have capability to do permeability measurement at high T, P and be able to measure pH of the fluid at those conditions.

Calibration: During summer 2013 most of the time was spent on testing and calibrating permeameter. At first, the pressure decay was not initiating. Since we did not purchase the CoreLab technical support, most of the difficulties were resolved via Skype conference calls. It was identified that most likely during shipping the diaphragm in the Validyne dP transducer was damaged and it had to be replaced. The equipment set up and calibration was successfully accomplished by graduate students with the assistance from technical staff from CoreLab Ltd at no charge.

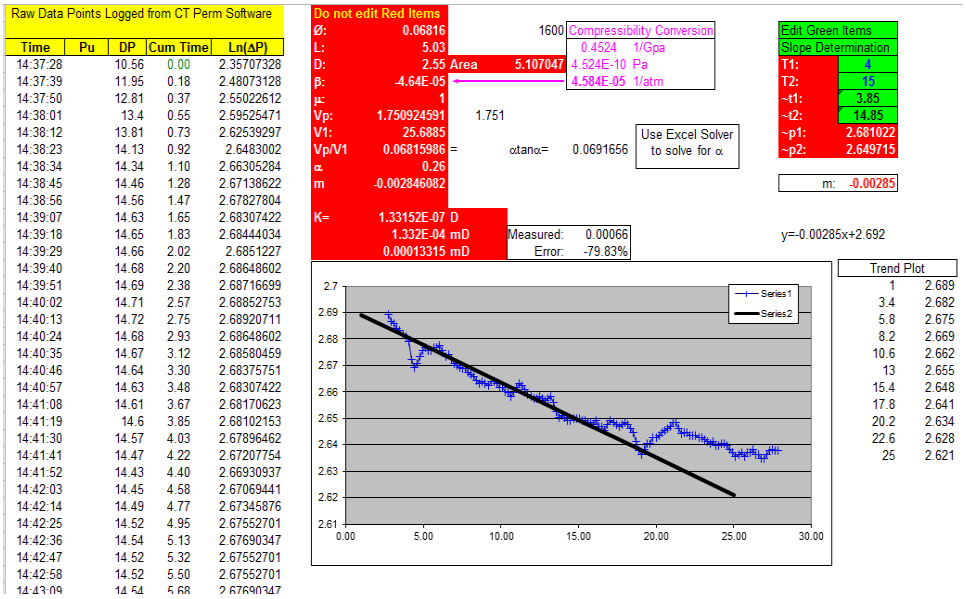

Raw Data Points Logged from CT Perm Software

Time	Pu	DP	Cum Time	Ln(ΔP)
14:37:28	10.56	0.00		2.35707328
14:37:39	11.95	0.18		2.48073128
14:37:50	12.81	0.37		2.55022612
14:38:01	13.4	0.55		2.59525471
14:38:12	13.81	0.73		2.62539297
14:38:23	14.13	0.92		2.6483002
14:38:34	14.34	1.10		2.66305284
14:38:45	14.46	1.28		2.67138622
14:38:56	14.56	1.47		2.67827804
14:39:07	14.63	1.65		2.68307422
14:39:18	14.65	1.83		2.68444034
14:39:29	14.66	2.02		2.6851227
14:39:40	14.68	2.20		2.68648602
14:39:51	14.69	2.38		2.68716699
14:40:02	14.71	2.57		2.68852753
14:40:13	14.72	2.75		2.68920711
14:40:24	14.68	2.93		2.68648602
14:40:35	14.67	3.12		2.68580459
14:40:46	14.64	3.30		2.68375751
14:40:57	14.63	3.48		2.68307422
14:41:08	14.61	3.67		2.68170623
14:41:19	14.6	3.85		2.68102153
14:41:30	14.57	4.03		2.67896462
14:41:41	14.47	4.22		2.67207754
14:41:52	14.43	4.40		2.66930937
14:42:03	14.45	4.58		2.67069441
14:42:14	14.49	4.77		2.67345876
14:42:25	14.52	4.95		2.67552701
14:42:36	14.54	5.13		2.67690347
14:42:47	14.52	5.32		2.67552701
14:42:58	14.52	5.50		2.67552701
14:43:09	14.54	5.68		2.67690347

Do not edit Red Items

Ø:	0.06816		
L:	5.03		
D:	2.55	Area	5.107047
β:	-4.64E-05		
μ:	1		
Vp:	1.750924591		
V1:	25.6885		
Vp/V1	0.06815986	=	
α	0.26		
m	-0.002846082		
K=	1.33152E-07	D	
	1.332E-04	mD	
	0.00013315	mD	

1600 Compressibility Conversion
0.4524 1/Gpa
4.524E-10 Pa
4.584E-05 1/atm

1.751

αtanα= 0.0691656

Use Excel Solver to solve for α

Measured: 0.00066
Error: -79.83%

Edit Green Items
Slope Determination

T1:	4
T2:	15
~t1:	3.85
~t2:	14.85
~p1:	2.681022
~p2:	2.649715

m: -0.00285

y=-0.00285x+2.692

Trend Plot

1	2.689
3.4	2.682
5.8	2.675
8.2	2.669
10.6	2.662
13	2.655
15.4	2.648
17.8	2.641
20.2	2.634
22.6	2.628
25	2.621

Figure 34: Screenshot of the Semi-log analysis of differential pressure in calculating permeability of class H cement cured at 90^{0}C and 100% RH for 30 days.

Figure 35: From Left to right, Liquid Pressure-Pulse Decay Permeameter, Vertical Temperature Chamber, and Temperature Cycling/Relative Humidity Chamber respectively.

***Both Chambers and the Porosimeter were fully functioning at the end of March 2013. The reason we were late on the projected date for these activities is that there was a delay from the LSU purchasing office in obtaining tender and selecting contractors. Other delays were caused due to the inadequate electricity supply as well as lab space modifications that had to be done prior to any calibration of the equipment.

Quality Control: Cement and Rock samples were sent to Weatherford Laboratories, Houston to validate measurements from installed instruments, good agreement in data was achieved. In addition, several graduate students run petrophysical measurements on cement/rock samples and reproducibility in data was achieved.

Subtask 4.2 – Cement design and Experimental methodology

Table 15: Experimental cement designs tested in this study. The selected admixtures were used based on their potential reduction of thermal shrinkage (fibers) and loss of Ca through change of Ca to Si ratio in CSH to prevent cement dissolution in contact with low pH geofluids.

Design	Neat Cement	Steel Fiber Cement	Silica Sand Cement	Calcined Clay Cement	Glass Fiber Cement
Class H Cement	1	1	1	1	1
Bentonite	0.02	0.02	0.02	0.02	0.02
Silica Flour	--	0.35	0.35	0.35	0.35
Steel Fiber	-	0.02	-	-	-
Silica Sand	-	-	0.02	-	-
Calcined Clay	-	-	-	0.02	-
Glass Fiber	-	-	-	-	0.02
Water	0.87	1.17	1.17	1.17	1.17

***Details of experimental methods, protocols, materials and conditions can be found online in K. Bello thesis document: http://etd.lsu.edu/docs/available/etd-09022014-111540/

Testing of experimental protocol and suitability of equipment:
Neat Cement core samples were prepared and cured in the chamber at 90 ^{0}C and 100% relative humidity to simulate reservoir conditions. Cement samples were also prepared and cured in water bath at ambient conditions. These two sets of samples were used as control sample data. SEM images showed increased porosity when compared to samples cured at ambient conditions (Figure 36). These observations have been reported extensively in the literature, and the purpose of repeating some of the basic research on known cement designs is to establish that our equipment was functioning and that all of our experimental protocols were tested.

Lower micrograph is a Back Scattered Electron Image of a polished thin section of a High T cured sample, clearly showing more detail in compositional difference of individual grains, due to presence of elements of different atomic mass. The spectra on the right from the same imaged area of the sample, reveal chemical variation that is more enhanced when compared to ambient condition cement. This suggest that future studies need to focus more on polished samples as they have higher level of accuracy and produce more quantitative data,

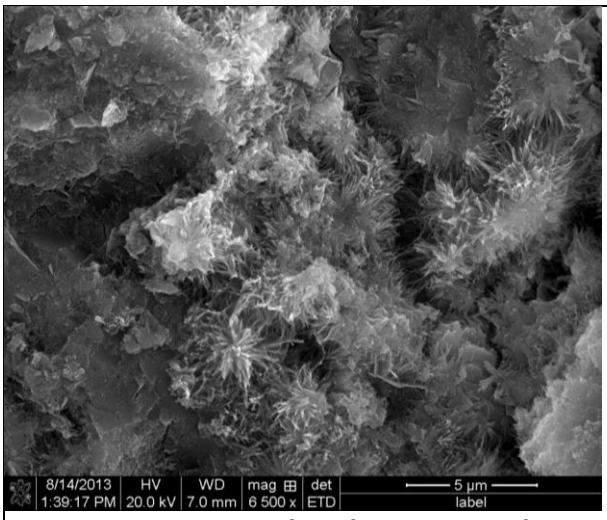

SEM micrograph of a fractured surface of hydrated class H neat cement slurry, cured 22C for 30 days in 100% RH (control sample)

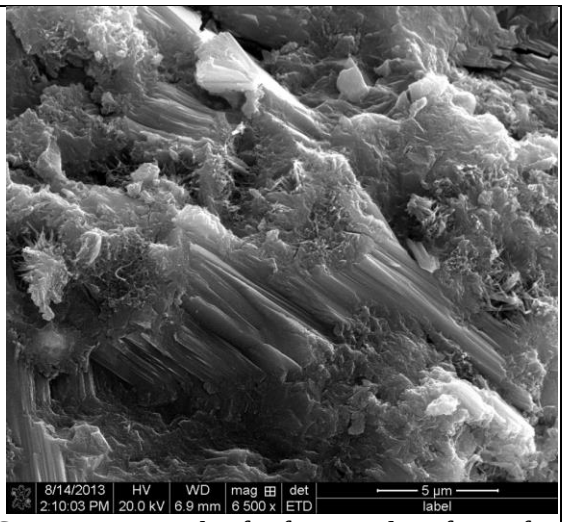

SEM micrograph of a fractured surface of hydrated class H neat cement cured at 90ºC in 100% RH for 30 days inside ESPEC Environmental Chamber

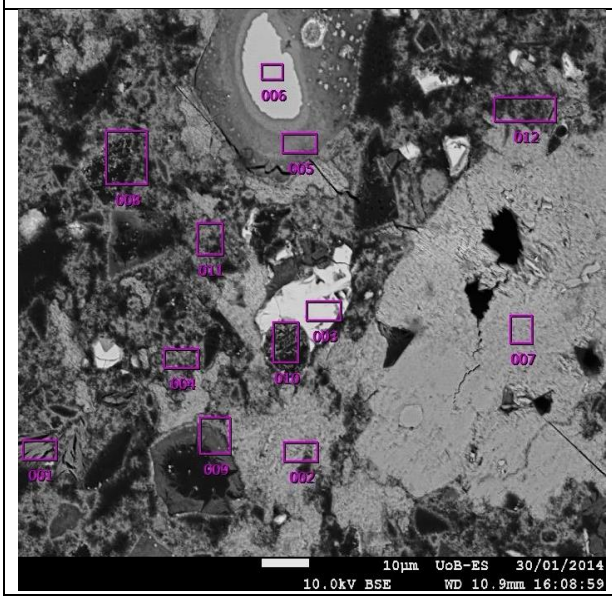

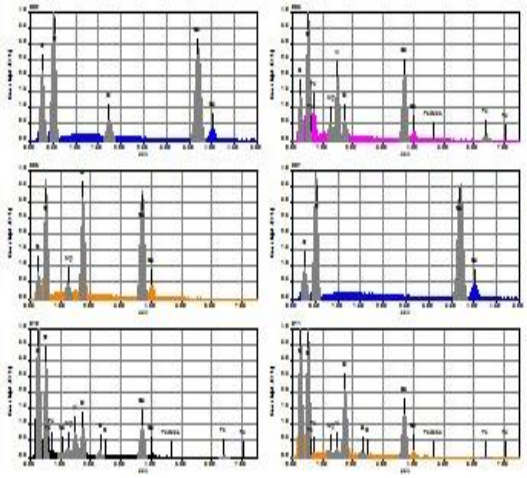

Energy Dispersive Spectroscopy, point and selected area surface analysis from the sample shown in BSE image, left.

Figure 36: Left to right SEM micrographs depicting the CSH micro-structure of Class H cement cured at 22^{0}C vs 90^{0}C, both images acquired at 6500x magnification. Agglomeration of large CSH causes increased porosity for 90^{0}C, cured samples as reported in literature for Portland cement based materials. Lower micrograph is BSE image of a polished 90^{0}C cured cement thin section, showing much more complexity than the fractured surface. Lower right, some typical Energy Dispersion Spectra acquired from the sample (areas highlighted in BSE micrograph).

which is critical for establishing effect of thermal cycling on wellbore cement compositional changes. This suggest that future studies need to focus more on polished samples as they have higher level of accuracy and produce more quantitative data.

***Subtask 4.3 – Experimental assessment of cements*:**

The experimental work was completed in 2014 Q2 and Q3. The data acquired was analyzed and integrated among different types of experimental techniques: petrophysical, microstructural, and mechanical. The data strongly suggests that the use of fibers and additives will have a positive

effect on lowering permeability and reducing impact of thermal cycling on wellbore cement. In addition, micro-mechanical strength, evaluated by micro-indentation was included. The summary of petrophysical data for ambient and thermal loading conditions are shown in Table 16 and Table 17.

Table 16: Petrophysical and Mechanical properties of cement control samples (cured in water bath at ambient conditions ~25^{0}C), based on measurements from three different samples used to calculate averages.

Cement Sample	Average Grain Density (g/cc)	Porosity (%)	Average Permeability (nD) of Control Samples	Average Unconfined Compressive Strength [psi] of Control Samples
Neat Cement	2.214±0.012	52.74±0.16	160.4±12.3	1151±331
Steel Fiber	2.270±0.011	53.47±0.24	247.4±9.6	575.5±99.0
Silica Sand	2.272±0.001	54.88±1.23	228.3±4.3	437.4±172.0
Calcined Clay	2.271±0.005	55.06±1.23	207.3±11.5	495.3±171.1
Glass Fiber	2.315±0.047	56.38±0.57	14.03±4.29	613.7±30.5

Table 2b: Petrophysical and Mechanical properties of cement designs after 100 thermal cycles, based on measurements from three different samples used to calculate averages.

Table 17: Petrophysical and Mechanical properties of cement designs after 100 thermal cycles, based on measurements from three different samples used to calculate averages.

Cement Sample	Average Density (g/cc)	Average Porosity (%)	MIP Porosity (%)	Average Permeability (nD) after 100 Thermal Cycles	Average Unconfined Compressive Strength [psi] after 100 Thermal Cycles
Neat Cement	2.343±0.015	57.41±0.608	51.41	305.2±28.9	409.6±166.1
Steel Fiber	2.363±0.072	54.36±2.895	54.18	257.7±23.5	440.1±78.09
Silica Sand	2.382±0.018	56.56±0.421	58.71	396.6±40.3	417.6±193.4
Calcined Clay	2.400±0.034	55.63±0.238	50.81	289.7±60.0	405.3±156.8
Glass Fiber	2.397±0.041	56.97±1.328	55.24	55.72±21.09	289.0±132.8

***Subtask 4.4 – Long-term testing*:**

100 thermal cyclic loading experiments were completed on each of 5 tested cement samples, at the duration of 1day per cycle, approximately 3months time period. The thermal cycle from 90^0-40^0-90^{0}C was based on the temperature range identified in the investigated LA geopressured brine field.

As shown in Figure 37, although the Elastic Modulus appeared to be lower in samples subjected to 100cycles of thermal loading (90-40-90C), the hardness values are higher after TCL in all cement samples that contained fibers/additives, only neat cement samples have lower hardness as a result of cyclic thermal loading. Therefore, the use of fibers and additives will improve cements mechanical durability under geothermal conditions.

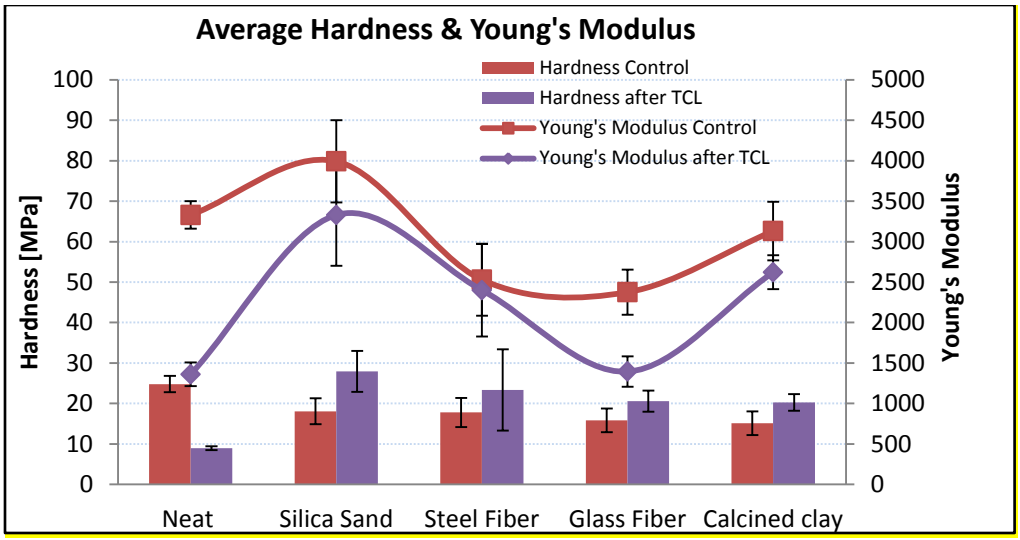

Figure 37: Micro-indentation measurements of all 5 cement designs, showing hardness and Young's modulus average values, based on 7-12 point analysis.

Relationship between physical and chemical properties of the cement design was evident in both, petrophysical and micromechanical, data. The presence of, coarse-grained calcium silicate hydrate (C-S-H) and high amount of portlandite (CH), in the neat cement design made it vulnerable to leaching of Ca^{2+}, as seen in the porosity and permeability data. Larger connectivity of these pores will provide fast pathways for ingress of low pH geofluids and rapid dissolution of cement, as reported in many geothermal field data from New Zealand for example, where CO_2 rich geofluids cause cement/casing corrosion/dissolution.

The presence of denser CSH and lower amount of CH, combined with the steel fibers, which are bridging across the pores, contributed to the low change in porosity and permeability observed in the steel fiber cement design. Even though the silica sand cement design cores have relatively low amount of $Ca(OH)_2$, they were more permeable after thermal cycle loading as there was more change in porosity on the inside of the cores due to thermally induced micro-fracturing. The permeability of the calcined clay cement cores also changed un-proportionally to its porosity due to thermal cycle loading induced fracturing.

Cement- glass fiber had a very different behavior for control conditions vs thermal loading conditions. Since glass fiber cement is alkaline, it becomes chemically unstable when the pH of cement pore water is reduced. The reduction of pH of cement slurry occurs when additional Si is available, as it reacts with $Ca(OH)_2$ in what is known as a pozzolanic reaction.

Although it produces denser final product due to higher amount of CSH produced, the pore water remaining within hydrated cement has pH <13, and therefore dissolves fine glass fiber. This reaction results in formation of an amorphous product, which lowers porosity and permeability as it clogs the pores, when compared to neat cement or any other cement design in this study. However, since amorphous material has no ability to bridge initiated fractures during thermal loading, porosity and permeability of glass fiber cement increased disproportionally comparing to other cement designs after thermal cycling. This phenomenon has been linked to reduced mechanical strength in concrete.

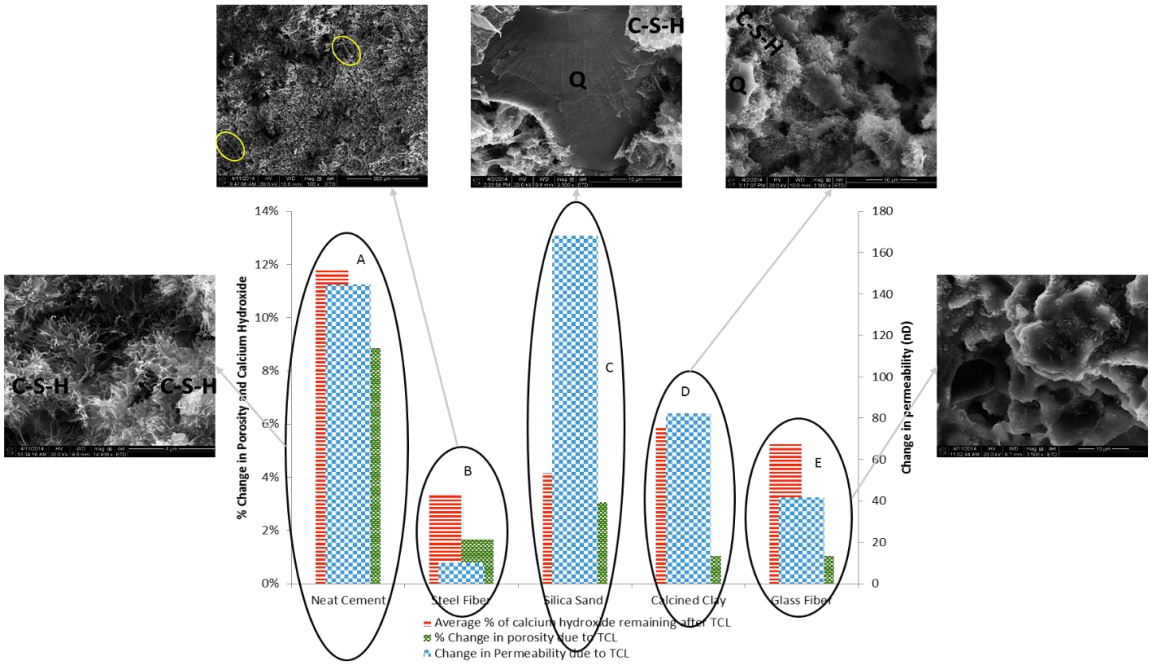

Figure 38: An integrated snapshot of the major results showing impact of thermal loading on wellbore cement designs that contain fibers and chemical admixtures and its comparison to Portland cement control sample. The goal is to compare microstructure (SEM micrographs) to the amount CH present in each of cement slurry designs tested, and how these results are related to changes in porosity and permeability of the above cements when subjected to thermal loading. In addition this is also an attempt for the quantification of the change in each cement design when compared to its control sample, which can provide approximate durability of each design under experimental conditions (time resolved behavior).

Main Observations and Conclusions:

- The liquid pressure-pulse decay permeameter provides an accurate, time efficient way to measure cement permeability with the porosity known.
  - Long, uneven fibers such as glass fibers can be used to improve permeability in wellbore cement sheath.
- Wellbore cement intended for a horizontal wellbore construction in reservoirs with high geopressured brine present will require addition of steel fibers and glass fiber along with silica flour would be necessary to increase the durability cement sheath over life of the well.
  - Similar experiment can be done with combinations and different concentration of silica sand, steel fiber, calcined clay, and glass fiber to study if the performance of calcium based cement under thermal cycling can be improved.
  - These experiments should be conducted over longer period resulting in multiple cycles.

Laboratory Utilization:

With regards to humidity/temperature chamber, it was running continuously for several months for sample curing, from June 2013 to November 2013 and then from December 2013 till end of May 2014. It allows us to cure cement in brine at high temperatures without evaporation.

The porosimeter was used to obtain core porosity and density data. We used on different types of cement slurries as well as shale, limestone samples. For this project alone almost 100 measurements were taken. Several graduate students used it for wellbore cement evaluation as

well as to measure porosity and density of the shale samples from Livingston parish for the CO_2 sequestration-eor project, originally sponsored by the DOE and BlackHorse. In addition, we trained undergraduate students to use it as part of their senior design projects in 2013, 2014 and 2015.

The permeameter was continuously used because the setup and measurements takes longer (approximately a sample/day). For this project we have analyzed over 80 samples. The permeameter can also be used for flow through experiments.

Currently the core-flooding unit (CFS) of the geothermal system is being used for differential pressure (Δp) data acquisition of artificially fractured shale rocks. This unit is fitted with two sensitive dp transducers that can accurately measure pressure changes ranging between 5 psi and 400 psi. The Δp data is automatically logged at operating temperature and pressure conditions providing useful in-situ information for fracture conductivity estimation. Core-length compressibility can also be measured for dynamic poisson's ratio estimation during the flooding process, and we intend to continue to utilize this capability.

New Contacts Established as a result of this research and potential for future collaborations:

- Dr. Toshifumi Sugama (Brookhaven National Lab, New York)
- Dr. N. Milestone, Callaghan Innovation Advanced Materials Lab, NZ
- Dr. A. Durandt, James Hardie company, AU

Acknowledgment:

- Dr. Dongmei Cao (Material Characterization, Institute of Advanced Materials Shared Facility Lab);
- Wanda Leblanc (Geology Department, LSU);
- Dr. Amitava Roy (CAMD, LSU)
- Richard Dubious (Halliburton Drilling Fluids Lab), Rodney Macon (tXI)

Publications and Presentations:

1. Radonjic, M., Bello, K. Experimental Assessment of Cement Integrity under Geopressured Geothermal Reservoir Conditions. *Presented at World Geothermal Congress*, Melbourne, Australia, (April, 2015).

2. Bello, K. and Radonjic, M.: "Petrophysical And Microstructural Evaluation Of The Thermal Cycle Loading Effect On Geothermal Wellbore Cements" *Journal of Porous Media*, 18 (2): 137–151 (2015)

3. Bello, K.S., 2014, *Experimental Assessment Of Cement Integrity Under Thermal Cycle Loading Conditions In Geopressured Geothermal Reservoirs*, M.S. Thesis, Louisiana State University, 110 p. http://etd.lsu.edu/docs/available/etd-09022014-111540/

4. Bello, K. and Radonjic, M.: "The Effect of Geofluids on Wellbore Cement under Thermal Cycle Loading Conditions" presented at the 38th Annual Meeting and GEA Energy Expo, September 28 - October 1, 2014, Portland, OR

5. Bello, K. and Radonjic, M.: "Evaluation of Wellbore Cement Integrity in Contact With High Temperature Brine" presented at the 48th US Rock Mechanics Geomechanics Symposium (ARMA), Minneapolis, MN, USA, June 1 – 4, 2014.

6. Bello, K. and Radonjic, M.: "Use of Liquid Pressure –Pulse Decay Permeameter in Experimental Evaluation of Permeability in Wellbore Cement under Geopressured Geothermal Conditions", presented at the 5th International Conference on Porous Media and its Applications in Science and Engineering (ICPM5), Keauhou Bay, Kona, Hawaii, USA, June 22 – 27, 2014.

7. Bello, K. and Radonjic, M.: "Experimental Investigation of the Onset of Strength Regression in Wellbore Cement under Geopressured Geothermal Conditions using Liquid Pressure-Pulse Decay Permeameter", poster presentation at the 2013 AGU Fall meeting, San Francisco, CA (December, 2013).

Figure 39 Geothermal fluids that reach the surface are rich in S, CO2, Geothermal location in New Zealand, May 2015, M. Radonjic

Task 5 – Geomechanics

Geothermal energy has been recognized as a clear renewable energy source and has been successfully used in some parts of the world for generating electricity or residential heating. However, exploiting this natural source has faced challenges that made its character as a clear or renewable source in jeopardy. Production and injection of water in unconsolidated formation could cause subsidence on surface and or compaction at the reservoir depth, both of these issues could damage wellbore integrity in the long term. Deformations associated with fluid production or pressure changes in unconsolidated or poorly consolidated reservoirs can lead to reservoir compaction, permeability loss, land surface subsidence, fracture gradient decrease, well shearing and, potentially, fault reactivation. These production-induced deformations can have significant impacts on the production process, surface facilities and the surface environments in the vicinity of the hydrocarbon reservoir. Examples of subsidence above the compacting gas/oil fields may found in Long Beach (California), in Venezuela, in the North Sea (Ekofisk field), or in the coastal area of the northern Adriatic Sea, Italy (due to gas injection) (Ferronato 2001), among others. In rare cases, if the depleted formation is significantly less compressible than the surrounding medium, the vertical reservoir shrinkage is relatively smaller than the horizontal one, thus generating a possible swelling of the overburden or decrease of the subsidence.
To predict the stress changes and the severity of the deformations, it is essential to understand the physical and mechanical properties of the producing formations in response to depletion. Reliable models that can capture all these effects are needed. If the fluid extraction from geothermal reservoirs exceeds the rate of reservoir fluid substitution, reservoir pressure decreases; however, pressure drop could also happen due to the temperature drop. Drop of pore pressure will increase effective stress and may induce subsidence or activates near faults. Disposal of produced water and induced earthquakes are two major issues that have endangered development of the geothermal energy as a renewable source of energy. To avoid these problems, circulation of fluid in a closed loop system has been pursued in this project. We considered the heat exchange problem in closed loop systems a thermoelasoplasticity problem. Thermoporoelasticity studies the interaction of heat flow, fluid flow and rock deformation through porous media. Thermoporoelasticity can have wide applications from heat extraction from geothermal reservoirs to design of artificial fractures in hydrocarbon reservoirs. Land subsidence can be a main issue during heat extraction from the geothermal reservoirs. Heat extraction from the geological formation reduces the formation temperature along the producing zone. The temperature drop may reduce the pore pressure through the porous medium around the production zone. Pore pressure reduction raises the effective stress and result in land subsidence. This mechanism is more important for the closed loop geothermal systems where there is no injection of working fluid thorough the geothermal reservoir. However in the open loop systems, the reduction of pore pressure by exploiting of formation fluid from the underground can exacerbate the land subsidence.

The concept of coupling between fluid flow and solid grains was introduced by Terzaghi (1925). Terzaghi developed a one-dimensional consolidation model to study the behavior of fully saturated soils undergoing a constant loading. He showed the role of effective stress on grains deformation. However, Biot (1941) was the person who established the general theory of three-dimensional consolidation based on the efforts of Terzaghi (1925). In Biot's formulation, the interstitial fluid has the incompressible property. Rice and Cleary (1976) developed the Biot's formulation for compressible fluids. Biot's poroelasticity theory is the basic framework to

predict the reservoir compaction, land subsidence and borehole damage in the energy exploitation from both the geothermal and petroleum reservoirs (Geertsma, 1973; Du, 2001; Segall and Fitzgerald, 1998; Wang and Dusseault, 2003; Chen and Ewy, 2005).

Heat conduction and heat convection are two main mechanisms controlling the heat transfer through the porous media. During the heat conduction, the heat transfer is governed by the molecular vibrations of solid grains and fluid particles without their bulk motions. Conversely, bulk movement of fluid particles controls the heat transfer through the convection. Having heat conduction, convection or both of them depends on the texture of porous medium. For instance, the convection in very low permeable rocks, due to very small flow rate through the reservoir, can be neglected compared to the heat conduction (McTigue, 1986). However, during the heat extraction from geothermal reservoirs or hydrocarbon exploitation, the rate of fluid flow is not as low causing negligible heat conduction compared to heat convection. McTigue (1986) developed the previous work through considering the non-isothermal situations. He considered the effects of compressibility and thermal expansion of both of pore fluids and solid grains. However, he neglected the effect of heat convection and phase change which can be important in the open-loop geothermal systems. Moreover, he did not present a coupled solution to the Thermoporoelasticity problem.

Governing Equations of Thermoporoelasticity

Momentum Balance Equation. In a porous media fully saturated with water, the linear momentum balance equation can be rewritten in the form of following equation where *s* and *w* superscripts refer to solid-phase and water-phase. σ, $\sigma^{''}$, ρ, g, φ, α, and P^w are symbols of total stress, effective stress, density, gravitational acceleration, porosity, Biot's coefficient, and pore pressure.

$$L^T \sigma + \rho g = 0$$

$$L^T = \begin{bmatrix} \frac{\partial}{\partial x} & 0 & 0 & \frac{\partial}{\partial y} & 0 & \frac{\partial}{\partial y} \\ 0 & \frac{\partial}{\partial y} & 0 & \frac{\partial}{\partial x} & \frac{\partial}{\partial z} & 0 \\ 0 & 0 & \frac{\partial}{\partial z} & 0 & \frac{\partial}{\partial y} & \frac{\partial}{\partial x} \end{bmatrix}$$

$$\rho = (1-\phi)\rho^s + \phi\,\rho^w$$

$$\sigma = \sigma^{''} - \alpha\, m\, P^w$$

$$m = [1,1,1,0,0,0]^T$$

Mass Balance Equation. The following mass balance equation for the fully saturated water-phase is given as follows where β is the thermal expansion coefficient. K_w, K_s, u, k, and μ^w are bulk modulus of water, bulk modulus of solid, solid displacement, permeability, and water viscosity.

$$\left(\frac{\alpha-\phi}{K_s}+\frac{\phi}{K_w}\right)\frac{\partial P^w}{\partial t}+\alpha m^T L\frac{\partial u}{\partial t}-\beta_{sw}\frac{\partial T}{\partial t}+\nabla^T\left[\frac{k}{\mu^w}\left(-\nabla P^w+\rho^w g\right)\right]=0$$

$$\beta_{sw}=(\alpha-\phi)\beta_s+\phi\beta_w$$

$$\nabla=\left\{\frac{\partial}{\partial x},\frac{\partial}{\partial y},\frac{\partial}{\partial z}\right\}^T$$

Energy Balance Equation. The Enthalpy balance equation having both the conductive and convective terms is representative of energy equation where

$$\left(\rho C_p\right)_{eff}\frac{\partial T}{\partial t}+\left(\rho_w C_p^w\frac{k}{\mu^w}\left(-\nabla P^w+\rho^w g\right)\right).\nabla T-\nabla^T\left(\chi_{eff}\nabla T\right)=0$$

$$\left(\rho C_p\right)_{eff}=\rho_s C_p^s+\rho_w C_p^w$$

$$\chi_{eff}=\chi_{dry}\left(1+\frac{4\phi\rho^w}{(1-\phi)\rho^s}\right)$$

Based on the above calculations, the governing equations can be written as

$$\begin{bmatrix}0&0&0\\0&H&0\\0&0&K_t\end{bmatrix}\begin{Bmatrix}\bar{u}\\\bar{p}^w\\\bar{T}\end{Bmatrix}+\begin{bmatrix}K_T&-Q&K_{tT}\\Q^T&S&R\\0&0&C_t\end{bmatrix}\frac{\partial}{\partial t}\begin{Bmatrix}\bar{u}\\\bar{p}^w\\\bar{T}\end{Bmatrix}=\begin{Bmatrix}\frac{\partial f_u}{\partial t}\\f_p\\f_T\end{Bmatrix}$$

To solve the dynamic problem, the central difference in time is applied to the above general equations

$$\begin{bmatrix}0&0&0\\0&H&0\\0&0&K_t\end{bmatrix}\begin{Bmatrix}\bar{u}\\\bar{p}^w\\\bar{T}\end{Bmatrix}+\begin{bmatrix}K_T&-Q&K_{tT}\\Q^T&S&R\\0&0&C_t\end{bmatrix}\frac{\partial}{\partial t}\begin{Bmatrix}\bar{u}\\\bar{p}^w\\\bar{T}\end{Bmatrix}=\begin{Bmatrix}\frac{\partial f_u}{\partial t}\\f_p\\f_T\end{Bmatrix}$$

$$\begin{bmatrix}-K_T&Q&K_{tT}\\Q^T&S-(1-\theta)\Delta tH&R\\0&0&C_t-(1-\theta)\Delta tK_t\end{bmatrix}\begin{Bmatrix}\bar{u}_n\\\bar{p}_n^w\\\bar{T}_n\end{Bmatrix}-\begin{bmatrix}0&0&K_{tT}\\0&0&R\\0&0&0\end{bmatrix}\begin{Bmatrix}0\\0\\\bar{T}_{n+1}^{(p)}\end{Bmatrix}+\Delta t\begin{Bmatrix}\frac{\partial f_u}{\partial t}\\f_p\\f_T\end{Bmatrix}=$$

$$\begin{bmatrix}-K_T&Q&0\\Q^T&S+\theta\Delta tH&0\\0&0&C_t+\theta\Delta tK_t\end{bmatrix}\begin{Bmatrix}\bar{u}_{n+1}\\\bar{p}_{n+1}^w\\\bar{T}_{n+1}\end{Bmatrix}$$

In the next section, we demonstrate several verification example to make sure that our numerical code can reproduce same results for the problems with available analytical solutions. Obviously, these solutions are available only for simple geometries.

Verifications for the Numerical Code

Mandel's Problem. A rectangular soil sample subjected to a constant vertical stress at its top, through a rigid and frictionless plate of width 2a, with drainage to the two sides in lateral direction. The deformation of the sample is forced to be in plane strain conditions, by preventing all deformation in the direction perpendicular to the plane shown in Figure 40. At time t = 0 a uniform vertical load of magnitude q is applied, and this load is supposed to remain constant. It can be assumed that at the instant of loading the pore pressure distribution will be homogeneous, but as soon as drainage starts the pore pressures at the two sides, for x = −a and x = +a, are reduced to zero, and the pore pressures in the interior of the sample will gradually be reduced to zero (Figure 41).

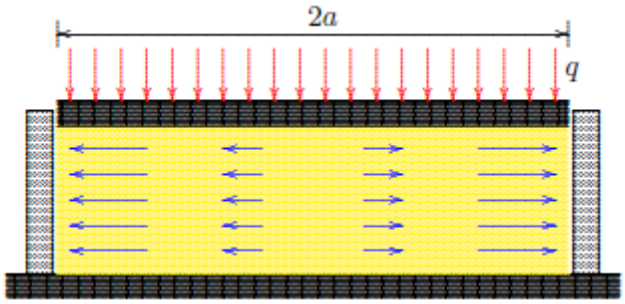

Figure 40: Schematic picture of the sample subjected to a constant vertical stress at its top

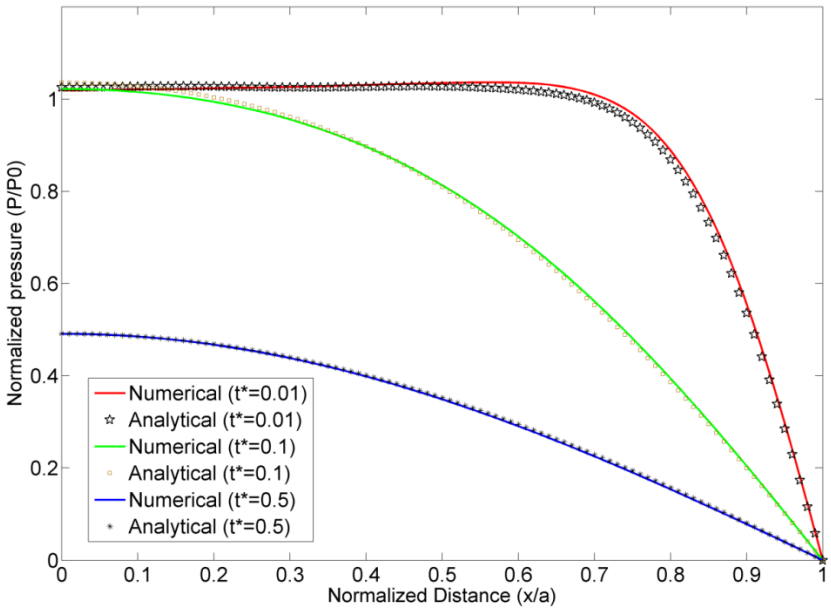

Figure 41: Comparison of the numerical and analytical normalized pore pressure inside the sample after the fluid is allow to freely flow through the sides, plotted in different time intervals.

Elder's Problem. Elder problem is an example of free convection, where the fluid flow inside the model is driven by density differences. Elder (1967) studied the effect of thermal convection in a porous medium being heated from the bottom. The original experiment, called the short-heater problem, was performed in a Hele-Shaw cell, which provides a laboratory analogue for

flow in porous media. Elder conducted these studies mainly to verify the finite difference model he developed for the two-dimensional simulation of thermal-driven convection and provided his results graphically for the temperature and stream-function fields. Because of its complexity, Elder's problem is typically used as a benchmark in flow-transport problems.

The Elder problem consists of a two-dimensional water-saturated rectangular porous volume. Hydrostatic pressure and uniform temperature are the initial condition and all boundaries are impervious to fluid flow. A source of heat at constant temperature is applied at part of the bottom boundary, while the temperature at the top boundary is kept constant. All remaining boundary portions are considered adiabatic (Figure 42). Dimensionless variables are as follows.

$$t^* = \frac{t}{\left[(1-\phi)\lambda_s + \phi\lambda_f\right]^{-1}\left[(1-\phi)\rho_s C_{p,s} + \phi\rho_f C_{p,f}\right]H^2}$$

$$T^* = \frac{T - T_i}{T_B - T_i}$$

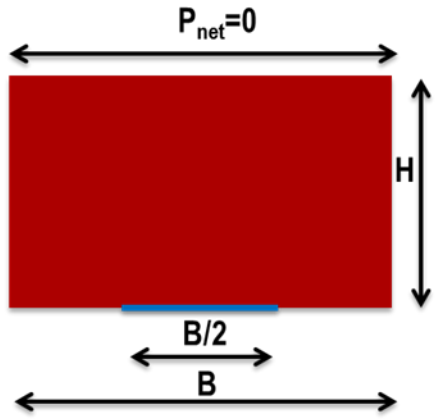

Figure 42: Schematic picture of Elder's problem subjected to a constant temperature at its half of bottom boundary.

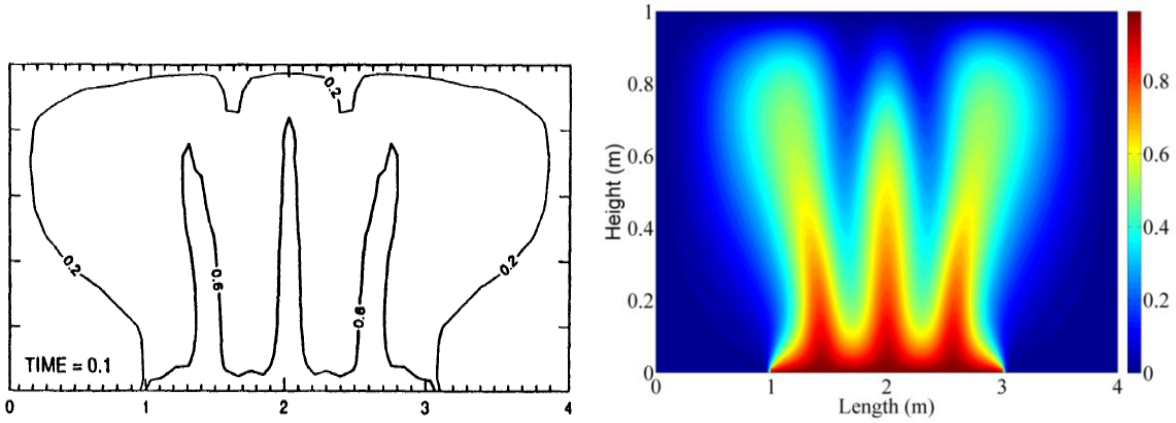

Figure 43: Dimensionless temperature if 0.1 for Elder's problem; (a) Elder; (b) this work

A Fully Coupled Mixed FEM Model for Downhole Heat Exchangers

Feng et al. (2015) showed the geofluid can have temperature drop of 100 ^{o}C along downhole heat exchangers. This report applies this temperature drop along the wellbore, where the downhole heat exchanger is located, to further calculate the temperature, pressure, displacement,

and stress distribution in a region around the wellbore. Moreover, it is assumed that the temperature drop happens linearly along the wellbore.

Figure 44 shows the schematic picture of wellbore and surrounding region used in this report. This report considers the fully coupling between temperature, pore pressure and displacement. Moreover, viscosity and density are assumed to be only functions of temperature as the pore pressure does not significantly change in abovementioned configuration. The model is under a uniform overburden of 83 MPa. The horizontal motions of its left and right boundary are restricted and the vertical displacement at the bottom boundary is also constrained to zero. Table 18 presents all the assumed parameters for this numerical study.

Table 18: Assumed parameters of reservoir and wellbore for a downhole heat exchanger

Symbol	Quantity	Value	Unit
B	Length	800	m
H	Height	200	m
L	Well length	400	m
ϕ	Porosity	0.2	
κ	Permeability	2×10^{-14}	m^2
λ_s	Rock thermal conductivity	1.9	$W\ m^{-1}\ ^oC^{-1}$
λ_f	Geofluid thermal conductivity	0.519	$W\ m^{-1}\ ^oC^{-1}$
$C_{p,s}$	Rock specific heat capacity	1000	$J\ Kg^{-1}\ ^oC^{-1}$
$C_{p,f}$	Geofluid specific heat capacity	3182	$J\ Kg^{-1}\ ^oC^{-1}$
ρ_s	Rock density	2700	$Kg\ m^{-3}$
ρ_s	Geofluid density	1000	$Kg\ m^{-3}$
μ	Geofluid viscosity	1.1×10^{-4}	Pa s
β_s	Thermal expansion coefficient of rock	0	$^oC^{-1}$
β_f	Thermal expansion coefficient of geofluid	450×10^{-6}	$^oC^{-1}$
E	Young's modulus of rock	1.38×10^{10}	Pa
ν	Poisson's ratio of rock	0.3	
α	Biot coefficient of rock	1	
T_i	Initial temperature of medium	140	^oC
$T_{f,o}$	Geofluid outlet temperature	40	^oC

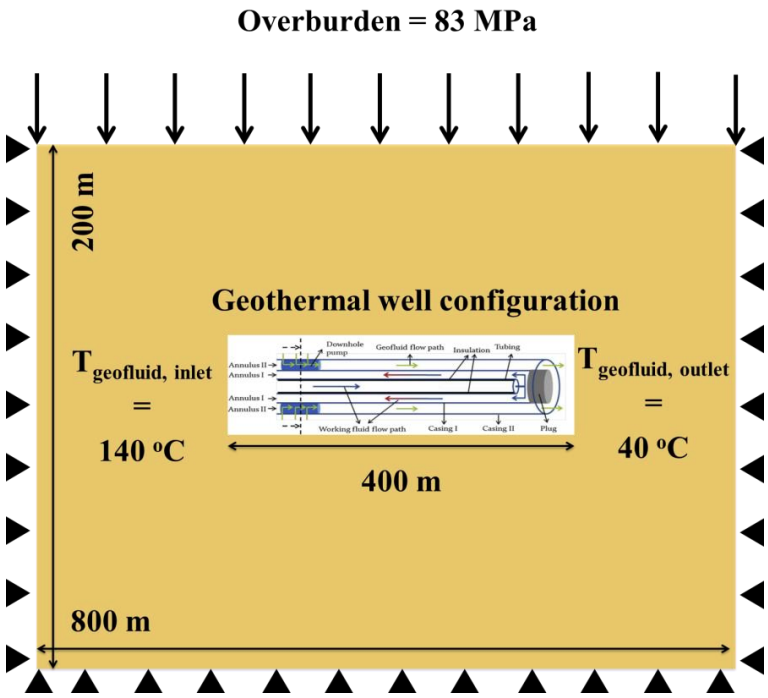

Figure 44: Schematic picture of a horizontal downhole heat exchanger in a porous hot medium.

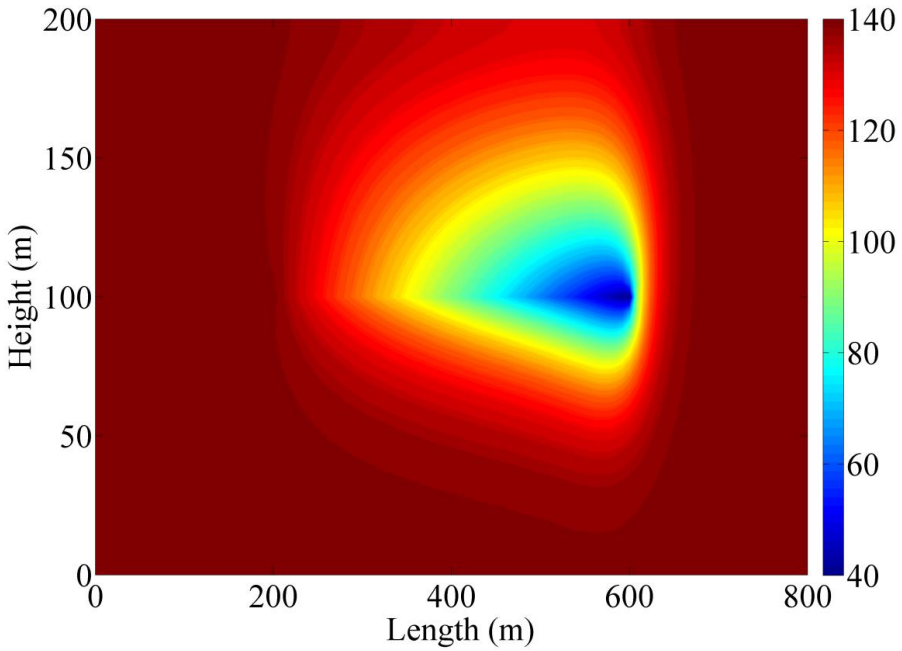

Figure 45: Temperature distribution (°C) around the wellbore after 37 years. It is assumed that the temperature drop of geofluid along the wellbore is linearly.

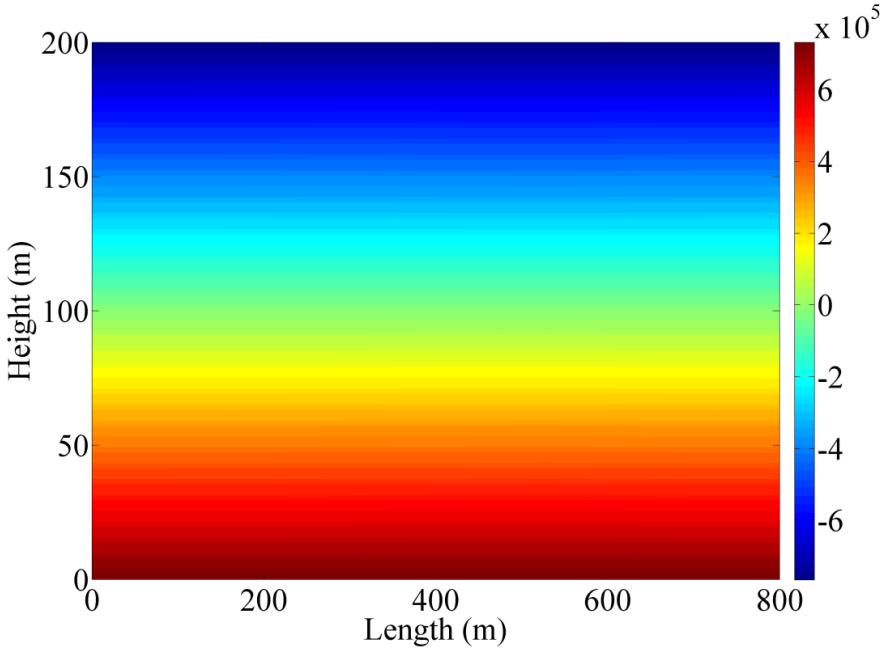

Figure 46: Net Pore pressure distribution (Pa) in the geothermal medium after 37 years. Net pore pressure means the difference between the initial pore pressure induced by overburden and current pressure.

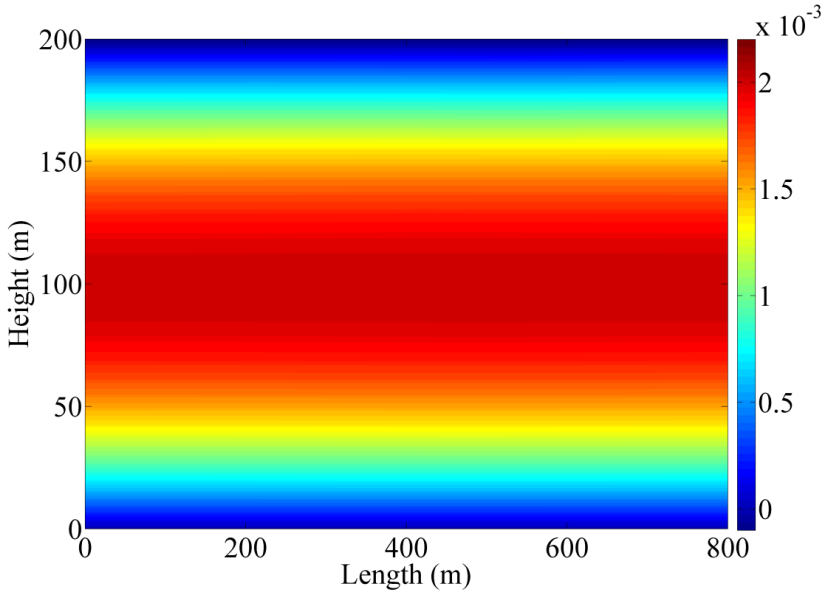

Figure 47: Net vertical displacement (m) distribution in the geothermal medium after 37 years. Net vertical displacement means the difference between the initial vertical displacement induced by overburden and current vertical displacement.

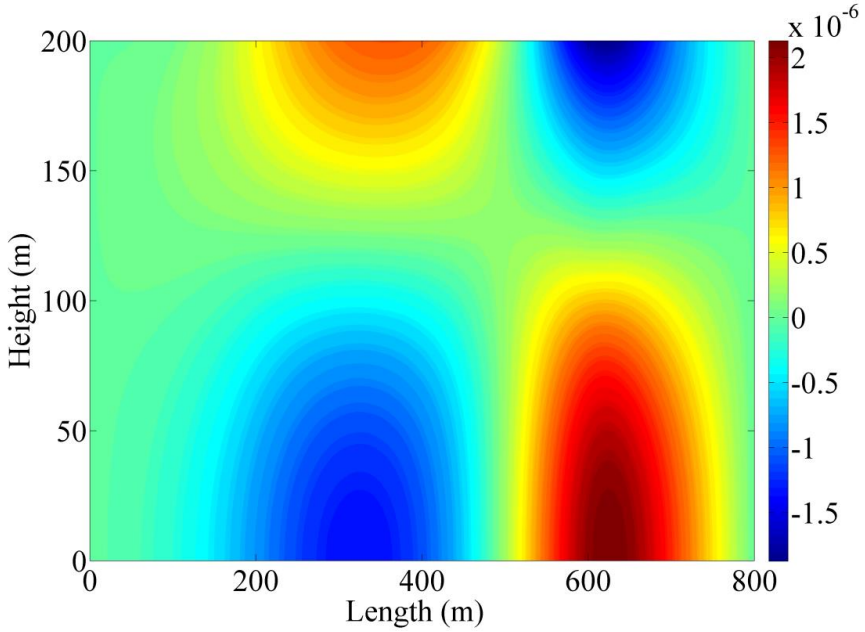

Figure 48: Net horizontal displacement (m) distribution in the geothermal medium after 37 years. Net horizontal displacement means the difference between the initial horizontal displacement induced by overburden and current horizontal displacement.

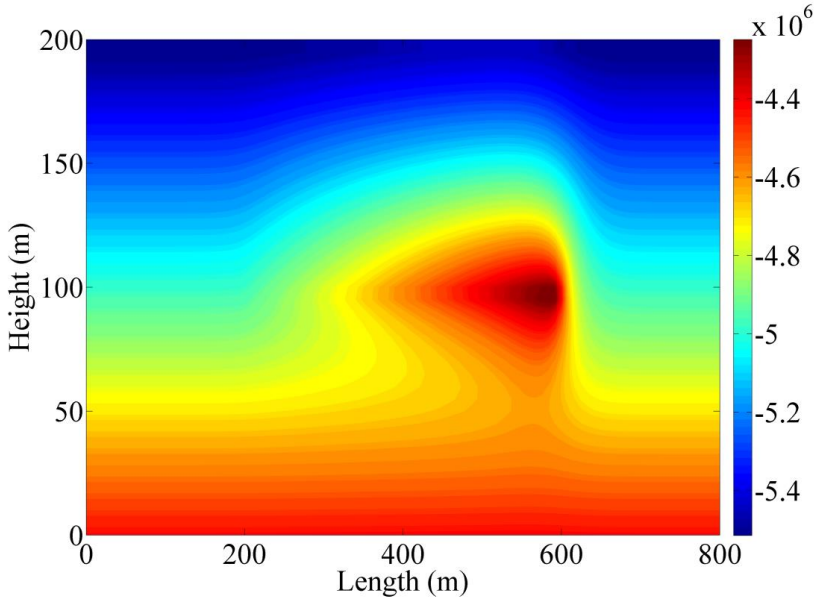

Figure 49: Net shear stress distribution (Pa) in the geothermal medium after 37 years. Net shear stress means the difference between the initial shear stress induced by overburden and current shear stress.

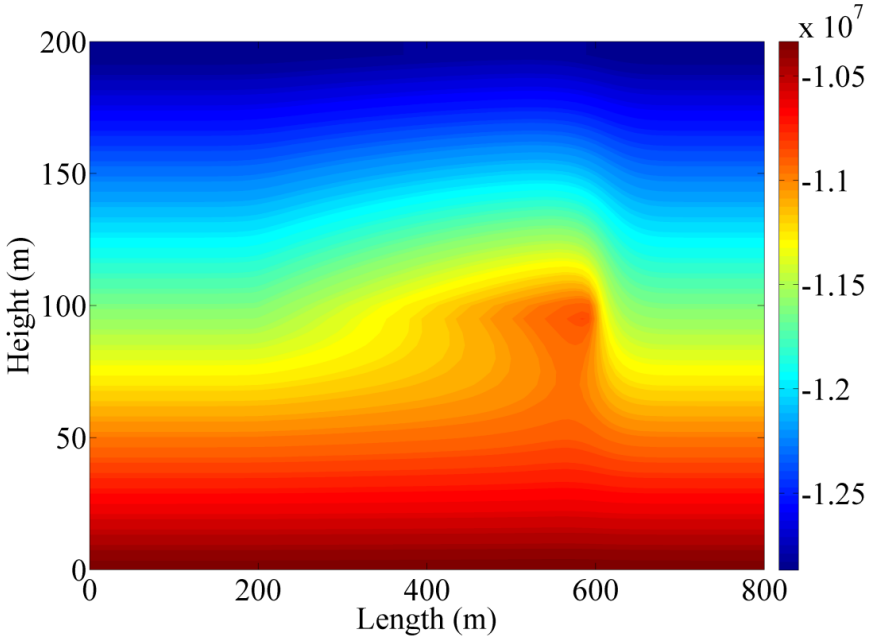

Figure 50: Net normal stress distribution (Pa) in the geothermal medium after 37 years. Net normal stress means the difference between the initial normal stress induced by overburden and current normal stress.

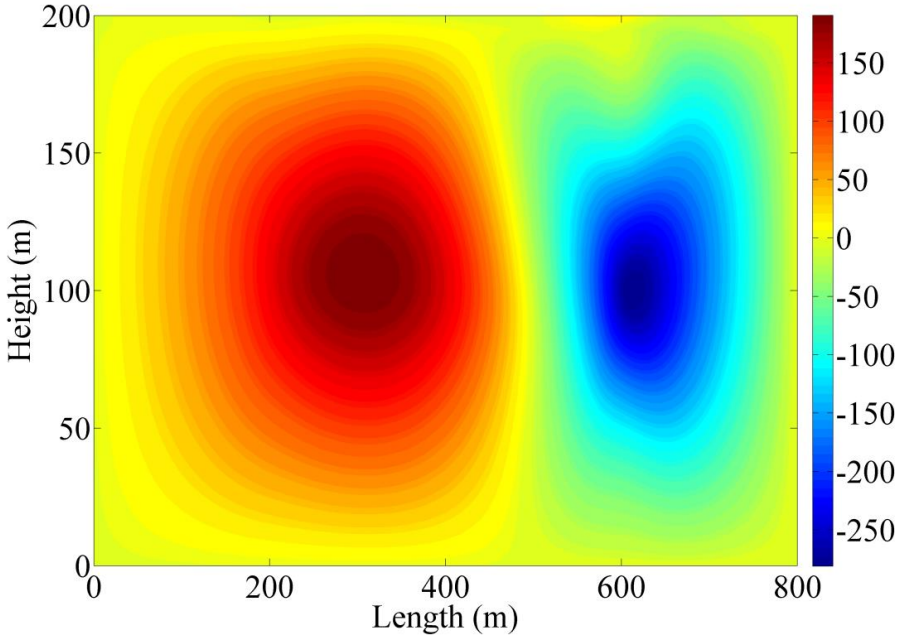

Figure 51: Net orthogonal shear stress distribution (Pa) in the geothermal medium after 37 years. Net orthogonal shear stress means the difference between the initial orthogonal shear stress induced by overburden and current orthogonal shear stress.

Seismicibility

Induced seismic events are one of the main concerns in heat extraction from the geothermal reservoirs. Injection of pressurized working fluid results in increase in pore pressure around the wellbore. This pressure gradient between the zones around and far from the wellbore may cause

to slippage of rock mass on the pre-existing fractures, known as shear stimulation (McClure and Horne, 2011). Although the rock mass slippage results in permeability enhancement, the induced seismic events by slippage are a cause of public uncertainties about the safety of Enhanced Geothermal Systems. Public fears about the natural earthquakes affect the acceptance of Enhanced Geothermal Systems (EGS). Therefore, investigation of seismicity during working fluid injection and post-injection can be very interesting topic for the problem studied in this project.

The causes of induced seismicity in the geothermal reservoirs can be categorized by change in the following parameters; coefficient of friction, pore pressure, temperature distribution around the wellbore (Allis, 1982). The role of each parameter can be different in injection or production process. During heat extraction from a geothermal reservoir, in an open-loop system, the significant increase in the effective rock stress can result in seismic events. Furthermore, increase in coefficient of friction through clay dehydration and precipitation of dissolved minerals such as silica can affect the stress distribution throughout the rock. The temperature decline around the wellbore might cause the stick-slip movement. However, its contribution is not as significant as the change in the pore pressure. McClure and Horne (2011) have found that injection-production schedule can have a considerable influence on the magnitude of seismic events. In other words, their model predicts that most of the seismic events happen right after the cease of injection because the formation starts to redistribute the pore pressure gradient throughout. The probability of post-injection seismic events can be lessened by staring the production immediately after injection (McClure and Horne, 2010). To accurately model seismicity in the geothermal reservoirs, coefficient of friction has to be a function of sliding velocity in order to model the role of coefficient of friction on quick slippage. Rate and state friction law, shown in below equation, is a common method to model dependency of coefficient of friction on sliding velocity and past sliding history. The parameters of $f_0, v_0, a, b,$ and d_c are materials constant. However, d_c is a characteristic displacement scale (Segall, 2010).

$$\mu_f = f_0 + a\ln\frac{v}{v_0} + b\ln\frac{\theta v_0}{d_c}$$

Most of the seismic studies in geothermal reservoirs have been applied for the open-loop systems. In other words, a working a cold fluid is injected through the reservoir, then the heat is extracted from hot working fluid exposed to hot rock. However, the novelty of this study is considering seismicity effect for a closed-loop system. In the closed-loop system, working fluid is circulated through a pipe run into the geothermal well. Therefore, the working fluid is not directly in contact with hot rock. In this system, there is no loss of working fluid. Change of geothermal reservoir pore pressure in seismicity induction is not significant for the closed-loop system. However, it can be significant if the closed-loop system extracts heat from a vapor-dominated reservoir. For this specific geothermal reservoir, steam condensation can reduce the pore pressure and induce seismicity. Seismicity induction for this specific case can be caused by the temperature change and intense localized cooling around the wellbore if the order of displacement is large enough.

The moment magnitude scale (denoted as M_W) is used to measure the size of earthquakes in terms of the energy released. The magnitude is based on the seismic moment of the earthquake, which is equal to the rigidity of the Earth (G) multiplied by the average amount of slip (D) on the fault and the size of the area that slipped (A). The moment magnitude (Mw) of an

earthquake is theoretically the same regardless of where the earthquake was measured, the type of recording instrument, or structure along the wave-paths.

$$M_W = \frac{2}{3}\log M_0 - 10.7$$

$$M_0 = G \times D \times A$$

Earthquakes can have a range in magnitude from a maximum of M 10 down to arbitrarily small values of M -3, monitored in the most sensitive micro-earthquake experiments. The aim of this part of this study is to show whether change of temperature distribution around the wellbore can cause large displacements to induce seismicity. The following calculation shows the magnitude of induced seismicity for the downhole heat exchanger geothermal system. Our calculation shows that induced seismicity can be negligible in the downhole heat exchanger configuration.

$$M_0 = \frac{E}{2\times(1+\nu)} * D * A = \frac{13.8\times10^9}{2\times(1+0.3)} \times 3.5\times10^{-6} \times 800 \times 200 \times 10^7 = 2.97\times10^{16} \ \ (dyne-cm)$$

$$M_W = \frac{2}{3}\log M_0 - 10.7 = \frac{2}{3} \times \log(2.97\times10^{16}) - 10.7 = 0.282$$

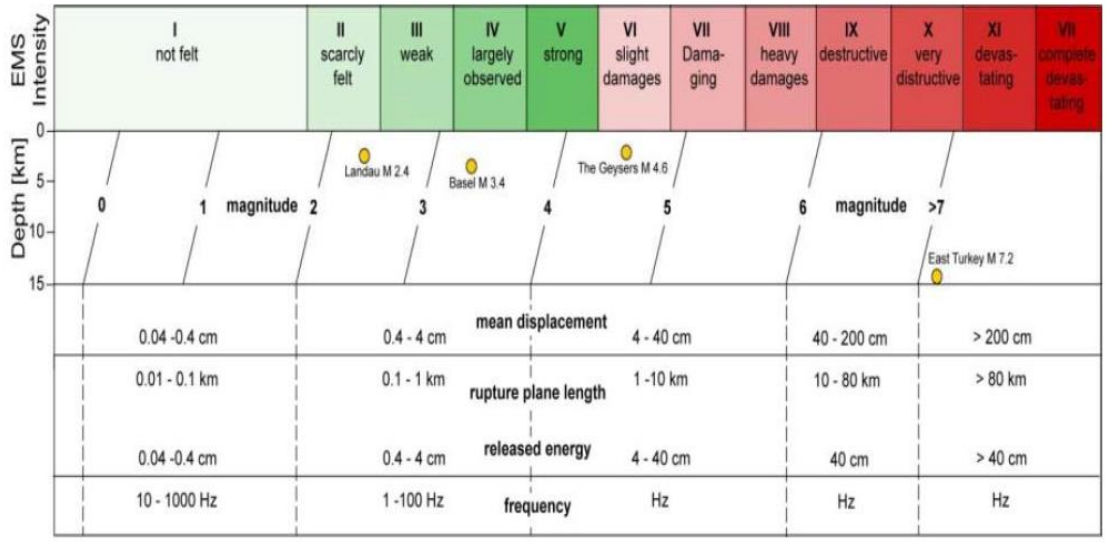

Figure 52: Magnitude of earthquakes and the range of their severity based on the depth and amplitude of displacement (www.geoelec.eu)

A similar model was developed for evaluating the two well ZMW problem. The This 2D model used a similar 6000 m × 6000 m grid system (see Figure 53) with quadratic triangular elements (six nodes per element) for displacement calculations, linear triangular elements (three nodes per element) for the temperature calculations and linear triangular elements (three nodes per element) for pore pressure calculations.

Figure 54 shows the change in thermal power and cumulative extracted heat as a function of time and given the fast thermal breakthrough represents an extreme case for the temperature and displacement modeling. Figure 55(a – d) show the temperature, pore pressure and displacement

distributions after 20 years of production and Figure 55(e) shows the amount of surface subsidence over those same 20 years. Again, displacements are very small and seismic activity is expected to be negligible.

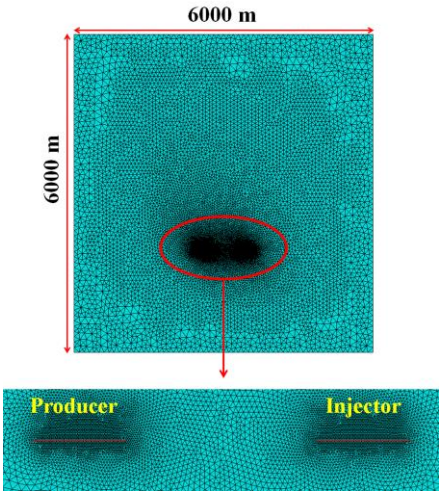

Figure 53 Grid system for modeling two well problem

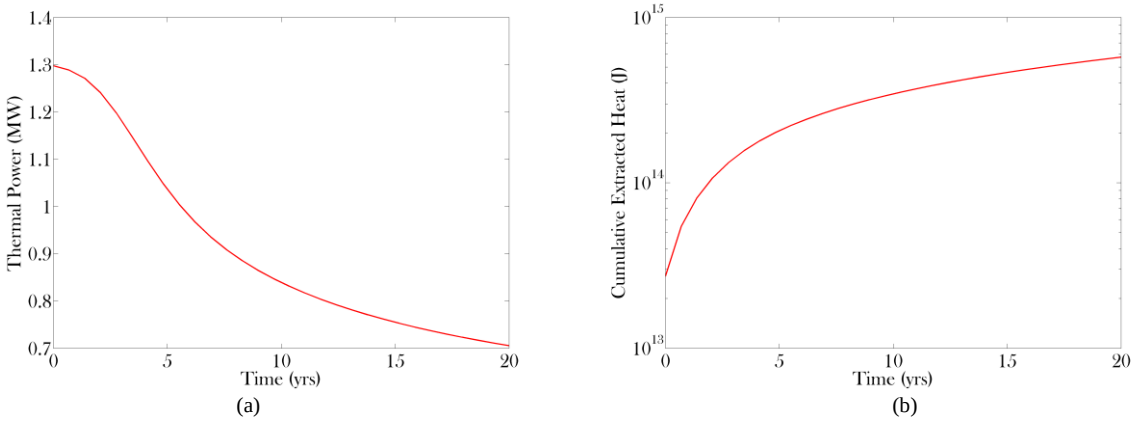

(a) (b)

Figure 54 Thermal power generated (a) and Cumulative energy extracted over time (b) for the modeled situation

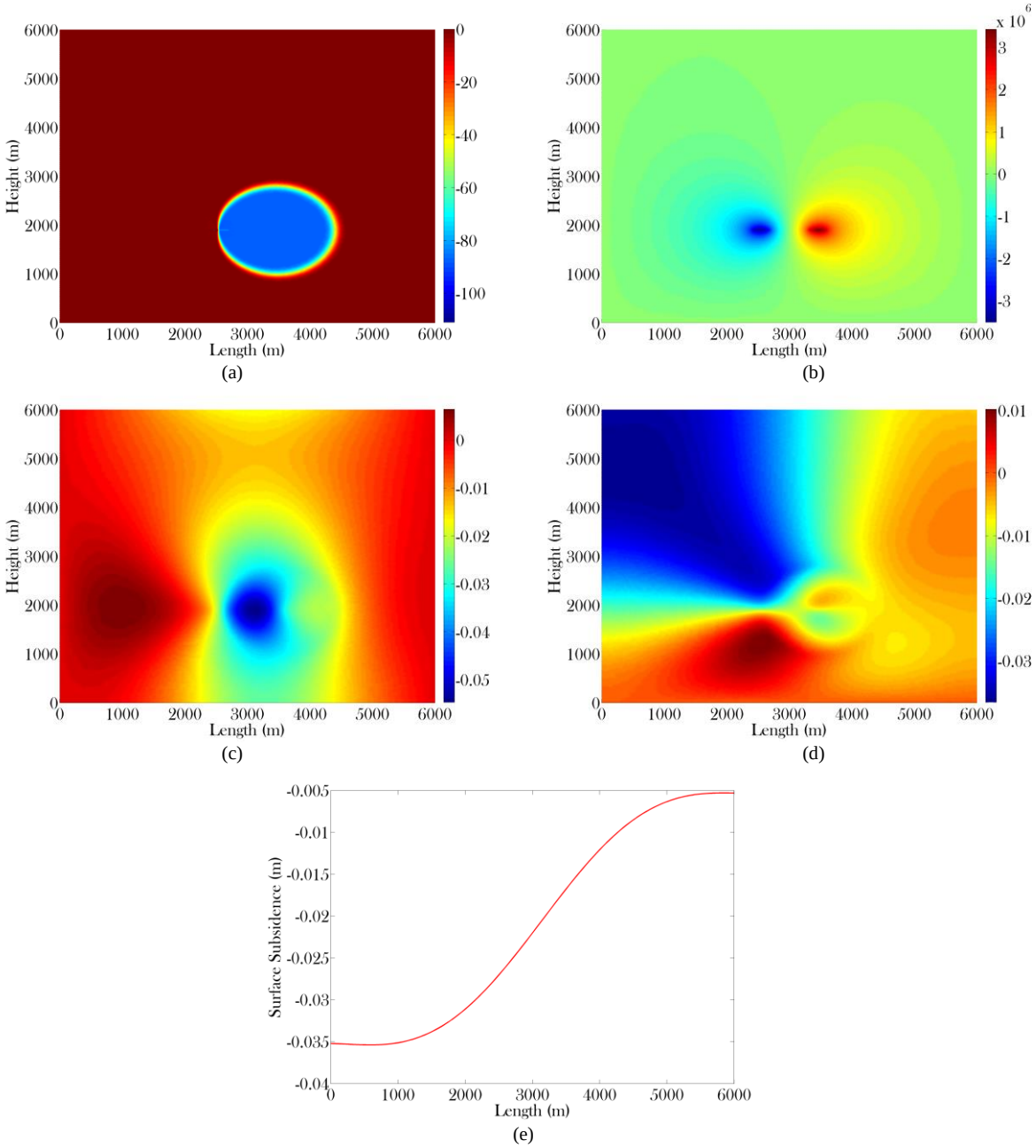

Figure 55 Temperature distribution (a), Pore pressure distribution (b), Horizontal displacement (c), Vertical displacement (d) and Surface subsidence (e) after 20 years of production for the modeled system

References:

Bai, M., and Y. Abousleiman. "Thermoporoelastic coupling with application to consolidation." *International journal for numerical and analytical methods in geomechanics* 21.2 (1997): 121-132.

Barber, J. R. "The disturbance of a uniform steady-state heat flux by a partially conducting plane crack." *International Journal of Heat and Mass Transfer* 19.8 (1976): 956-958.

Belotserkovets, Anastasia, and Jean H. Prevost. "Thermoporoelastic response of a fluid-saturated porous sphere: An analytical solution." *International Journal of Engineering Science* 49.12 (2011): 1415-1423.

Biot, Maurice A. "General theory of three- dimensional consolidation." *Journal of applied physics* 12.2 (1941): 155-164.

Coffee, Derek A. "Closed loop geothermal heat exchanger." U.S. Patent No. 6,138,744. 31 Oct. 2000.

Coussy, Olivier. *Poromechanics*. John Wiley & Sons, 2004.

Diao, Nairen, Qinyun Li, and Zhaohong Fang. "Heat transfer in ground heat exchangers with groundwater advection." *International Journal of Thermal Sciences* 43.12 (2004): 1203-1211.

Elder, J.W. "Transient convection in a porous medium." *Journal of Fluid Mechanics*, v. 27, no. 3, p. 609-623 (1967).

Feng, Y., M. Tyagi, and C. D. White. "Effect of Natural Convection Patterns on Optimal Location and Size of a Heat Sink in a Geothermal Reservoir." Proceedings of Thirty-Sixth Workshop on Geothermal Reservoir Engineering, Stanford, CA. 2011.

Feng, Yin, Mayank Tyagi, and Christopher D. White. "A downhole heat exchanger for horizontal wells in low-enthalpy geopressured geothermal brine reservoirs." *Geothermics* 53 (2015): 368-378.

Giardini, Domenico. "Geothermal quake risks must be faced." *Nature* 462.7275 (2009): 848-849.

Geertsma, J. "Land subsidence above compacting oil and gas reservoirs." *Journal of Petroleum Technology* 25.6 (1973): 734-744.

Kipp Jr, K. L. "Guide to the revised heat and solute transport simulator." HST3D--Version 2 (1997).

Kodashima, Tsuyoshi, and Michio Kurashige. "Thermal stresses in a fluid-saturated poroelastic hollow sphere." *Journal of thermal stresses* 19.2 (1996): 139-151.

Lewis, R. W., and B. A. Schrefler. "The Finite Element Method in the Static and Dynamic Deformation and Consolidation of Porous Media." *Meccanica* 34.3 (1999): 231-232.

Majer, Ernest L., et al. "Induced seismicity associated with enhanced geothermal systems." *Geothermics* 36.3 (2007): 185-222.

McTigue, D. F. "Thermoelastic response of fluid- saturated porous rock." *Journal of Geophysical Research: Solid Earth (1978–2012)* 91.B9 (1986): 9533-9542.

Rice, James R., and Michael P. Cleary. "Some basic stress diffusion solutions for fluid-saturated elastic porous media with compressible constituents." *Reviews of Geophysics* 14.2 (1976): 227-241.

Segall, Paul. "Induced stresses due to fluid extraction from axisymmetric reservoirs." *Pure and Applied Geophysics* 139.3-4 (1992): 535-560.

Taleghani, Arash Dahi. "An Improved Closed-Loop Heat Extraction Method From Geothermal Resources." *Journal of Energy Resources Technology* 135.4 (2013): 042904.

Terzaghi, Charles [Karl], 1925, Principles of soil mechanics: IV—Settlement and consolidation of clay: Eng. News-Record, v. 95, p. 874-878

Verruijt, A. "Theory and problems of poroelasticity." *Delft University of Technology, The Netherlands* (2013).

Task 6 – Economic analysis

The economic analysis team has completed their work and has published an overview paper (Kaiser, 2016). The levelized cost of electricity (LCOE) was calculated through a techno-economic analysis that included top down and bottom up estimates of capital costs associated with drilling, as well as the procurement and installation costs of the downhole heat exchanger and organic Rankine cycle turbine; operational costs associated with failures of major system components were also included. Since this work was done about a year ago, a system capacity of 200 kW was assumed. The capital (Figure 56) and operating expenses were then used to calculate the levelized cost of electricity through the DOE's System Advisor Model (SAM; see Blair et al. 2014). Three parameterizations were developed which differed in capital and operational costs and required internal rate of return (Figure 57). In general, LCOE was high and are expected to range from 24 to 78 ¢/kWh with an expected value of 62 ¢/kWh (Figure 58a).

Category	P90 ($1,000)	P50 ($1,000)	P10 ($1,000)
Downhole heat exchanger	280	340	400
Well	3,877	8,600	13,200
Electric submersible pumps	1,000	1,250	1,500
ORC turbine	320	500	1,600
Total	5,477	10,690	16,700

Figure 56 Capital Costs assumed for the optimistic, expected and pessimistic cases

Variable	Optimistic	Expected	Pessimistic
Capacity factor (%)	95	92.5	90
Capital cost ($/kW)	28,000	53,650	84,000
Capacity (kW)	200	200	200
IRR (%)	10	12.5	15
Operating cost ($/yr)	45,600	242,000	438,300
Production tax credit ($/kWh)	0	0	0
Depreciation	5 year MACRS	5 year MACRS	5 year MACRS
Investment tax credit (%)	10	10	10
Lifetime (yr)	25	25	25

Note: Variables not specified are set at the SAM default values and are identical for all scenarios.

Figure 57 Parameter values for the SAM software LCOE calculations

Due to the high LCOE estimates, we explored the sensitivity of the model to changes in the system. Figure 58b depicts the real LCOE of a system in which the drilling costs are cut in half. This could occur if rig day rates decline or if an existing well could be used, both of which have occurred in the past year. Under these circumstances, and under optimistic assumptions, LCOE is below 20 ¢/kWh. Akhmadullin (2016) provides several ways in which power can be increased to as high as 1.5 MW without increasing costs dramatically as well as revised capital costs for equipment other than drilling costs. While the LCOE is still high, for a novel system with large technological uncertainty, the potential for an LCOE below 20 ¢/kWh is relatively promising.

The relationship between increasing system capacity and LCOE was also explored (Figure 59). When system capacity increases from 200 kW to 400 kW, the LCOE declines in the expected

parameterization from 62 ¢/kWh to 32 ¢/kWh. Again, given that a 200 kW system capacity may be conservative and that system capacity could be three or four times the 200 kW value, this result is promising.

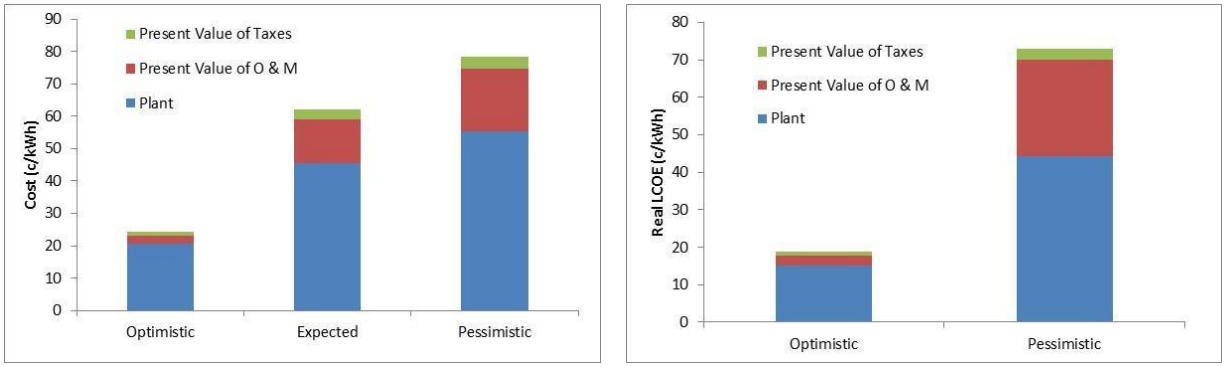

(a) (b)

Figure 58: LCOE of optimistic and pessimistic scenarios for (a) the basic set of assumptions and economic parameters and (b) for the case where drilling costs are half the value in the base set.

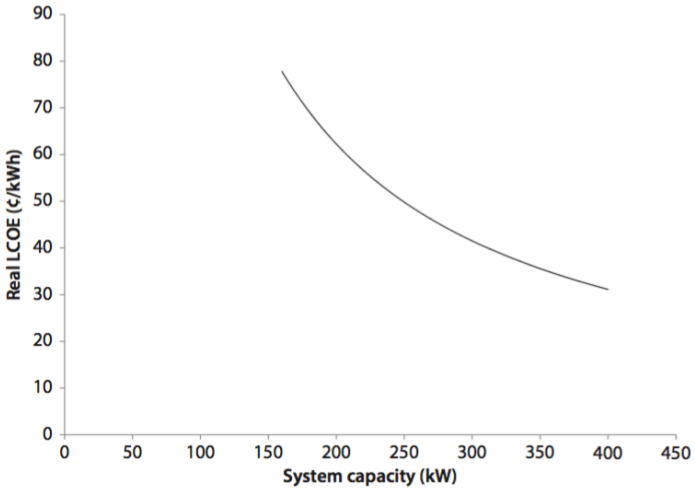

Figure 59: Relationship between system capacity and real LCOE.

References:

Akhmadullin I., *Design And Analysis Of Geothermal Wellbore Energy Conversion System Working On Zero Mass Withdrawal Principle*, PhD Dissertation, LSU, (2016)

Blair, N., Dobos, A.P., Freeman, J., Neises, T., Wagner, M., Ferguson, T., Gilman, P. and Janzou, S., System Advisor Model, SAM 2014.1.14: General Description. National Renewable Energy Laboratory Technical Report NREL/TP-6A20-61019 (2014).

Kaiser, M. "Economic Analysis of a Zero-Mass Withdrawal Geothermal Energy System." *Journal of Sustainable Energy*, Vol. 3, No. 3 (2016): 191-220.

Task 7 – Geospatial Analysis

A stand-alone document entitled: "Environmental and social aspects of geothermal development in Louisiana" is attached as an Appendix to this document.

Task 8 – Reporting

None besides this report.

Products / Deliverables

Publications, Conference Papers, and Presentations:

Ahmadi, M., 2016: *Application of the Finite Element Methods to Solve Coupled Multiphysics Problems for Subsurface Energy Extraction*, PhD Dissertation, Louisiana State University.

Ahmadi, M.; Dahi Taleghani, A.; "Changes in Fracture Compliance Due to Roughness", H53D-0883, 2014 AGU Conference, San Francisco, California, United States of America, 15-19 December 2014.

Ahmadi, M.; Dahi Taleghani, A.; Sayers, C.: "The effect of slickensides on fracture compliance", ID: GJI-S-14-0723 (Under review by Geophysical Journal International).

Ahmadi, M.; Dahi Taleghani, A.; Sayers, C.: "Direction dependence of fracture compliance ratio induced by slickensides", ID: GEO-2013-0227, Published May, 23 2014.

Akhmadullin, I. and Tyagi, M.: "Design and Analysis of Electric Power Production Unit for Low Enthalpy Geothermal Reservoir Applications", presented at the International Conference on Turbomachinery and Fluid Dynamics (ICTFD) held in New York, USA, June, 5-6, 2014.

Akhmadullin, I., 2016: *Design And Analysis Of Geothermal Wellbore Energy Conversion System Working On Zero Mass Withdrawal Principle*, PhD Dissertation, Louisiana State University, 148 p. http://etd.lsu.edu/docs/available/etd-07072016-142902/unrestricted/Akhmadullin_Diss.pdf

Ansari, E., 2016: *Mathematical Scaling And Statistical Modeling Of Geopressured Geothermal Reservoirs*, PhD Dissertation, Louisiana State University, 154 p.

Ansari, E., Hughes, R.G., and White, C.D.: "Statistical Modeling of Geopressured-Geothermal Reservoirs", paper submitted to *Computers & Geosciences*.

Ansari, E., Hughes, R.G., and White, C.D.: "Modeling a New Design for Extracting Energy from Geopressured Geothermal Reservoirs", paper submitted to *Geothermics*.

Ansari, E., Hughes, R.G., and White, C.D.: "Well Placement Optimization for Maximum Energy Recovery from Hot Saline Aquifers", paper SGP-TR-202 in PROCEEDINGS, Thirty-Ninth Workshop on Geothermal Reservoir Engineering, Stanford University, Stanford, California, February 24-26, 2014

Ausburn, M.E., 2013, *Controls on the composition of saline formation waters in coastal and offshore Louisiana*, M.S. Thesis, Louisiana State University, 95 p. http://etd.lsu.edu/docs/available/etd-05302013-141118/

Ausburn, M.E., and Hanor, J.S.: "Geochemical characterization of formation waters and sediments from an area of south-central Louisiana with implications for geothermal energy production", *Gulf Coast Association of Geologic Societies Transactions*, v. 63, p. 67 – 77, 2013.

Bello, K. and Radonjic, M.: "Experimental Assessment of Cement Integrity Under Geopressured Geothermal Reservoir Conditions", World Geothermal Congress 2015, Melbourne, Australia, 19th -24th April 2015.

Bello, K.S., 2014, *Experimental Assessment Of Cement Integrity Under Thermal Cycle Loading Conditions In Geopressured Geothermal Reservoirs*, M.S. Thesis, Louisiana State University, 110 p. http://etd.lsu.edu/docs/available/etd-09022014-111540/

Bello, K. and Radonjic, M.: "Petrophysical And Microstructural Evaluation Of The Thermal Cycle Loading Effect On Geothermal Wellbore Cements" *Journal of Porous Media,* v.18 Is. 2, p. 137 – 151, 2015.

Bello, K. and Radonjic, M.: "The Effect of Geofluids on Wellbore Cement under Thermal Cycle Loading Conditions" presented at the 38th Annual Meeting and GEA Energy Expo, September 28 - October 1, 2014, Portland, OR

Bello, K. and Radonjic, M.: "Evaluation of Wellbore Cement Integrity in Contact With High Temperature Brine" presented at the 48th US Rock Mechanics Geomechanics Symposium (ARMA), Minneapolis, MN, USA, June 1 – 4, 2014.

Bello, K. and Radonjic, M.: "Use of Liquid Pressure –Pulse Decay Permeameter in Experimental Evaluation of Permeability in Wellbore Cement under Geopressured Geothermal Conditions", presented at the 5th International Conference on Porous Media and its Applications in Science and Engineering (ICPM5), Keauhou Bay, Kona, Hawaii, USA, June 22 – 27, 2014.

Bello, K. and Radonjic, M.: "Experimental Investigation of the Onset of Strength Regression in Wellbore Cement under Geopressured Geothermal Conditions using Liquid Pressure-Pulse Decay Permeameter", poster presentation at the 2013 AGU Fall meeting, San Francisco, CA (December, 2013).

Dahi Taleghani, A; Ahmadi, M.; Wang, W., Olson, J.E: "Thermal Reactivation of Microfractures and Its Potential Impact on Hydraulic Fractures Efficiency", SPE-163872-PA, *SPE Journal*, October, 2014.

Dahi Taleghani, Arash: "An Improved Closed-Loop Heat Extraction Method From Geothermal Resources", *Journal of Energy Resources Technology*, v. 135, December, 2013.

Dutrow, B.L.: "A Geochemical perspective: Geothermal Resource Development with Zero Mass Withdrawal, Engineered Convection, and Wellbore Energy Conversion", presented at the LBNL/DOE Geochemical/EGS Workshop, November 11 – 12, 2013.

Feng, Y., Tyagi, M., and White, C.D.: "A Novel Downhole Heat Exchanger Concept for Saturated Low-Enthalpy Geothermal Resources" *Geothermics*, v.53, p. 368 – 378, January 2015.

Feng, Y.: *Numerical Study of Downhole Heat Exchanger Concept for Geothermal Energy Extraction from Saturated and Fractured Reservoirs*, Ph.D. Dissertation, 116 p. http://etd.lsu.edu/docs/available/etd-07112012-041823/

Safari-Zanjani, M., 2016: *Impacts of Rock-Brine Interactions on Petrophysical Properties of a Sandstone Reservoir, Utilizing Geochemical and Pore Network Modeling*, PhD Dissertation, Louisiana State University.

Safari-Zanjani, M., White, C.D., and Hanor, J.S.: "Impacts of Rock-Brine Interactions on Sandstone Properties in Lower Miocene Sediments, Southwest Louisiana", in PROCEEDINGS, Thirty-Eighth Workshop on Geothermal Reservoir Engineering, Stanford University.

Safari-Zanjani, M. and Sears, S.O.: "Impacts of Rock-Brine Interactions on Sandstone Properties in Lower Miocene Sediments, Southwest Louisiana", submitted for publication in *Geothermics*

Geospatial Analysis Appendix Follows

Environmental and social aspects of geothermal development in Louisiana

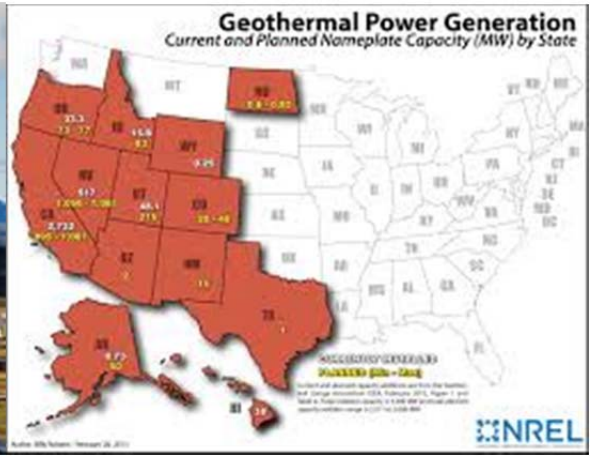

Fahui Wang and Yanqing Xu

Contact: fwang@lsu.edu and yxu28@tiger.lsu.edu

Department of Geography & Anthropology, Louisiana State University

Table of Contents

List of Tables

List of Figures

Introduction

Geothermal energy is thermal energy generated by heat stored beneath the earth's surface that can be used as geothermal power generation. It can also be used as geothermal heat pumps, greenhouses, aquaculture, and agricultural drying (Lund, Freeston and Boyd 2005). The United States is the largest geothermal electricity production county in the world and most of the power plants are located in the western areas. Geothermal is clean with very low emissions and safe for surrounding environment. Greater use of geothermal power can reduce air pollution as compared to greater use of fossil-fuel generation. The American Lung Association estimates that power plant emissions, primarily from coal plants, result in over 30,000 yearly deaths (Kagel 2006). Beside the environmental aspects, the socio-economic effects are also impartment, especially in neighboring communities where the geothermal power plant is located. For example, areas that suffer from high rate of unemployment, especially in the rural areas, can benefit from geothermal development.

In Louisiana, the electricity is generated from fossil fuels and nuclear power. According to the annual report from the Louisiana energy facts, the net electricity generation is 54,924 million KWH (11,860 from coal, 4,378 from oil, 22,071 from gas, and 16,615 from nuclear) (Lam 2013). The fossil and nuclear plants are harmful to the environment and people's health not only, but also are limited and not renewable. The development of a geothermal plant can help reduce the state's reliance of power production from fossil fuels and nuclear power. Whilst development proposes to bring about positive change, it can lead to negative effects as well. For example, construction of geothermal power plants can affect the stability of land and lead to subsidence which may cause earthquake activity. In this report, we will analyze the environmental and social aspects of geothermal development in the state of Louisiana. There are

three potential sites, which are E. Hackberry, Sweet Lake and Gueydan. These three sites are located in three different census tracts, of which E. Hackberry and Sweet Lake are located in the Cameron Parish while Gueydan is located in the Vermillion Parish.

The land use pattern in Louisiana and the potential geothermal plant sites can be seen in Figure 1. The land use and land cover data is from the National Land Cover Database (NLCD) which is in a 16-class land cover classification scheme covering the contiguous United States at a ground spacing of 30 meters (Wickham et al. 2013, Fry et al. 2011). NLCD is based primarily on the unsupervised classification of Landsat Enhanced Thematic Mapper+ (ETM+) circa satellite data (Fry et al. 2011). The map data is based in the year of 2006 with several categories: water, developed, barren, forest, shrubland, herbaceous, planted/cultivated and wetlands. The area of Louisiana is about 130,000 km^2 with 64 counties and 1106 census tracts.

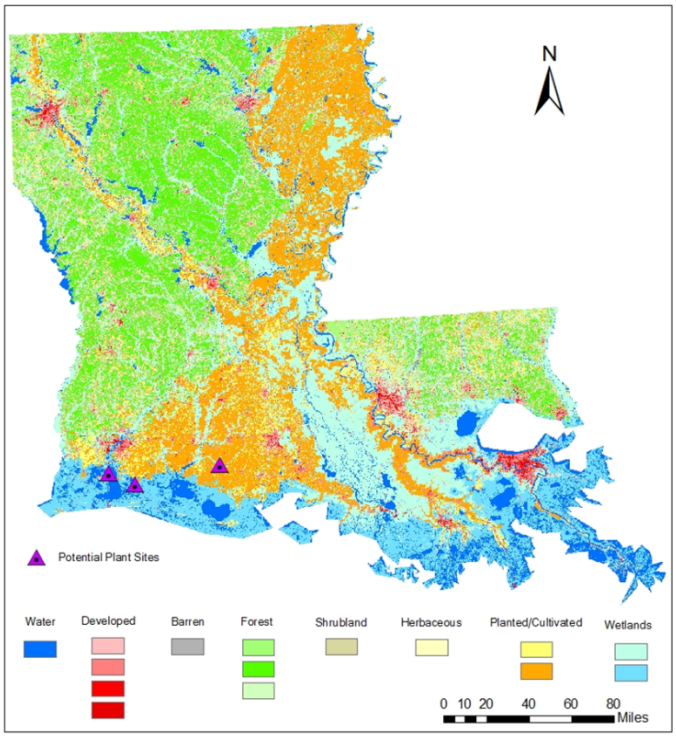

Figure 1 Land use patterns in Louisiana and the potential geothermal plant sites

(Note: Colors were defined according to the NLCD 2006 legend)

Environmental Impacts

Flood analysis

Hazus-MH 2.1 was used in this part to estimate the 100 years flood zone around each potential geothermal site as a consideration for decision making. Hazus-MH is a commercial off-the-shelf loss and risk assessment software package based on ArcGIS software produced by Federal Emergency Management Agency (FEMA). Hazus-MH includes multiple model of three different hazards type: hurricanes, flooding and earthquake. Each model estimates the hazards in three steps. First, it calculates the exposure for a user selected study area. Second, it creates scenarios by characterizing the level or intensity of the specific hazard affecting the exposed study area with historical hazards data or user defined hazards data. Then the Hazus-MH will calculate the potential losses like economic losses, structural damage, the number and level of people affected.

In flood analysis, step one and two could show the potential flood hazard around each potential sites and the affection to the possible geothermal facilities. A 100-year flood is a flood hazard that has a 1% probability of occurring in any given year. The 100-year flood is also called 1% flood because of the 1% probability or having a return period of 100-years. 100-year flood was used here to represent the flood hazards.

Site E. Hackberry locates in a census tract which ID is 22023970201 in Cameron Parish. As showing in the map, the geothermal site is a 0.8 mile away from the nearest flood boundary of 100 years flood. Considering the size of geothermal facility, 0.8 mile could be considered as a safe distance.

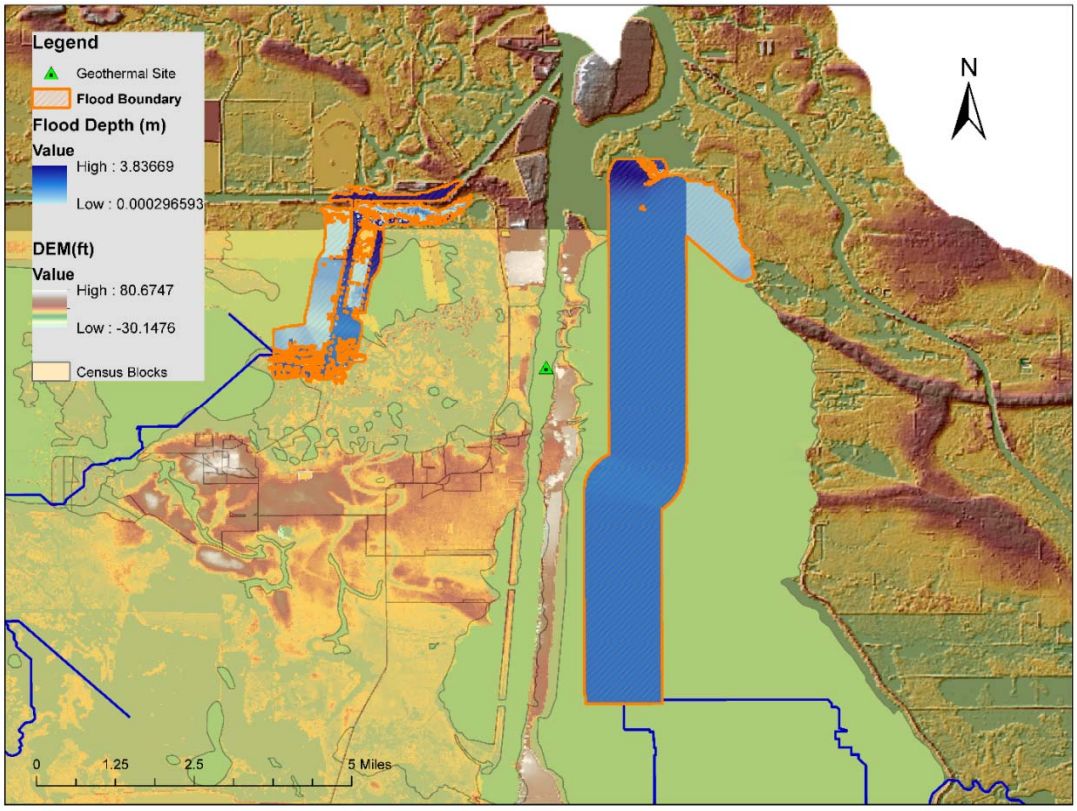

Figure 2 Flood zone around Site E. Hackberry

Site Sweet Lake locates in the census tract with ID 22023970100 in Cameron Parish. As showing in the map, the geothermal site is a 0.04 mile away from the nearest flood boundary of 100 years flood. Considering of the size of geothermal facilities, it is a short distance that facing a 2 meters flood rick.

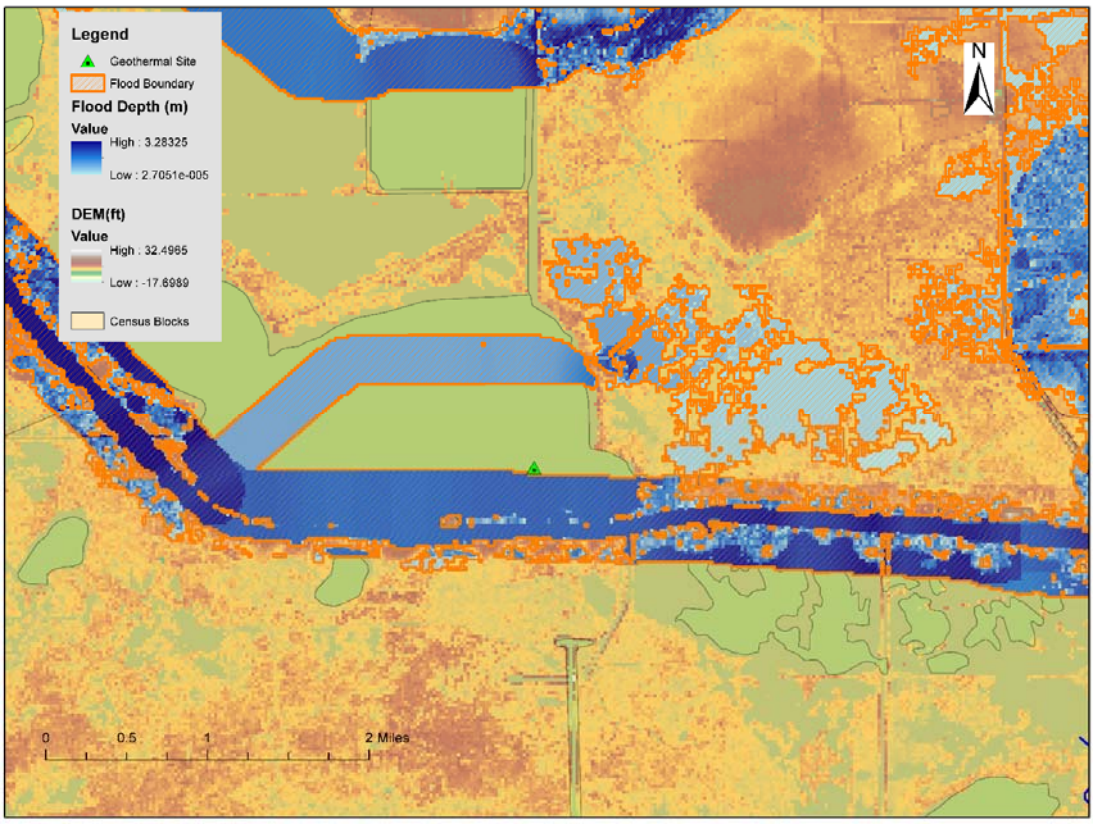

Figure 3 Flood zone around site Sweet Lake

Site Gueydan locates in census tract 22113950200 in Vermilion Parish. As showing in the map, the geothermal site is a 0.007 mile away from the nearest flood boundary of 100 years flood. Considering of the size of geothermal facilities, part of the facilities area will be affected by 0.2-0.6 meter flood.

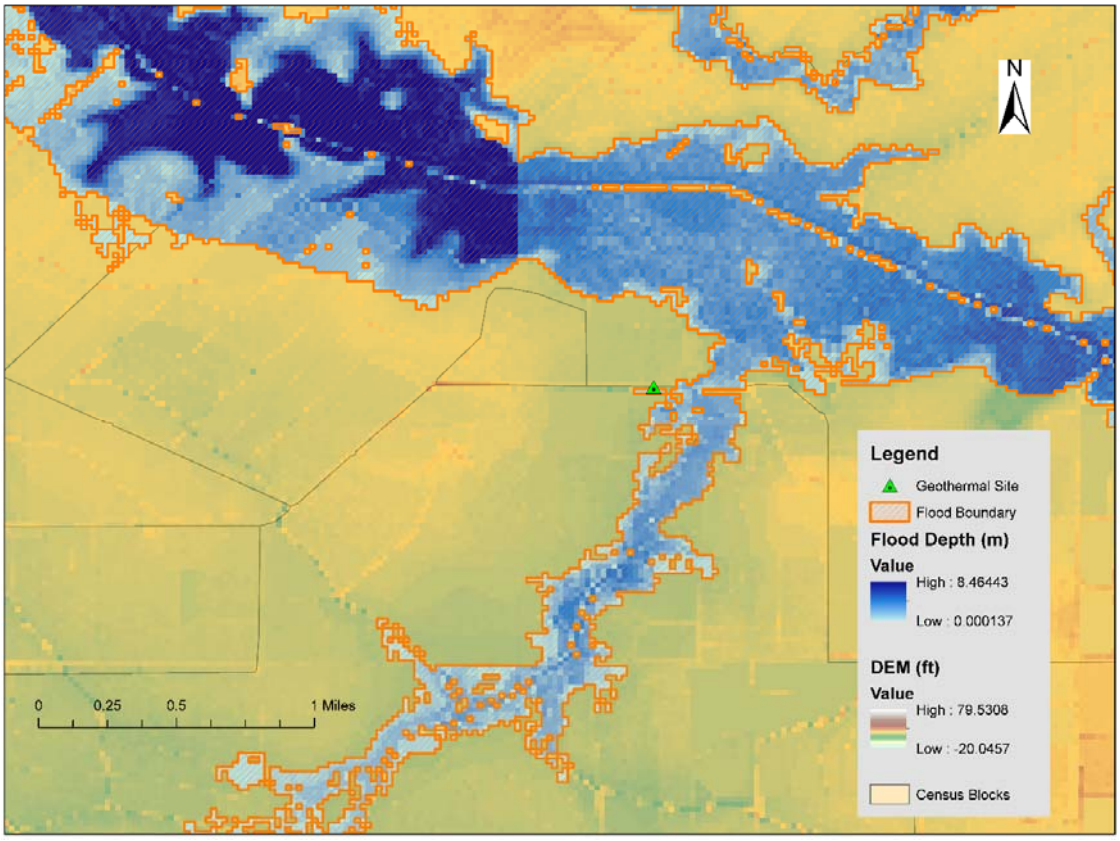

Figure 4 Flood zone around site Gueydan

Induced Seismicity Risk

With large amounts of geothermal fluids being popped and injected below the earth's surface, induced seismicity or earthquake activity is an important concern. Hazus-MH earthquake model was used again here which could estimate the total losses caused by earthquake in the study areas. One of the biggest earthquake happened in Basel geothermal area in 2009 which made Switzerland government abort this project registered as magnitude 3.4 and underground 3 miles (4.8 km) (Gabbatt 2009). Recently report shows the worst earthquakes caused by wastewater wells or geothermal power facilities can reach magnitude 4.0 to 5.0 according to the earthquakes record in United States since 2003-2013 (Joyce 2013). So this research uses magnitude 5.0 in user defined earthquake with 5 miles deep to show the worst scenario.

For scenario one, a magnitude 5.0 earthquake happens in the first potential geothermal site, E. Hackberry, locating in a census tract which ID is 22023970201 in Cameron Parish.

Table 1 Low seismic design building damage rate in site E. Hackberry

Building Damage % Distribution by Building Type for Low Design Level

February 16, 2014

	% Distribution by Damage State				
	None	Slight	Moderate	Extensive	Complete
Louisiana					
Cameron					
Wood	93.78	5.44	0.74	0.04	0.00
Steel	89.62	6.70	3.26	0.41	0.01
Concrete	92.34	5.77	1.78	0.10	0.00
Precast	88.15	6.23	4.58	1.03	0.01
Reinforced Masonry	92.24	4.68	2.73	0.35	0.00
Unreinforced Masonry	84.96	9.92	4.33	0.72	0.07
Manufactured Home	84.67	10.10	4.81	0.42	0.00
County	**90.40**	**7.13**	**2.24**	**0.22**	**0.01**

Table 2 Pre code seismic design building damage rate in site E. Hackberry

Building Damage % Distribution by Building Type for Pre Code Design Level

February 16, 2014

	% Distribution by Damage State				
	None	Slight	Moderate	Extensive	Complete
Louisiana					
Cameron					
Wood	88.37	9.48	2.03	0.11	0.01
Steel	82.95	10.03	5.92	1.08	0.02
Concrete	86.31	9.36	3.91	0.41	0.00
Precast	80.08	9.55	8.17	2.15	0.04
Reinforced Masonry	87.39	6.79	4.88	0.93	0.00
Unreinforced Masonry	75.31	14.24	8.21	1.95	0.29
Manufactured Home	74.89	15.85	8.89	0.36	0.01
County	**83.39**	**11.62**	**4.56**	**0.39**	**0.04**

Table 3 Directly economic losses for buildings in site E. Hackberry

Direct Economic Losses For Buildings

February 16, 2014 — *All values are in thousands of dollars*

	Capital Stock Losses					Income Losses				
	Cost Structural Damage	Cost Non-struct. Damage	Cost Contents Damage	Inventory Loss	Loss Ratio %	Relocation Loss	Capital Related Loss	Wages Losses	Rental Income Loss	Total Loss
Louisiana										
Cameron	594	1,716	638	34	0.60	455	98	137	176	3,847
Total	**594**	**1,716**	**638**	**34**	**0.60**	**455**	**98**	**137**	**176**	**3,847**
Region Total	**594**	**1,716**	**638**	**34**	**0.60**	**455**	**98**	**137**	**176**	**3,847**

Table 4 Directly losses for transportation in site E. Hackberry

Direct Economic Loss For Transportation

February 16, 2014 — *All values are in thousands of dollars*

	Highway	Railway	Light Rail	Bus Facility	Ports	Ferries	Airport	Total
Louisiana								
Cameron								
Segments	0	0	0					0
Bridges	158	0	0					158
Tunnels	0	0	0					0
Facilities		0	0	0	15,464	406	0	15,870
Total	**158**	**0**	**0**	**0**	**15,464**	**406**	**0**	**16,027**
Total	**158**	**0**	**0**	**0**	**15,464**	**406**	**0**	**16,027**
Region Total	**158**	**0**	**0**	**0**	**15,464**	**406**	**0**	**16,027**

For scenario two, a magnitude 5.0 earthquake happens in the second potential geothermal site Sweet Lake locates in a census tract which ID is 22023970100 in Cameron Parish.

Table 5 Low seismic design building damage rate in site Sweet Lake

Building Damage % Distribution by Building Type for Low Design Level

February 16, 2014

	% Distribution by Damage State				
	None	Slight	Moderate	Extensive	Complete
Louisiana					
Cameron					
Wood	91.00	7.73	1.20	0.08	0.00
Steel	85.98	8.64	4.70	0.66	0.02
Concrete	89.82	7.41	2.58	0.18	0.00
Precast	84.30	7.90	6.24	1.56	0.01
Reinforced Masonry	89.64	5.96	3.85	0.55	0.00
Unreinforced Masonry	80.30	12.49	5.98	1.11	0.12
Manufactured Home	81.25	12.07	6.09	0.58	0.01
County	**87.10**	**9.42**	**3.13**	**0.33**	**0.01**

Table 6 Pre code seismic design building damage rate in site Sweet Lake

Building Damage % Distribution by Building Type for Pre Code Design Level

February 16, 2014

	% Distribution by Damage State				
	None	Slight	Moderate	Extensive	Complete
Louisiana					
Cameron					
Wood	84.45	12.33	3.01	0.20	0.01
Steel	77.50	12.34	8.37	1.73	0.05
Concrete	81.93	11.73	5.63	0.70	0.02
Precast	75.22	11.17	10.45	3.09	0.08
Reinforced Masonry	83.86	8.21	6.52	1.40	0.01
Unreinforced Masonry	70.05	16.46	10.31	2.72	0.46
Manufactured Home	68.02	18.82	12.44	0.69	0.03
County	**78.25**	**14.56**	**6.52**	**0.61**	**0.06**

Table 7 Directly economic losses for buildings in site Sweet Lake

Direct Economic Losses For Buildings

February 16, 2014 — All values are in thousands of dollars

	Capital Stock Losses					Income Losses				
	Cost Structural Damage	Cost Non-struct. Damage	Cost Contents Damage	Inventory Loss	Loss Ratio %	Relocation Loss	Capital Related Loss	Wages Losses	Rental Income Loss	Total Loss
Louisiana										
Cameron	732	2,413	850	15	0.88	619	185	283	334	5,430
Total	**732**	**2,413**	**850**	**15**	**0.88**	**619**	**185**	**283**	**334**	**5,430**
Region Total	**732**	**2,413**	**850**	**15**	**0.88**	**619**	**185**	**283**	**334**	**5,430**

Table 8 Directly economic losses for transportation in site Sweet Lake

Direct Economic Loss For Transportation

February 16, 2014 — All values are in thousands of dollars

	Highway	Railway	Light Rail	Bus Facility	Ports	Ferries	Airport	Total
Louisiana								
Cameron								
Segments	0	0	0					0
Bridges	3,335	0	0					3,335
Tunnels	0	0	0					0
Facilities		0	0	0	1,103	0	0	1,103
Total	**3,335**	**0**	**0**	**0**	**1,103**	**0**	**0**	**4,439**
Total	**3,335**	**0**	**0**	**0**	**1,103**	**0**	**0**	**4,439**
Region Total	**3,335**	**0**	**0**	**0**	**1,103**	**0**	**0**	**4,439**

For scenario three, a magnitude 5.0 earthquake happens in the third potential geothermal site Gueydan locates in a census tract which ID is 22113950200 in Vermillion Parish. This site locates in the intersection of different parishes which were all included in the analysis.

Table 9 Low seismic design building damage rate in site Gueydan

Building Damage % Distribution by Building Type for Low Design Level

February 16, 2014

	% Distribution by Damage State				
	None	Slight	Moderate	Extensive	Complete
Louisiana					
Acadia					
Wood	90.04	8.09	1.73	0.14	0.01
Steel	84.75	8.11	5.71	1.30	0.12
Concrete	88.74	7.39	3.43	0.41	0.03
Precast	84.52	7.19	6.31	1.94	0.04
Reinforced Masonry	88.42	6.08	4.57	0.91	0.01
Unreinforced Masonry	80.23	11.67	6.39	1.48	0.23
Manufactured Home	81.99	10.66	6.40	0.93	0.02
Cameron					
Wood	99.47	0.49	0.04	0.00	0.00
Steel	98.60	1.04	0.34	0.03	0.00
Concrete	99.11	0.74	0.14	0.01	0.00
Precast	98.61	0.83	0.48	0.08	0.00
Reinforced Masonry	99.25	0.52	0.21	0.02	0.00
Unreinforced Masonry	98.09	1.42	0.44	0.05	0.00
Manufactured Home	98.14	1.35	0.49	0.03	0.00
Jefferson Davis					
Wood	95.68	3.80	0.50	0.03	0.00
Steel	92.33	5.05	2.34	0.28	0.01
Concrete	94.70	4.07	1.16	0.07	0.00
Precast	91.74	4.42	3.15	0.69	0.00
Reinforced Masonry	94.21	3.58	1.97	0.24	0.00
Unreinforced Masonry	88.93	7.43	3.10	0.49	0.05
Manufactured Home	91.26	5.90	2.64	0.21	0.00
Lafayette					
Wood	98.47	1.40	0.13	0.01	0.00
Steel	96.35	2.62	0.94	0.09	0.00
Concrete	97.58	1.99	0.41	0.02	0.00
Precast	96.25	2.19	1.33	0.23	0.00
Reinforced Masonry	97.54	1.68	0.71	0.06	0.00

Table 10 Pre code seismic design building damage rate in site Gueydan

Building Damage % Distribution by Building Type for Pre Code Design Level

February 16, 2014

	% Distribution by Damage State				
	None	Slight	Moderate	Extensive	Complete
Louisiana					
Acadia					
Wood	84.17	11.84	3.61	0.35	0.03
Steel	77.19	10.65	8.90	2.93	0.33
Concrete	80.72	10.79	6.78	1.58	0.12
Precast	76.08	9.88	10.08	3.74	0.22
Reinforced Masonry	81.77	8.07	7.66	2.43	0.07
Unreinforced Masonry	71.07	14.99	10.10	3.12	0.72
Manufactured Home	67.85	14.57	13.30	3.69	0.60
Cameron					
Wood	98.58	1.25	0.16	0.01	0.00
Steel	97.26	1.92	0.72	0.09	0.00
Concrete	98.07	1.53	0.37	0.03	0.00
Precast	96.63	1.96	1.20	0.21	0.00
Reinforced Masonry	98.43	1.01	0.50	0.06	0.00
Unreinforced Masonry	95.41	3.08	1.29	0.20	0.02
Manufactured Home	94.49	4.08	1.41	0.02	0.00
Jefferson Davis					
Wood	91.59	6.92	1.40	0.08	0.00
Steel	87.17	7.79	4.27	0.75	0.01
Concrete	90.21	6.91	2.61	0.26	0.00
Precast	85.20	7.40	5.91	1.46	0.03
Reinforced Masonry	90.26	5.40	3.67	0.66	0.00
Unreinforced Masonry	80.68	11.49	6.23	1.39	0.20
Manufactured Home	83.03	11.31	5.47	0.18	0.01
Lafayette					
Wood	96.23	3.27	0.48	0.02	0.00
Steel	93.24	4.61	1.89	0.26	0.00
Concrete	95.00	3.87	1.05	0.08	0.00
Precast	91.58	4.75	3.09	0.58	0.00
Reinforced Masonry	95.14	3.04	1.61	0.21	0.00

Table 11 Directly economic losses for buildings in site Gueydan

Direct Economic Losses For Buildings

February 16, 2014 — *All values are in thousands of dollars*

	Capital Stock Losses					Income Losses				
	Cost Structural Damage	Cost Non-struct. Damage	Cost Contents Damage	Inventory Loss	Loss Ratio %	Relocation Loss	Capital Related Loss	Wages Losses	Rental Income Loss	Total Loss
Louisiana										
Lafayette	6,281	14,159	3,868	129	0.14	4,687	1,906	2,469	2,393	35,894
Acadia	8,993	29,148	12,481	730	1.14	7,236	1,517	2,045	2,571	64,722
Jefferson Davis	1,925	5,533	1,876	42	0.40	1,591	413	550	649	12,578
Cameron	118	247	49	1	0.05	91	29	44	54	633
Vermilion	8,685	28,793	11,215	233	1.18	6,994	1,425	1,862	2,428	61,635
Total	**26,001**	**77,881**	**29,489**	**1,136**	**0.58**	**20,598**	**5,291**	**6,970**	**8,095**	**175,462**
Region Total	**26,001**	**77,881**	**29,489**	**1,136**	**0.58**	**20,598**	**5,291**	**6,970**	**8,095**	**175,462**

Table 12 Directly economic losses for transportation in site Gueydan

Direct Economic Loss For Transportation

February 16, 2014 — All values are in thousands of dollars

	Highway	Railway	Light Rail	Bus Facility	Ports	Ferries	Airport	Total
Louisiana								
Acadia								
Segments	0	0	0					0
Bridges	1,422	0	0					1,422
Tunnels	0	0	0					0
Facilities		0	0	0	0	0	2,912	2,912
Total	**1,422**	**0**	**0**	**0**	**0**	**0**	**2,912**	**4,334**
Cameron								
Segments	0	0	0					0
Bridges	9	0	0					9
Tunnels	0	0	0					0
Facilities		0	0	0	197	7	0	204
Total	**9**	**0**	**0**	**0**	**197**	**7**	**0**	**213**
Jefferson Davis								
Segments	0	0	0					0
Bridges	110	0	0					110
Tunnels	0	0	0					0
Facilities		0	0	34	0	0	771	805
Total	**110**	**0**	**0**	**34**	**0**	**0**	**771**	**915**
Lafayette								
Segments	0	0	0					0
Bridges	38	0	0					38
Tunnels	0	0	0					0
Facilities		80	0	15	0	0	145	240
Total	**38**	**80**	**0**	**15**	**0**	**0**	**145**	**278**
Vermilion								
Segments	0	0	0					0
Bridges	880	0	0					880
Tunnels	0	0	0					0
Facilities		0	0	0	0	0	321	321
Total	**880**	**0**	**0**	**0**	**0**	**0**	**321**	**1,201**
Total	**2,458**	**80**	**0**	**49**	**197**	**7**	**4,149**	**6,940**
Region Total	**2,458**	**80**	**0**	**49**	**197**	**7**	**4,149**	**6,940**

Smaller land footprint

A recent paper evaluates the intensity of land use associated with different energy sources based on the prospective technology in the year 2030. Geothermal power's estimated usage of 7.5 km^2/TW hr/yr which is better than coal (9.7), solar thermal (15.3), natural gas (18.6), solar voltaic (36.9), petroleum (44.7), hydropower (54.0), wind (72.1), and biomass (543.4). (McDonald et al. 2009)

Low emission levels

Geothermal power plant has very low emission levels by comparing with other plants by using fossil fuel. Figure 5 shows the geographic distribution of Toxics Release Inventory (TRI) reporting facilities in Louisiana from the United States Environmental Protection Agency. TRI tracks the management of certain toxin chemicals that may threaten human health and the environment (http://www2.epa.gov/toxics-release-inventory-tri-program/learn-about-toxics-release-inventory). By checking the figure, we can see that there are many facilities with toxic release around site E. Hackberry.

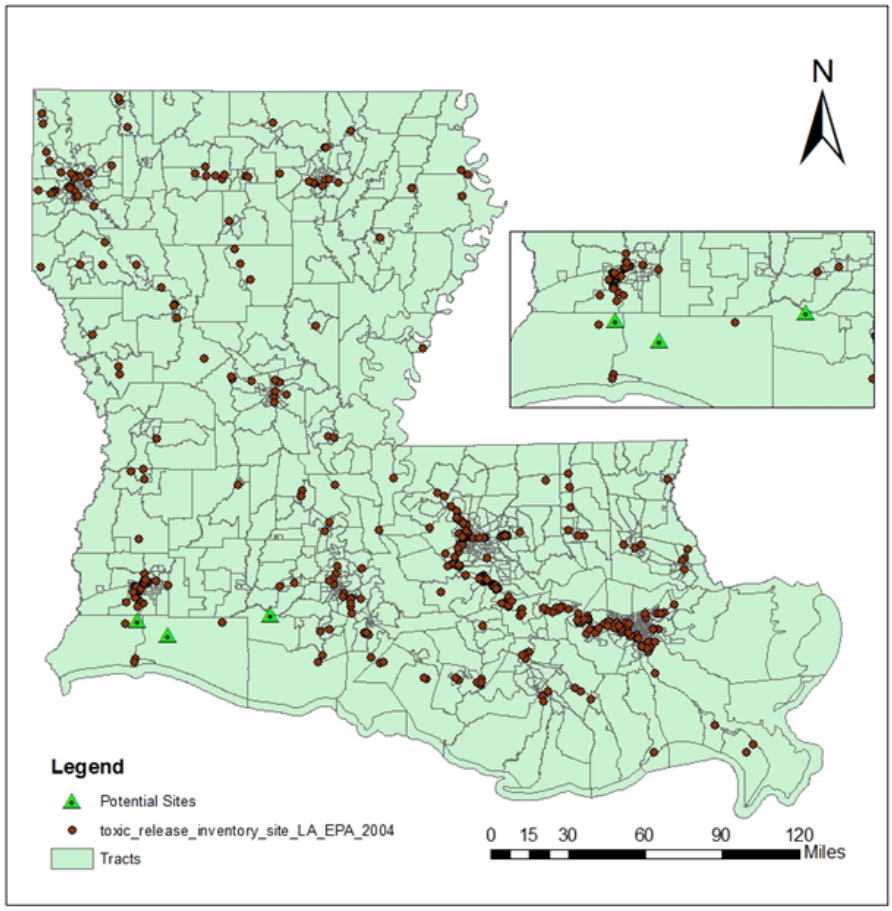

Figure 5 Geographic distribution of TRI reporting facilities in Louisiana

Socio-Economic Issues

Table 13 shows the socio-economic characteristics in the three census tract where the potential geothermal power plants locate.

Table 13 Socio-economic characteristics for the three tracts

TractID	**22023970201**	**22023970100**	**22113950200**
Population	1956	4883	5075
Population Density	3.9	6.3	20.2
Black Percentage	0.82	2.11	4.61
Households	783	1792	2018
Unemployment Rate	4.2	3.0	1.7
High school percentage	4.6	9.3	5.7
Median Household Income	51510	65822	43979
Poverty rate	9.8	5.1	11.6

Reduce poverty

Geothermal energy has potential for increasing the positive impact on poor communities which then contribute to poverty reduction. From the above table, census tract where site Gueydan locates has the highest poverty rate and largest black population.

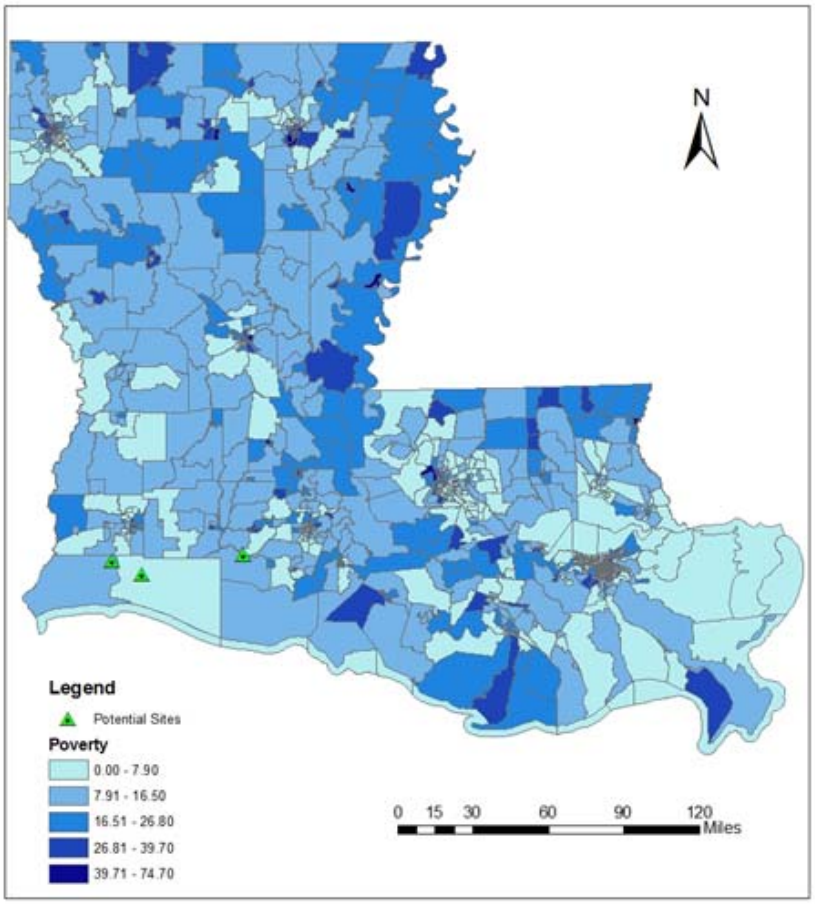

Figure 6 Distribution of Louisiana Tracts in Poverty

Create job opportunities

In census tract 22023970201 where site E. Hackberry locates, the estimated unemployment rate here was 4.2% in summer 2010, affecting an estimated 35 people age 16 and over. In census tract 22023970100 where site Sweet Lake locates, the estimated unemployment rate here was 3.0% in summer 2010, affecting an estimated 79 people age 16 and over. In census tract 22113950200

where site Gueydan locates, the estimated unemployment rate here was 1.7% in summer 2010, affecting an estimated 39 people age 16 and over.

The development of geothermal power plants can create direct job opportunities for high caliber of professionals, including scientist in geology, geophysics, geochemistry and human resources and engineers in civil, electrical and mechanical. The local communities benefit mostly from unskilled and semi-skilled labor during the construction of the geothermal projects, such as construction of assesses road, masonry, loading/off-loading and so on. Geothermal power creates more jobs per megawatt than natural gas (Table 14) (Deloitte Consulting LLP 2008). The proposed power plant would be approximately between 250 kW and 1 MW in generating capacity which will create plenty of jobs.

Table 14 Comparative Job Creation

Power Source	Construction Employment (jobs/MW)	O&M Employment * (jobs/MW)	Total Employment for 500 MW Capacity (person-years)
Geothermal	4.0	1.7	27,050
Natural Gas	1.0	0.1	2,460

*O&M: Operation and Maintenance; Source: U.S. DOE 2006

Alleviate power outages

The geothermal development can increase power supply and subsequent steadiness of electricity. Unlike solar panels which is dependent on the sun and light, geothermal power plants are unaffected by weather and night cycle. Residents, hospitals and schools are benefit from this characteristic of geothermal energy.

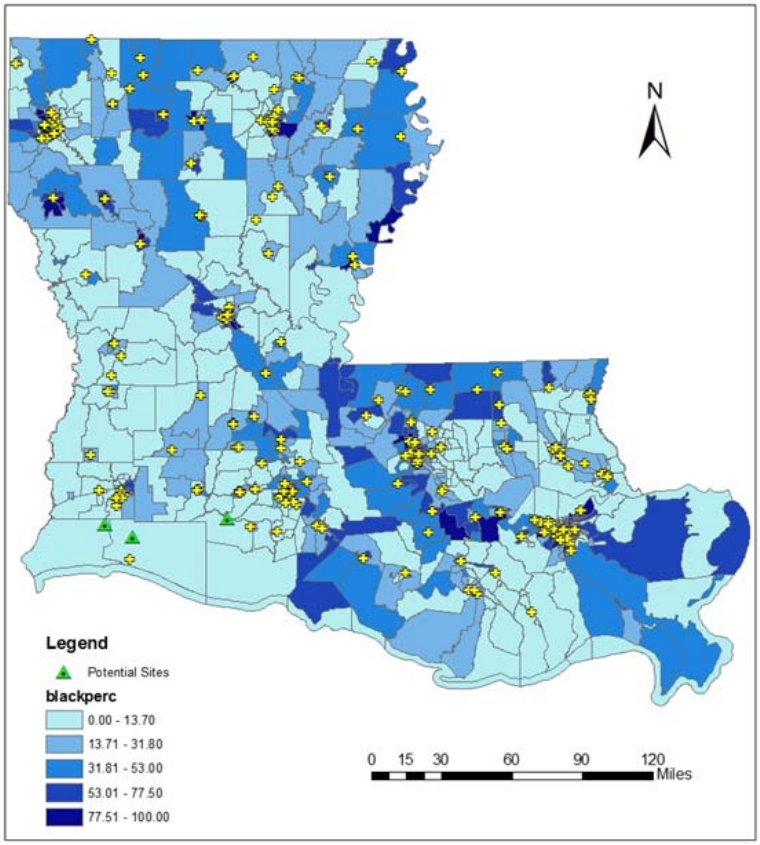

Figure 7 Distribution of Louisiana Black Population and Hospitals

Other related issues

Tourism

To build a geothermal power plant will improve on movement within the project area and increase in tourism. Sabine National Wildlife Refuge is about 8 miles south of Hackberry which provides colorful activities like environmental education, fishing, hunting, and wildlife observation. Every year there is over 280,000 people visit the refuge . Cameron Prairie National Wildlife Refuge is located in north central Cameron parish and there are about 30,000 people visit the refuge annually (http://www.fws.gov/swlarefugecomplex).

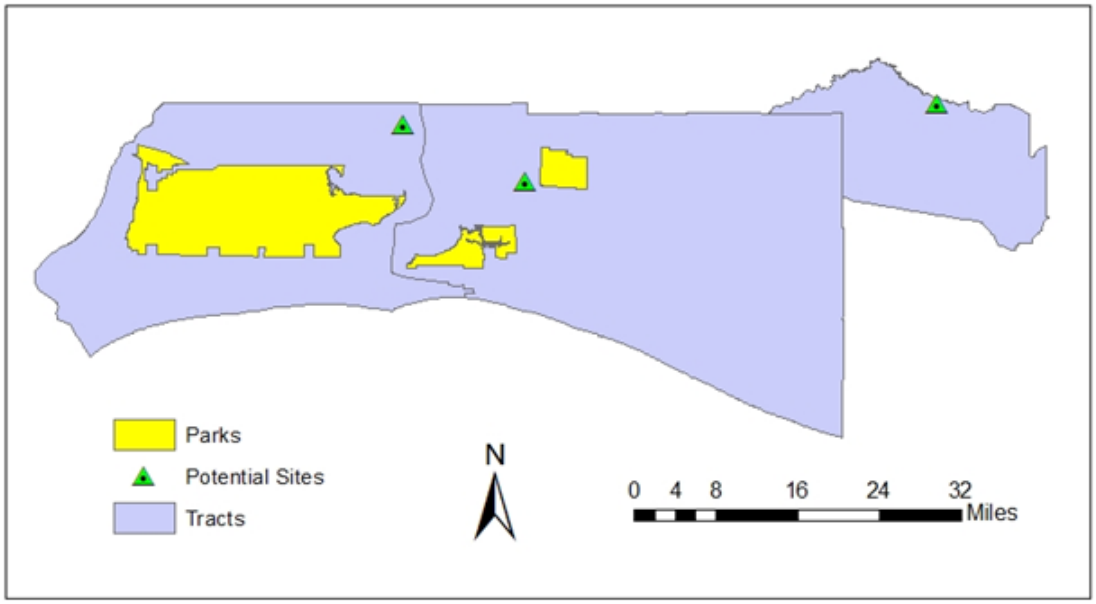

Figure 8 Parks in the three tracts where the potential geothermal sites are located

Airport

Airports should also be considered because the large steam plumes leaving the plants can obstruct air traffic. Figure shows the airport position in Louisiana. The potential site in the E. Hackberry area may face this problem.

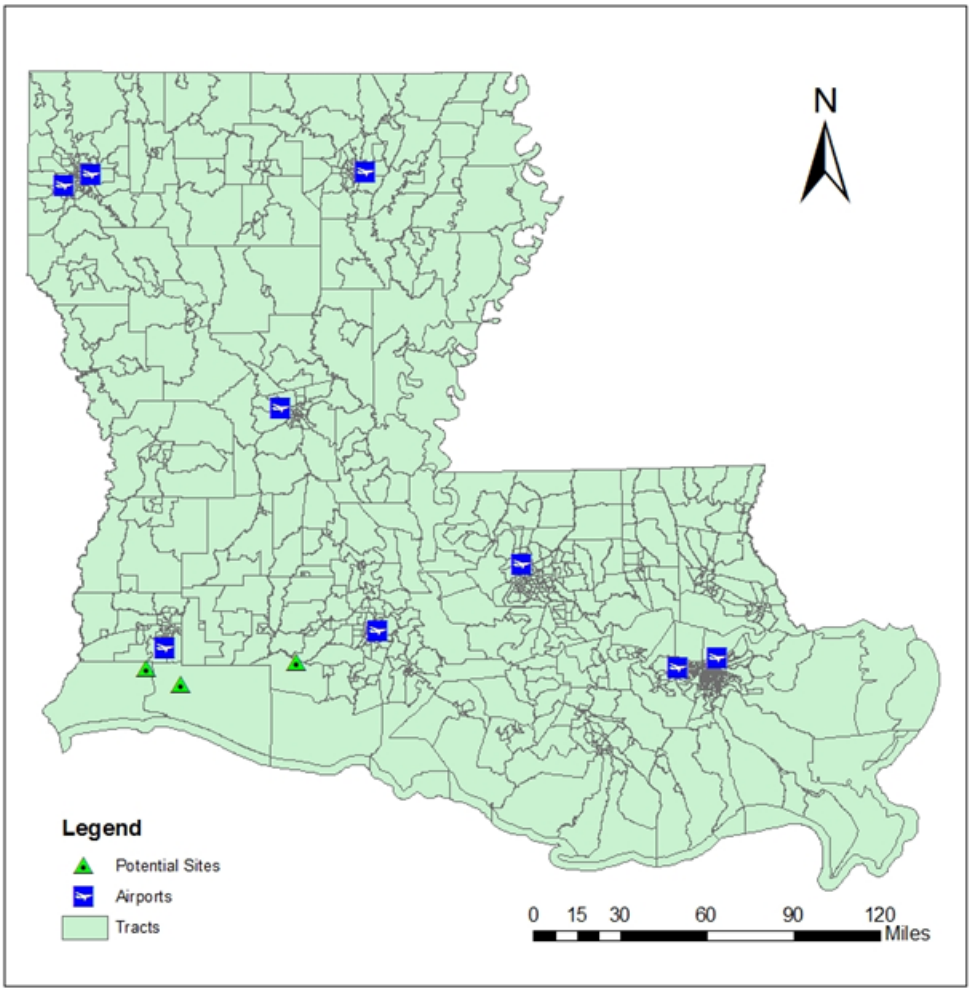

Figure 9 Airports in Louisiana

Reference

Deloitte Consulting LLP. 2008. Market Analysis-Geothermal. In *Geothermal Technologies Program*, prepared for the US Department of Energy.

Fry, J. A., G. Xian, S. Jin, J. A. Dewitz, C. G. Homer, L. Yang, C. A. Barnes, N. D. Herold & J. D. Wichham (2011) Completion of the 2006 National Land Cover Database for the Conterminous United States. *Photogrammetric engineering and remote sensing,* 77**,** 858-864.

Gabbatt, A. 2009. Swiss geothermal power plan abandoned after quakes hit Basel. In *Associated Press*.

Joyce, C. 2013. Wasterwater Wells, Geothermal Power Triggering Earthquakes.

Kagel, A. 2006. A Handbook on the Externalities, Employment, and Economics of Geothermal Energy. Washington, D.C.

Lam, M. 2013. Louisiana Energy Facts Annual 2012. ed. N. Resources. Baton Rouge: Techonolgy Assessment Division of the Louisiana Department of Natural Resources.

Lund, J. W., D. H. Freeston & T. L. Boyd. 2005. World-Wide Direct Uses of Geothermal Energy 2005. In *Proceedings World Geothermal Congress 2005*. Antalya, Turkey.

McDonald, R. I., J. Fargione, J. Kiesecker, W. M. Miller & J. Powell (2009) Energy Sprawl or Energy Efficiency: Climate Policy Impacts on Natural Habitat for the United States of America. *PLOS ONE,* 4.

Wickham, J. D., S. V. Stehman, L. Gass, J. Dewitz, J. A. Fry & T. G. Wade (2013) Accuracy assessment of NLCD 2006 land cover and impervious surface. *Remote Sensing of Environment,* 130**,** 294-304.